Genetically engineered Mouse Models reveal a tumourigenic collaboration between *Sdhb* deficiency and oncogenic *Hras*

Dr. med. Jan Henry Matthias Däbritz

Thesis submitted to the University of Glasgow in fulfilment of the requirements for the Degree of Doctor of Philosophy

Institute of Cancer Sciences
College of Medical, Veterinary and Life Sciences
University of Glasgow
April 2019

CRUK Beatson Institute
Garscube Estate
Switchback Road
Bearsden, Glasgow

Abstract

The mitochondrial tumour suppressor succinate dehydrogenase is found inactivated in several tumour entities, amongst them SDH–deficient renal cell carcinoma (RCC) and pheochromocytomas/paragangliomas (Pheo/PGL). Publically available data show an association of activating *HRAS* mutations with genetic *SDHB* deletions in Pheo/PGL, but an in-depth understanding of cooperating events that enable malignant transformation of SDH-deficient tissues and preclinical model systems of SDH-deficient malignancies are still lacking.

The first major goal of this thesis project was to generate a genetically engineered model of SDH-deficient RCC as an easy-to-monitor pathology in mice. In addition, we set out to study tissue-specific phenotypes resulting from stochastic *Sdhb* loss in peripheral organs. Based on the hypothesis that defined metabolic constraints imposed by loss of SDH function might drive similar collaborating genetic alterations of SDH-deficient tumours in different organs, we combined deletion of the essential *Sdhb* exon 3 ($Sdhb^{fl/fl}$) with activation of oncogenic *Hras* ($Hras^{LSLG12V}$) in our models.

Driven by a *Cadherin 16* promoter (*KspCre*) and thus in the distal renal tubular system, the postulated origin of SDH-deficient RCC, a fatal cystic degeneration of $Sdhb^{fl/fl}$ kidneys resulted from Cre expression. While not causing clinical events in SDHB-proficient mice, $Hras^{LSLG12V}$ shortened endpoint latency in $Sdhb^{fl/fl}$ animals in an allele dose-dependent fashion. Age-matched $Sdhb^{fl/fl}$, $Hras^{LSLG12V}$ kidneys displayed higher cyst content as well as more pronounced pre-malignant features in comparison to matched $Sdhb^{fl/fl}$, $Hras^{wildtype}$ cases. Ongoing untargeted metabolomics analyses of kidney, plasma and urine specimens obtained from this model hold potential for discovery of new biomarkers of SDH-deficient tumours.

In a $RosaCreER^{T2}$-based model, dramatic weight loss within the first weeks after transgene induction correlated with succinate accumulation in peripheral organs of $Sdhb^{fl/fl}$, $Hras^{wt/wt}$ animals. Less intense transgene induction schemes resulted in long-term survival irrespective of *Sdhb* status. Compared to $Sdhb^{wt/wt}$, $Hras^{wt/LSLG12V}$ animals, $Sdhb^{fl/fl}$, $Hras^{wt/LSLG12V}$ mice developed significantly higher degrees of papillomatous skin changes under long-term observation.

The findings presented in this thesis argue in favour of a tumour-promoting collaboration between genetic loss of *Sdhb* (or the resulting succinate accumulation) and *Hras* activation in two different organs. To the best of my knowledge, this work describes the first, albeit not perfect, genetically engineered mouse model of SDH-deficient RCC. Ongoing experimental efforts focus on reliable identification of systemic metabolic biomarkers that could improve monitoring of patients who are at (relapse) risk of SDH-deficient tumours. In addition, gene expression analyses are aiming at a mechanistic understanding of the interaction between *Hras* activation and *Sdhb* loss.

Table of Contents

List of Tables

List of Figures

Acknowledgements

First of all, I would like to thank my supervisor, Prof. Eyal Gottlieb, for inviting me to join his research group in Glasgow, for giving me the scientific freedom of working in his laboratory and for his mentoring throughout the last four years. I would also like to thank my PhD advisor Professor Hing Leung for his continuous support with regards to scientific strategies as well as to career advice for myself as a clinician scientist.

I am very grateful to former members of R12 for their support, most of all Elaine D. MacKenzie for her practical and administrative help with mouse work, for investing endless hours in quantifying "my" IHC stainings and for just always being there to help in whatever way possible. Many thanks to Jiska, Johan, Saverio, Elodie and Stefan for being such great colleagues and for sharing the joyful as well as the low moments in the lab. A special "Thank you" to Leon for helping me to get started with mass spectrometry and all the crazy discussions that we had in the late evening hours of my first year.

I would also like to thank Dr. Karen Blyth for her essential support of my mouse projects and for our monthly meetings with valuable feedback and suggestions. I feel equally obliged to the metabolomics facility at the Beatson Institute (David Sumpton, Niels van den Broek and Gillian MacKay) for developing the untargeted metabolomics approaches discussed in this work and for trying to introduce me to some of the many secrets of mass spectrometry. In addition, I am also extremely grateful to our collaborator Markus Eckstein (Institut für Pathologie, Universitätsklinikum Erlangen) for his comprehensive pathological review of our mouse models.

Thanks a lot to Saadia Karim for teaching me in mouse kidney ultrasound and to Susan Mason, Dimitris Athineos, Rachel Ridgway and Sandeep Dhayade for training me on mouse models and looking after "my" mice when I was away. My work would never have been possible without the amazing staff of the animal facility of the Beatson Institute. Thank you all so much! I would also like to say "Thank you" for the immense support of my work by the whole team of the histology facility at the Beatson Institute, especially to Dr. Colin Nixon, Gemma Thomson and Mark Hughes. Thanks a lot to William Clark, Robin Shaw, Liat Linde and Ann Hedley for

helping me with RNA sequencing and, especially, to Jonatan Fernández García for his skillful and timely analysis of transcriptomic data. Furthermore, I am extremely grateful to Joo Sang Lee and Eytan Ruppin for sharing results of their computational work (that provided the basis for our mouse experiments) with us.

Only with strong commitment and support by Jayne Bressington and Dr. Ramesh Bulusu, I was able to join the PAWS-GIST clinic and obtain primary human SDH-deficient GIST tumour tissues. Thank you so much!

I also want to thank all staff members of central services and in general to everybody at the CRUK Beatson Institute for making it such an amazing place to explore science.

Finally but most importantly, I want to thank my beloved family in Glasgow and Berlin for supporting me in all my decisions and for being so patient with me throughout my PhD time (especially in the last few months!), but also for always reminding me that life is more than just work.

Last but not least, I would like to express my gratitude to CRUK for generously funding my work.

Author’s Declaration

I hereby declare that the work presented in this thesis is the result of my own independent investigation unless explicitly stated as the contribution of others.

This work has hitherto not been accepted for any other degree, nor is it currently being submitted for any other degree.

Dr. med. Jan Henry Matthias Däbritz

Abbreviations

Abbreviation	Expression
4-OHT	4-hydroxytamoxifen
2-HG	2-hydroxyglutarate
α-KG	α-ketoglutarate
BAT	Brown adipose tissue
ccRCC	Clear cell-type renal cell carcinoma
Cdh 16	Cadherin 16
chRCC	Chromophobe renal cell carcinoma
CNS	Central nervous system
Cre	"Causes Recombination" (P1 bacteriophage recombinase)
DNA	Deoxyribonucleic acid
ER	Oestrogen receptor
ERK/Erk	Extracellular signal-regulated kinases
FAD	Flavin adenine dinucleotide, oxidised
$FADH_2$	Flavin adenine dinucleotide, reduced
FDG-PET	^{18}F-deoxyglucose-based positron emission tomography
FDR	False discovery rate
FFPE	Formalin-fixed paraffin-embedded
FH	Fumarate hydratase
fl	floxed
g	Relative centrifugal force
GEMM	Genetically engineered mouse model
GTP	Guanosine triphosphate
H & E	Haematoxylin and eosin
HIF	Hypoxia-inducible factor
HMT	Histone methyltransferase
HPLC	High performance liquid chromatography
HRAS/Hras	Harvey rat sarcoma viral oncogene homolog
Hras^{LSLG12V}	Mouse allele *Hras^{tm1Khai}* (please refer to Table 2)
IDH	Isocitrate dehydrogenase
IHC	Immunohistochemistry
i.p.	Intraperitoneal
KRAS/Kras	Kirsten rat sarcoma viral oncogene homolog

KspCre	Mouse allele Tg(Cdh16-cre)91Igr
LDH	Lactate dehydrogenase
LC-MS	Liquid chromatography-coupled mass spectrometry
loxP	locus of X(cross)-over in P1
MAPK	Mitogen-activated protein kinase
min	minute(s)
mTOR	Mechanistic Target of rapamycin
mTORC	mTOR complex
NAD(H)	Nicotinamide adenine dinucleotide
NADP(H)	Nicotinamide adenine dinucleotide phosphate
PAS	Periodic acid–Schiff
PC/Pc	Pyruvate carboxylase
PCA	Principal component analysis
PDGFRα	Platelet-derived growth factor α
PFA	Paraformaldehyde
PGL	Paraganglioma
Pheo	Pheochromocytoma
PI3K	Phosphatidyl inositol-3-kinase
ppm	parts per million
pRCC	Papillary Renal Cell Carcinoma
QC	Quality Control
RAS/Ras	Rat sarcoma viral oncogene homolog
RCC	renal cell carcinoma
Rfp	Red fluorescent protein
Rfp^{LSL}	Mouse allele Gt(ROSA)26Sor^{tm1Hjf} (please refer to Table 2)
RIN	RNA integrity number
RNA	Ribonucleic acid
ROS	Reactive oxygen species
RosaCreER^{T2}	Mouse allele Gt(ROSA)26Sor$^{tm2(cre/ERT2)Brn}$
rpm	Rounds per minute
RSD	Relative Standard Deviation
RT	Retention Time
RTK	Receptor tyrosine kinase
SDH/Sdh	Succinate dehydrogenase
SDHA/Sdha	Succinate dehydrogenase, subunit A

SDHAF/Sdhaf	Succinate dehydrogenase assembly factor
SDHB/Sdhb	Succinate dehydrogenase, subunit B
SDHC/Sdhc	Succinate dehydrogenase, subunit C
SDHD/Sdhd	Succinate dehydrogenase, subunit D
Sdhb^{fl}	Mouse allele Sdhb$^{Tm1cBea\text{-}4.8C}$ (please refer to table Table 2)
TCA	Tricarboxylic acid
TCGA	The Cancer Genome Atlas
TET	Ten-eleven-translocation methylcytosine dioxygenase
TKI	Tyrosine kinase inhibitor
WCR	water consumption rate
WHO	World Health Organisation
VEGF	Vascular endothelial growth factor
VHL	von Hippel-Lindau

1 Introduction

1.1 General Introduction

At first thought, it might seem far less important to scientifically study a rare disease than trying to improve diagnostic or therapeutic options for a more common medical condition. However, two major lines of evidence argue against this statement. Firstly, albeit *per definitionem*, a single rare disease affects only very few people in a population (<0.05% as defined by the European Union), the 5000-8000 described rare diseases in total are actually quite common, *i.e.* a substantial fraction (about 6-7%) of the general population suffers from a rare disease and is hoping for scientific advances to improve their condition (1, 2). Secondly and of equal importance, rare genetic conditions have substantially aided the understanding of fundamental cellular physiology and its dysregulation in very common diseases. In the context of cancer in particular, important regulators that protect the integrity of the human organism and that are found dysregulated in common, sporadic types of cancers were initially identified in rare malignancies that arise in a syndromic fashion with a strong family background (3, 4)

Since Otto Warburg and his co-workers first described increased aerobic glycolysis in cancerous tissues and implied an underlying general causality of this phenomenon for malignoma growth (5, 6), research has uncovered a diverse spectrum of metabolic alterations in tumours, including cancer driving loss- and gain-of-function mutations in "metabolic genes" (7).

However, almost 100 years of research into cancer metabolism have only translated into a limited number of diagnostic and therapeutic routine applications to date (8). These include imaging of the "Warburg Effect" by ^{18}F-deoxyglucose-based positron emission tomography (FDG PET) and interference with ribonucleic acid or folate metabolism as the mode of action of several classes of classical antineoplastic chemotherapy (8).

In theory, tumours with dependency on genetically encoded (*i.e.* very stable) metabolic alterations provide very attractive targets for specific pharmacological interventions with tumour metabolism. It is thus not surprising that promising

early phase clinical trials with small compounds targeting the neomorphic enzymatic activities of mutant isocitrate dehydrogenase 1 and 2 (IDH1/2) constitute the most recent successful example of a "metabolic" cancer treatment (9, 10). In comparison to *IDH1/2* mutated cancers, current therapeutic approaches against *SDH*- and *FH*-deficient tumours are far less advanced, which, from my point of view, can best be explained by the much lower frequency at which these occur in patients.

1.2 The succinate dehydrogenase complex and its function in TCA and respiratory chain

The succinate dehydrogenase complex consists of four subunits that are encoded by four different nuclear genes (Table 1). In addition, several additional proteins are expressed to guard correct assembly of SDH at the inner mitochondrial membrane (Table 1). SDH (complex II) differs from the other electron transfer chain complexes in several regards: In contrast to complexes I, III, and IV, SDH lacks components that are encoded by the mitochondrial genome and does not possess direct proton pump activity (11). Thirdly, instead of the more commonly used Nicotinamide adenine dinucleotide (NAD^+), the proton-accepting cofactor of SDH is Flavin adenine dinucleotide (FAD^+) (12).

Most importantly however, complex II (*i.e.* SDH) constitutes a connection between electron transfer chain and the tricarboxylic acid cycle (TCA, a.k.a Krebs cycle) as part of which SDH oxidises its substrate succinate to fumarate (13). Whereas SDHC and SDHD ensure a correct 3D structure of the complex and correct anchoring into the inner mitochondrial membrane, SDHA and B comprise the catalytically active sites of the complex: In parallel to chemical conversion of succinate to fumarate, two electrons are transferred to ubiquinone (12). Under physiological conditions, fumarate will then be further oxidised to malate in the TCGA by the mitochondrial isoform of fumarate hydratase.

Gene name (human)	Gene locus Homo sapiens	Gen locus Mus musculus
SDHA	5p15.33	13 C1
SDHB	1p36.13	4 D3
SDHC	1q23.3	1 H3
SDHD	11q23.1	9 A5.3
SDHAF1	19q13.12	7 B1
SDHAF2	11q12.2	19 A
SDHAF3	7q21.3	6 A1
SDHAF4	6q13	1 A5

Table 1: Overview of SDH and important SDH assembly factor genes and their chromosomal locations in humans and mice. Source: www.ncbi.nlm.nih.gov/gene

1.3 Selected roles of succinate signalling and SDH in physiology and disease

Already decades ago, Hans Adolf Krebs and his co-workers described a selective local accumulation of succinate under hypoxic conditions or upon external perturbation of the tricarboxylic acid cycle (14, 15). Since these initial observations, succinate production and accumulation have been linked to regulation of a growing spectrum of physiological functions. In particular, the discovery of the G-protein-coupled cell surface receptor GPR91 (encoded by the *SUCNR1* gene) and succinate as its ligand have mechanistically established the role of succinate as a paracrine and endocrine signalling molecule (16, 17). Recent scientific evidence has underscored involvement of the succinate-GPR91 axis in regulation of haematopoiesis and immunity (18-20). Of special interest in the context of this thesis project is the observation that the kidney is one of the organs with highest GPR91 expression and, within the kidney, particularly high levels of GPR91 have been detected in epithelial cells of the distal tubules (21). In the kidneys, the succinate GPR91 axis acts as an essential regulator of renin secretion and glomerular filtration as well as arterial blood pressure (22-24). In accordance with this, increased local renal succinate concentration causes glomerular hyper-filtration and hypertension, both early hallmarks in the pathogenesis of Diabetes mellitus. Thus, urinary succinate concentrations have been proposed as a biomarker of this disease (22). Another link between increased succinate concentrations and complications of Diabetes mellitus derives from the detection

of GPR91 in retinal ganglion neurons and increased retinal neovascularisation, the major pathophysiological process in diabetic macula degeneration, upon GPR91 engagement by succinate (25).

The current state of research implies divergent, tissue-specific downstream signalling after GPR91 ligation. It is noteworthy however that, amongst the pathways that have been implicated in GPR91 signalling, is the MAPK/ERK cascade, a classical effector of *HRAS* (please refer to section 1.7 as well) (26).

In addition to GPR91-mediated signal transduction, an alternative mechanism of intracellular "signalling" related to SDH dysfunction has been uncovered by recent studies: Under conditons of intermittent hypoxia/ischemia and consecutive reperfusion, such as acute myocardial infarction and cerebrovascular insult, SDH becomes a source of mitochondrial reactive oxygen species (ROS) production. (27, 28). More precisely, in these pathologies, succinate accumulation in an acutely oxygen-deprived condition and subsequent rapid oxidation by SDH upon restoration of oxygen supply causes reverse electron transfer to the respiratory chain complex I and thereby triggers increased production of free reactive oxygen species (27). The clinical correlate of resulting tissue damage that typically exceeds the core of a non-perfused area is a well-known phenomenon termed ischemia-reperfusion injury and currently investigated as a promising target for pharmacological interference (27). Similarly, SDH-mediated ROS enable macrophages to activate a pro-inflammatory transcriptional program (29).

After initial reports on succinate as a regulator of lipolysis had been contradictory, another physiological function of the "hormone" succinate (independent of GPR91) has recently been dissected by Evanna Mills and co-workers (30-32): In hypothermic mice, succinate production increases (presumably in shivering muscles), and higher systemic levels of this metabolite are selectively incorporated into brown adipose tissue (BAT). Augmented succinate oxidation by SDH results in ROS generation which in turn activate thermogenesis in BAT by uncoupled cellular respiration. In mice, this phenomenon (that can be recapitulated by exogenous supply of succinate to the organism) results in increased energy expenditure and diminished weight gain on a feeding regime that induces obesity in untreated animals (32).

1.4 SDH genes are inactivated in different tumour entities

Bi-allelic germline mutation of *SDHA* constitutes one of the more than 75 genetic defects underlying Leigh Syndrome, a progressive disorder that is typically diagnosed shortly after birth and inevitably fatal within the first few years of life (33, 34). Even though the clinical picture of Leigh Syndrome is in most cases dominated by features of progressive neurodegeneration, the ubiquitous loss of respiratory chain function results in systemic lactate accumulation as well (33).

The major difference between Leigh Syndrome and SDH-associated cancer entities lies in the fact that in the latter, one germline allele is mutated and tumours arise with somatic loss of the second allele. Adults with mono-allelic germline inactivation of *SDHB* show significantly higher plasma levels of succinate than *SDHB* wild type individuals, but these are typically still within reference range limits (35).

When inactivating mutations in the genes encoding succinate dehydrogenase subunits *D, C* and *B* were first described to form the genetic basis of hereditary pheochromocytoma/paraganglioma (Pheo/PGL) syndromes (36-38), it seemed extremely surprising how loss of an enzyme complex that connects two central pathways of eukaryote metabolism could facilitate malignant transformation in a classical tumour suppressor pattern. Over the last 18 years however, all four *SDH* genes and SDH assembly factor 2 (SDHAF2) were shown to be recurrently mutated or deleted in different heritable cancer syndromes and at low frequencies in sporadic tumour types (39-43). In addition, epigenetic silencing and promoter mutations have since been identified as additional mechanism of *SDH* gene inactivation (44, 45). *SDH* genes were also found to encode some of the most frequently downregulated metabolic transcripts across many cancer entities (46, 47). Taken together, these discoveries hint towards SDH dysfunction as a general tumour-promoting principle.

Phe/PGL, gastrointestinal stroma tumour (GIST) and SDH-deficient renal cell carcinoma remain the classical SDH-related tumour entities, but genetic or epigenetic *SDH* gene inactivation have been reported in thyroid cancer, pituitary adenoma, neuroblastoma, pancreatic neuroendocrine tumours and melanoma (11, 41, 45).

1.4.1 In Pheochromocytoma/Paraganglioma, genetic *SDH* loss co-occurs with oncogenic *HRAS* mutation

All four *SDH* genes as well as the gene encoding SDH assembly factor 2 (*SDHAF2*) were demonstrated to function as tumour suppressors in Pheo/PGL, rare tumours of the peripheral neuroendocrine system (36-38, 42, 43).

In 2015, unpublished analyses of TCGA data by the laboratory of Eytan Ruppin (48) concluded a strong association of activating *Hras* mutations, a long-established driver mutation in this tumour type (49), with genetic losses at the SDHB locus in Pheo/PGL (personal communication with Eyal Gottlieb). During the course of my PhD project, the Cancer Genome Atlas project published an in-depth genetic study of this data set , confirming a significant co-occurrence ($p<0.001$) of activating *HRAS* mutations and shallow gene deletions at the *SDHB locus,* but also demonstrating mutual exclusivity between germ line *SDH* mutations and *HRAS* mutations (Figure 1). In addition, almost all *HRAS* mutations within the cohort were mapped to codon 61 (50).

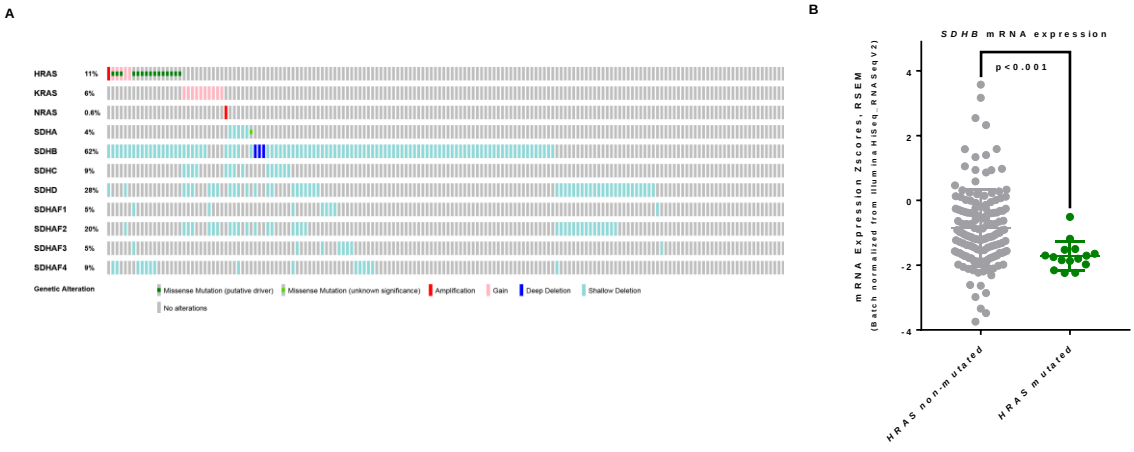

Figure 1: Overview of genetic *RAS, SDH* and *SDHAF* alterations (A) and correlation of *SDHB* transcript levels with *HRAS* mutational status (B) in the provisional TCGA Pheo/PGL data set. Please note that only a single case with *RAS* (*KRAS*) mutation or gain does not carry deletions in any *SDH* gene. Since the data set has only been deposited at the platform as a provisional version, *SDHB* and *SDHD* germline mutations (occuring in 9% and 2% of patients) are not depicted (50). Results have been obtained from http://www.cbioportal.org on 06/01/2019 by the following query: "DATATYPES: MUT AMP GAIN; HRAS; KRAS; NRAS; DATATYPES: MUT HETLOSS HOMDEL; SDHA; SDHB; SDHC; SDHD; SDHAF1; SDHAF2; SDHAF3; SDHAF4". $P<0.001$ for co-occurance of *HRAS* mutations with shallow *SDHB* deletions as well as decreased *SDHB* mRNA levels (51, 52)

1.4.2 SDH-deficient renal cell carcinoma

Renal cell carcinomas (RCC) in general are considered “metabolic diseases”(53). In order to distinguish its unique pathophysiology from other, more common types of kidney cancer, the World Health Organisation has recently introduced SDH-deficient RCC as a formal tumour entity (54). From my point of view, this argues against transferability of gene association studies from more common types of renal cancer to SDH-deficient cancer. In addition, in sharp contrast to clear cell type RCC and papillary RCC that both originate from epithelial cells of the proximal renal tubule (55, 56), immunohistochemical characteristics, including expression of kidney-specific Cadherin (KSP-Cadherin) of SDH-deficient RCC argue for its origin from the distal part of the tubular system (57). SDH-deficient RCC has a typical microscopic morphology that includes cytoplasmatic vacuolisations, neuroendocrine appearance of nuclei and a varying degree of cystic tumour areas (58).

With only about 55-60 cases that have been documented in the scientific literature to date in total, SDH-deficient RCC is an extremely rare tumour type, even if it is probably underdiagnosed (59, 60). Nevertheless, its reliable detection in individual patients has high importance: Since the majority of patients suffering from SDH-deficient RCC carry *SDHB* germline mutations, clinical surveillance for development of SDH-associated Pheo/PGL and GIST as well as genetic investigation of family members can only be initiated after correct diagnosis (59, 60).

Screening of clinical specimens for SDH-deficiency is commonly performed by immunohistochemical staining for SDHB protein expression since upon loss of any *SDH* gene, assembly of the SDH complex is disrupted and SDHB is degraded. In contrast, SDHA remains detectable unless mutations affect this unit in particular (11).

1.5 Oncogenic mechanisms of loss of SDH function and succinate accumulation

Loss or impairment of SDH function leads to intracellular accumulation of its substrate succinate with a broad impact on cellular function: As the reaction

product of alpha-ketoglutarate-dependent dioxygenases, increased succinate concentrations inhibit this vast class of enzymes. Besides other downstream effects, classical paradigms of SDH-deficient tumourigenesis such as stabilisation of Hypoxia-inducible Factor 1alpha as well as impaired DNA and histone demethylase activities are direct consequences (61-63). A more recent addition to the intracellular effects of succinate that are mediated by inhibition of dioxygenases is the evidence for impaired DNA double strand repair capacity of SDH-deficient cancer cells due to inhibited activities of the Lysine-specific demethylases 4A and 4B (encoded by the *KDM4A* and *KDM4B* genes) (64). This mechanism of succinate to increase genetic instability could at least in theory suggest acquisition of additional oncogenic genetic insults by *SDH*-deficient cells.

Another line of research has established GPR91-mediated succinate signalling as a trigger of pro-survival pathways in many different physiological and pathological conditions (26, 65) (please see section 1.3 as well). Therefore, one can at least speculate a tumour-promoting function of para-/auto-/or endocrine succinate signalling *via* GPR91

1.6 Typical metabolic features of *Sdhb*-deficient kidney cells

The laboratory of Professor Gottlieb has generated and extensively characterised two immortalised murine kidney epithelial cell clones that carry the same conditional *Sdhb* allele (*Sdhb*$^{fl/fl}$) as the genetically engineered mouse models used in this thesis (66). In comparison to *Sdhb*-proficient controls, after exposure to Cre *in vitro*, *Sdhb* deleted (*Sdhb*$^{\Delta/\Delta}$) clones displayed a >100-fold accumulation of intracellular succinate, a virtually complete block of oxidative TCA cycle flux at the succinate-to-fumarate conversion as well as decreased basal and maximal mitochondrial respiration (66). Glucose consumption and lactate secretion as markers of glycolytic activity were measured at increased rates in *Sdhb*$^{\Delta/\Delta}$ cells. In a subsequent untargeted metabolomics approach comparing *Sdhb*$^{\Delta/\Delta}$ their counterparts that had not been exposed to Cre (*Sdhb*$^{fl/fl}$), Simone Cardaci, Leon Zheng and their co-workers found the non-essential amino acid aspartate to be one of the most decreased metabolites in the Sdhb-deficient setting. This observation could be validated in human SDH-mutated Pheo/PGLs. Further experimental evidence pointed towards pyruvate carboxylation, a key reaction to

provide the aspartate precursor (and TCA cycle intermediate) oxaloacetate in the SDH-deficient setting, as a selective vulnerability of *Sdhb*$^{\Delta/\Delta}$ cells (66).

Importantly, other recent evidence has similarly revealed biological availability of aspartate as a critical, general limitation in biological systems with disturbed respiratory chain function including hypoxic conditions (67-69).

Throughout this thesis, I have employed succinate accumulation and decreased aspartate abundance as metabolic indications of SDH inactivation in opposite biological directions.

1.7 Oncogenic *HRAS* in tumourigenesis

As outlined above, based on scientific evidence derived from pheochromocytoma and paraganglioma, the mouse models discussed in this thesis combine Cre-mediated deletion of *Sdhb* with activation of transcription of a mutated, oncogenic *Hras*^{G12V} allele (50, 70).

Mono-allelic germline *HRAS* mutations result in the clinical picture of Costello syndrome, which, amongst other typical morphological features, is characterised by a "failure to thrive" (*i.e.* impaired age-based weight gain in affected children) (71, 72). In addition, patients suffering from Costello syndrome show an increased susceptibility towards cutaneous papilloma development, bladder cancer, rhabdomyosarcoma and neuroblastoma (73). Recurrent somatic *HRAS* mutations mainly occur in urological and gynaecological tumours, Pheo/PGL, head and neck tumours and non-melanoma skin cancer (Figure 2).

The *Harvey RAS (HRAS)* gene constitutes one of the classical cellular oncogenes and is in the vast majority of cases activated by somatic, mono-allelic point mutations in codons 12, 13 or 61 that occur at different frequencies in typical *HRAS*-associated tumours (74). According to the recently published TCGA data, most *HRAS* mutations in Pheo/PGL are located in codon 61 (50). The G12V hotspot mutation that has been used throughout this study decreases sensitivity of HRAS for GTPase-activating proteins and thereby causes constitutive activation of cellular signalling cascades downstream of HRAS, of which phosphatidylinositol 3-kinase (PI3K) and mitogen-activated protein kinase (MAPK) pathways are probably

the most studied (74, 75). Acute activation of RAS oncogenes is well established as a trigger of oncogene-induced cellular senescence, a long-term growth arrest of viable cells that can prevent malignant transformation (76). Therefore, senescence effectors need to be inactivated or bypassed to enable RAS-driven tumourigenesis (77).

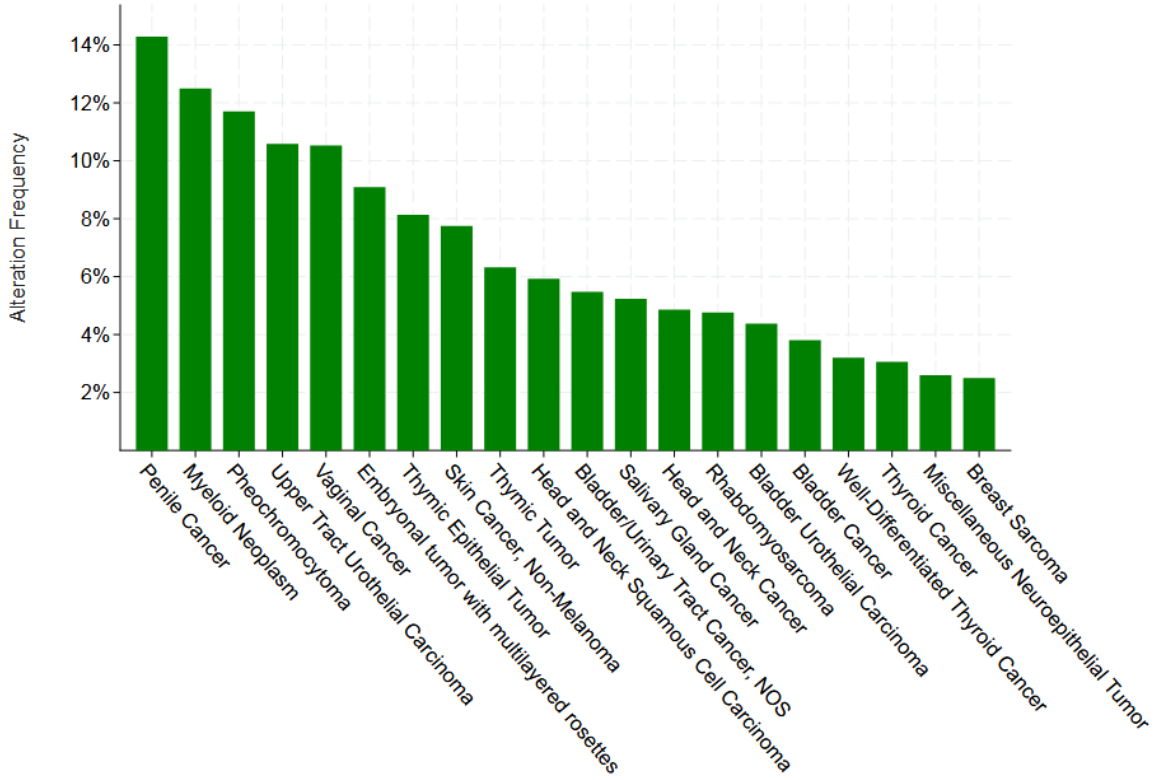

Figure 2: Cancer entities with recurrent *HRAS* (>2% of cases) mutations in data sets available through the cBioPortal platform. Results were downloaded from http://www.cbioportal.org on 05/01/2019. (51, 52)

The fact that *RAS* gene mutations, as discussed above, typically follow a mutational pattern of classical oncogenes has for many decades determined the view on RAS genes as molecular switches that become constitutively activated by mutations at early stages of cancer development. However, more recent work has clearly established gene dose effect and expression levels of mutated *RAS* genes to play an important role in tumour development and maintenance. More specifically, genetic copy number gains and loss of wildtype alleles at the corresponding *RAS* loci were shown to be selected for during $HRAS^{G12V}$ and KRAS driven tumourigenesis in different organs (78-81). In addition, Kerr *et* al. found that distinct metabolic phenotypes of murine lung carcinomas with homozygous versus heterozygous *Kras* mutations result in a much more aggressive biological behaviour (80).

It is also noteworthy that in the genetically engineered mouse models studied as part of this thesis project, the mutated *Hras* construct has been inserted into the endogenous *Hras* locus (70). As a consequence, mutated *Hras* is not ectopically overexpressed, but downstream effects of constitutive HRAS signalling should only become apparent after Cre activity in tissues with substantial *Hras* gene expression under physiological conditions. Inclusion of animals carrying two mutated *Hras* alleles into the experimental cohorts provides an option of studying gene dose effects as well as $HRAS^{G12V}$ signalling in the absence of wild type HRAS in addition.

1.8 Aims of my PhD thesis project

More than 15 years after the discovery of bi-allelic SDH gene inactivation in Pheo/PGL, additional genetic events and tissue-specific factors that contribute to SDH-deficient oncogenesis remain to be elucidated and adequate preclinical models are still lacking (36, 37, 82).

The first goal of my thesis project was to phenotypically characterise genetically engineered mice with kidney-specific *Sdhb* inactivation in order to develop a model of SDH-deficient renal cell carcinoma.

Secondly, employing newly designed experimental platforms for untargeted metabolomics, we have investigated kidney tissues and bio-fluids obtained from these *Sdhb*-deficient mice with the aim to identify new metabolic biomarkers of SDH-deficient tumours.

Finally, we set out to gain insights into tissue-specific vulnerabilities towards SDH loss by studying consequences of stochastic *Sdhb* inactivation in small cell fractions of peripheral murine tissues.

2 Materials and Methods

2.1 Materials

2.1.1 Mouse models

2.1.1.1 General information

All mouse experiments were carried out in mixed genetic backgrounds but within highly inbred colonies.

Constitutive, kidney-specific, or inducible gene targeting in multiple organs was achieved by Cre-*loxP*-mediated recombination (83, 84). This experimental system enables site-specific modifications in virtually any gene of interest *in vivo* and can circumvent toxicity as well as embryonic lethality that are commonly associated with genetic germline alterations (85). Most importantly, Cre-*loxP*-based genetically engineered mouse constructs can model spontaneous acquisition of distinct somatic gene alterations that typically occur in certain cancer entities (85).

To summarise briefly, the P1 bacteriophage recombinase "Cre" (Causes Recombination) recognises "*loxP*" (locus of X(cross)-over in P1) DNA sequences that are not known to naturally occur in mammalian genomes. In the presence of Cre activity, "floxing", *i.e.* introduction of two *loxP* sites into a DNA sequence, typically at non-transcribed positions, will cause rearrangement of the intermittent, otherwise functionally non-compromised DNA. If both *loxP* sites have the same orientation, the genomic information between them will be excised by Cre, whereas an inversion will occur between two *loxP* sites in opposite orientation (86). The Cre-*loxP* principle can either be applied to abrogate gene function (*e.g.* by Cre-mediated deletion of Sdhb exon 3 in mice carrying "floxed" *Sdhb* alleles [$Sdhb^{fl}$), see 2.1.1.2] or to induce gene expression by Cre-dependent excision of a transcriptional 5' stop codon ("lox-stop-lox" [LSL] *e.g.* of Rfp^{LSL} or/and $Hras^{LSLG12V}$ alleles, see 2.1.1.2) (87).

Different experimental tools have been designed in order to control tissue-specificity, timing and magnitude of Cre activity: Transcriptional regulation of *Cre* can be achieved by coupling the *Cre* transgene to a tissue-specific promoter (*e.g.*

the *Cadherin 16* promoter in this study) or, if ubiquitous Cre activity is desired, inserting it into a gene locus with broad expression (e.g. *Rosa26*). Alternatively, timed, short-term nuclear translocation (and activity) of a constitutively-expressed, but otherwise cytoplasmic (*i.e.* inactive) Cre-receptor-complex (*e.g.* CreERT^2) can be induced by application of exogenous ligands in a dose-dependent manner (*e.g.* tamoxifen in the *RosaCreER^{T2}* system) (88).

Constitutively active Cre constructs are more likely to provide a strong, constant, durable Cre activity and therefore to enable recombination of the target gene at high efficacy in a Cre-expressing tissue. However, if the target gene is essential to organ function, its complete abrogation might be toxic to the whole organism at an early stage of embryonal development and thus prevent mechanistic studies in adult animals. On the contrary, ligand-inducible Cre expression holds the advantage of acutely inducing desired genetic alterations in thitherto healthy animals at defined ages and to "titrate" recombination efficacy to a desired level. It has to be considered though that short term Cre activation may be insufficient to achieve substantial target gene recombination especially if both alleles of a gene need to be recombined in the same cell. In addition, the need for ligand application introduces an additional source of biological variation into the experimental workflow.

2.1.1.2 Genetically engineered alleles used in this this thesis

Allele name	Abbreviation	Source	Reference
Tg(Cdh16-cre)91Igr	*KspCre*	Jackson Laboratory	(89)
Gt(ROSA)26Sor$^{tm2(cre/ERT2)Brn}$	*RosaCreER^{T2}*	Dr David Adams, Wellcome Sanger Institute	(90)
Sdhb$^{Tm1cBea-4.8C}$	*Sdhb^{fl}*	Generated at CRUK Beatson Institute	(66)
Hras^{tm1Khai}	*Hras^{LSLG12V}*	Dr. Kevin Haigis (*via* Prof. Owen Sansom, CRUK Beatson Institute)	(70)
Gt(ROSA)26Sor^{tm1Hjf}	*Rfp^{LSL}*	European Mouse Mutant Archive (with permission of Prof. Hans Jörg Fehling)	(91)

Table 2: Details, abbreviations and references for genetically engineered mouse alleles employed in this thesis.

KspCre

In this construct, a *Cre* transgene has been inserted under transcriptional control of a *Cadherin 16* (*Cdh 16*, "Ksp cadherin") promoter with the aim of kidney-specific, constitutive gene targeting (89). During murine embryogenesis, *CDH 16* is expressed in the developing genitourinary system of both sexes, whereas in adult mice, *CDH 16* expression is confined to the renal tubular system and most pronounced from the loop of Henle to the collecting duct (89).

RosaCreER^{T2}

The *Rosa26 (Gt(ROSA)26Sor)* locus, located on mouse chromosome 6, has been widely used for constitutive expression of transgenes as it possesses a unique set of features: It is almost ubiquitously expressed throughout development and in adult mouse tissues at substantial levels, but its function remains to be elucidated and, most importantly, its disruption does not result in overt phenotypes (92, 93). The fact that *Rosa26* can easily be subjected to gene targeting constitutes an additional advantage from the technical point of view (87).

In the *RosaCreER^{T2}* system, the *Rosa26* promoter drives constitutive expression of a fusion protein that consists of the recombinase Cre and a mutated human oestrogen receptor ligand-binding domain with only very low affinity for naturally occurring oestrogens (90). Application and consecutive binding of the synthetic oestrogen analogue tamoxifen, or, to a much higher degree, its active metabolite 4-hydroxytamoxifen (4-OHT), result in temporary nuclear translocation of the fusion protein and Cre activity on the genome (88). RosaCreER^{T2} exhibits only a very low degree of "background" recombination that was found insufficient to induce skin neoplasia in the absence of tamoxifen (90). Recombination efficacies and dynamics of *RosaCreER^{T2}* systems are variable between peripheral organs with particularly high recombination levels in the gastrointestinal and haematopoietic system (90). The observation that *RosaCreER^{T2}* fails to efficiently induce recombination in the brain has been explained by low levels of transgene expression in the CNS (94), even though another study suggested low achievable ligand (*i.e.* 4-OHT) concentrations in this compartment after systemic tamoxifen application as the major cause instead (95).

In summary, induction of target gene recombination by the *RosaCreER^{T2}* method typically results in a stochastic, mosaic pattern of recombination in most peripheral tissues depending on target gene features, *RosaCreER^{T2}* expression levels, and, most importantly, tamoxifen application scheme and resulting 4-OHT concentrations in different organs (88, 94).

Sdhb^{fl}

An *Sdhb* targeted allele was generated by the Transgenic Production Facility of the CRUK Beatson Institute (Head: Dr. Douglas Strathdee) by introducing *loxP* sites 5' and 3' of *Sdhb* exon 3 as previously described and characterised *in vitro* (66). Cre-mediated recombination of *Sdhb$^{fl/fl}$* genomes will result in deletion of the functionally essential *Sdhb* exon 3, hence entirely abrogating SDHB protein expression (66). In addition, Cre activity generates a premature translational stop codon at the start of *Sdhb^{fl}* exon 5. It is reasonable to assume that this premature stop codon would result in nonsense-mediated decay of the truncated *Sdhb^{fl}* mRNA and therefore substantially lower overall *Sdhb* transcript levels after Cre-mediated recombination than in the corresponding wildtype condition (personal communication with Dr. Douglas Strathdee).

Rfp^{LSL}

Originally inserted into the *Rosa26* locus to function as a flow cytometry- as well as immunohistochemistry-based reporter of Cre activity, this transgene encodes a fusion protein of two covalently linked, genetically modified red fluorescent protein units (91). By a sequence of two consecutive recombination events in the presence of Cre activity, the otherwise non-transcribed *Rfp* allele is "activated" by inversion and excision of a stop site. The necessity of a genetic inversion to activate transcription of *Rfp*^{LSL} prevents "read through" the stop codon in the absence of Cre activity (91). Due to their shared location on the *Rosa26* locus, *RosaCreER*$^{T2+}$, *Rfp*^{LSL} double transgenic mice can only be generated at heterozygous states for both alleles.

Hras^{LSLG12V}

This allele was generated by introduction of a transcriptional stop site that is flanked by *loxP* sites (*i.e.* a LSL construct) into the first exon of the murine *Hras* locus 5' of an oncogenic Glycine to Valine point mutation at *Hras* codon 12 (70). In the absence of Cre activity, this construct results in a lack of (wildtype) *Hras* transcription from this allele. As reported for *Hras* and *Nra*s, but not *Kras* knockout mice, *Hras*$^{LSLG12V/LSLG12V}$ homozygous mice, for which an entire lack of wildtype HRAS protein expression is predicted, are viable and without overt phenotype (96).

2.1.2 Chemicals, Reagents, Kits, Antibodies

Reagent name	Supplier
Acetone	Fisher Chemicals
Acetonitrile (HPLC grade)	VWR Chemicals
Clear Ultrasound Gel	Henleys Medical Supplies Limited
Corn oil	Sigma Aldrich
Dimethyl Sulfoxide (DMSO TC-grade)	Sigma Aldrich
DNAse/RNAse free water	Qiagen
Ethanol (pure)	VWR Chemicals
Glass beads, acid-washed (425-600 µm)	Sigma Aldrich
IsoFlo® Isoflurane 100 w/w%	Zoetic Inc., Kalamazoo, USA
Methanol (HLPC grade)	Fisher Chemicals
Neutral buffered formalin (10%)	Solmedia
Tamoxifen	Sigma Aldrich
Veet Hair Removal Crème Sensitive Skin	RB Healthcare

Table 3: List of reagents and chemicals

Name	Supplier
Autosampler Vial Screw Thread Caps	Thermo Fisher Scientific
Clear Screw Top Vials (12 x 32 mm)	Thermo Fisher Scientific
EDTA-coated Microvettes (CB 300 K2E)	Sarstedt
Insert Standard Opening 0.05 ml (27.5 x 4 mm)	Kinesis
Lithium-Heparine Microtubes LH11.3	Sarstedt
QIAshredder	QIAGEN
RNeasy Mini Kit	QIAGEN

Table 4: List of commercial kits and consumables

Antigen	Supplier	Catalogue number	Dilution
γH2AX (Phospho-Histone H2A.X [Ser139])	**Cell Signalling**	**9718**	**1:50**
Ki67	Thermo Fisher Scientific	RM-9106	1:100
aRFP	Tebu-bio	600-401-379	1:100
SDHB	Abcam	ab14714	1:100

Table 5: Details of primary antibodies for immunohistochemistry

2.1.3 Research equipment

Name	Manufacturer
CryoCooler	OPS Diagnostics
CryoGrinder Kit 230V	OPS Diagnostics
Mouse Anaesthesia Unit	Vet Tech Solutions, Fortec
NanoDrop 2000c Spectrophotometer	Thermo Fisher Scientific
Nikon PowerShot G12 Digital Camera	Nikon
Centrifuge 5427R	Eppendorf
Thermomixer compact	Eppendorf
Vevo 3100 Preclinical Imaging System with MX550D transducer	FUJIFILM VisualSonics

Table 6: List of research equipment

2.1.4 Software packages

Name, Version	Manufacturer/link
cBioPortal for Cancer Genomics, Version 1.18.1	Multi-institutional team; www.cbioportal.org
CompoundDiscoverer, Version 2.1	Thermo Fisher Scientific
EndNote X8	18.2.0.11343
Halo, Version 2.2	indica labs
Office Professional Plus 2016, Version 16.0.4266.1001	Microsoft
Prism, Version 7.02	GraphPad
Sante DICOM viewer, Version 4.0.8	Santesoft
TraceFinder, Version 3.2.368.22	Thermo Fisher Scientific
Wellcome Sanger Institute Mouse tracking system (Latest version: 2018.9.4_221733)	https://beatson.mig.sanger.ac.uk/mouse/user_home.do
Vevo LAB, Version 1.7.1	FUJIFILM VisualSonics

Table 7: Commercial software packages and online resources

2.1.5 Human GIST tissue samples

Fresh frozen GIST tissue samples were collected by the National GIST Tissue Bank (Royal Marsden NHS Foundation Trust, London, UK) after approval from Newcastle and North Tyneside Research Ethics Committee and individual patient consent. After approval of a project-specific application to the Biobank, 32 specimens were obtained for our research and extracted as outlined in section 2.2.5.4. Initial analyses revealed a dramatically altered metabolic profile of samples that had been accidentally thawed before final cryo-conservation at the GIST Tissue Biobank (n=12, not shown) and two additional fibrotic tissue samples (for which adequate cryogrinding was not achievable). Therefore, a total number of 8 SDH-deficient and 10 SDH wildtype GIST samples (7 of which carrying cKIT and 3 PDGFRα [platelet-derived growth factor receptor α] mutations respectively) were included in subsequent analyses.

2.2 Methods

2.2.1 Animal work

All experimental procedures involving mice were carried out under the project licence "Mouse Models of Human Cancer" (PPL Number 70/8645) of Dr. Karen Blyth, Head of Transgenic Models at the CRUK Beatson Institute) and my personal licence (number I889D8F90) in accordance with UK Home Office guidelines, the Animals (Scientific Procedures) Act 1986 and the Directive of the European Parliament and of the Council of 22 September 2010 on the protection of animals used for scientific purposes (2010/63/EU).

2.2.1.1 Breeding, maintenance and general procedures

Mice were bred and maintained on a twelve hours dark-light cycle at the CRUK Beatson Institute animal facility in individually ventilated (breeding stocks) or regular cages (experimental cohorts). Aiming for comparable Cre levels in all animals of a mouse colony (*i.e.* at the heterozygous state for *Cre*), mice carrying *Cre* transgenes were only bred to *Cre* negative mice. Standard diet consisted of ad libitum food and water intake. General maintenance, sampling (ear notch) for genotyping and tamoxifen injections were carried out by staff of the Biological Services Unit. Genotyping was performed on ear tissue by Transnetyx Inc. (Cordova, Tennessee, US). Animal-related tasks such as matings and internal transfers were requested through the web-based Wellcome Sanger Institute Mouse tracking system accessible from the CRUK Beatson Institute Intranet.

Animals were frequently checked by me and staff of the Biological Services Unit for general health concerns and endpoints as defined in model-specific standard operating procedures.

2.2.1.2 Sampling of specimens

Animals were weighed and humanely killed according to Schedule 1 protocol by asphyxiation with carbon dioxide (CO_2) followed by exsanguination (cardiac puncture) or by cervical dislocation.

In *KspCre*$^{+}$ mice, weight of kidneys (wet weight) was determined on a fine scale. Whole blood (in EDTA-coated microtubes) and tissues of interest were immediately snap-frozen in dry ice and stored at -80ºC until further analysis. Plasma was obtained by centrifugation of blood in Heparin micro tubes for 10 min at 2.500 g at room temperature and subsequent transfer of supernatant to a fresh Eppendorf tube before snap-freezing in dry ice and storage at -80ºC.

Tissues for (immuno-)histological analyses were immediately fixed in 10% neutral buffered formalin for at least one day at room temperature before further processing by the Histology Service at the CRUK Beatson Institute.

2.2.1.3 Monitoring of water intake

Mice and unopened PVC water pouches were weighed before single mice were transferred to individually ventilated cages. After a total duration of five days, end weights of water pouches and mice were measured. Water consumption rates (WCR) were calculated (in g/g body weight/day) for individual animals as follows:

$$WCR = \Delta\ weight_{water\ pouch}/(mean\ mouse\ body\ weight_{start\text{-}end})/5\ days$$

As outlined in Figure 23, spontaneous loss of water from the watering system into empty cages was measured to be negligible.

2.2.1.4 Kidney ultrasound

Sonographic kidney studies were performed under continuous inhalation anaesthesia with isoflurane. Mice were kept on a heated body warming plate during examinations and vital parameters (heart rate and respirator rate) were monitored continuously. Typical flow levels were 0.8 for medical air, 4 for isoflurane anaesthesia induction and 2-2.5 for isoflurane anaesthesia maintenance. Once the mouse to be examined had reached sufficient anaesthesia (as evidence by loss of defensive reflexes and calm breathing pattern), abdominal coat was removed using Nair hair removal crème. Subsequently, anaesthesia was induced again before switching to maintenance on the heated examination table. Both kidneys were scanned in cranio-caudal direction using pre-warmed ultrasound gel and at least two image loops per kidney electronically documented. Mice were manually warmed and clinically observed until fully awake and

recovered at the end of the procedure. Kidney morphologies with regards to cyst detection were scored as outlined in Table 11.

2.2.1.5 Induction of Cre activity in the *RosaCreER^{T2}* model

Tamoxifen was dissolved in 10% ethanol, 90% corn oil to a final concentration of 10 mg/ml), stored in amber glass bottles at -20 C and pre-warmed in a water bath before application. Adult mice of >20ºg body weight received a single intraperitoneal (i.p.) injection of tamoxifen at doses of 80 mg/kg, 50 mg/kg or 30 mg/kg body weight depending on the experiment by specifically trained animal facility staff (Table 8).

Induction scheme	**Tamoxifen dose** (mg/kg body weight)
"high" dose	80
"low" dose	30
"medium" dose	50

Table 8: Designation of three different transgene induction dosis schemes tested in *RosaCreER^{T2+}*, *Sdhb^{fl}*, *Hras^{LSLG12V}* mice

2.2.1.6 Scoring of proliferative skin changes

The degree of skin tumour burden in the *RosaCreER^{T2}* model was scored by measuring diameters at all typical locations if an animal had reached a clinical endpoint or the defined end of observation time as given in Table 15. A total skin score per animal was calculated as the sum of all values obtained for individual locations.

2.2.2 Histology and immunohistochemistry

All histological specimens were generated and processed by the Histology Facility of the CRUK Beatson Institute (head: Colin Nixon). FFPE blocks of kidneys (*KspCre^{+}* model) or tissue slides stained for H&E or PAS (*RosaCreER^{T2}* model) were mailed to Dr. med. Markus Eckstein (Institute of Pathology, University Hospital Erlangen, Friedrich-Alexander-Universität Erlangen-Nürnberg, Erlangen, Germany) for morphological analysis. IHC for SDHB was performed by Dr. Markus Eckstein following the internally established and validated diagnostic protocol (*i.e.* using the identical SDHB-directed antibody) for human kidney specimens. All other IHC stainings were performed by the CRUK Beatson Institute Histology Facility

following established standard protocols using primary antibodies as outlined in Table 5. For semi-automated quantification of IHC, stained slides were scanned at a magnification of 20x and analysed by Elaine MacKenzie using the Halo Image quantification software package following instructions of the manufacturer. Results were expressed as the percentage of (positive cells per area)/(total cells per area) for nuclear antigens and (stained tissue area)/(total tissue area) for cytoplasmic antigens. Representative images were compiled into figures employing the built-in Figure Maker tool of the software package.

2.2.3 RNA extraction from mouse kidneys

Snap-frozen kidney tissue of eight representative mice per genotype was cryo-grinded using the CryoCooler and CryoGrinder following instructions of the manufacturer. Between 9 mg and 14.5 mg of frozen tissue per kidney sample were homogenised (QIAshredder) and RNA was immediately extracted following manufacturer's instructions for RNeasy Mini Kit including on-column DNA digestion. After product elution in RNAse-free water, RNA concentration was determined on a NanoDrop 2000c Spectrophotometer and adjusted to 20 ng/ml in RNAse-free water before samples were stored at -80ºC.

2.2.4 RNA sequencing

RNA quality analysis and RNA sequencing were performed by William Clark (Molecular Technology Services) at the CRUK Beatson Institute. Technical information and results described in this section have been provided by William Clark. After assessment of RNA quality on an Agilent 2200 TapeStation system using RNA ScreenTape, six biological replicates per genotype with appropriate estimated RNA integrity number [RIN^e] values were selected for RNA sequencing. Results values obtained for 16 kidney samples are exemplified in Figure 3.

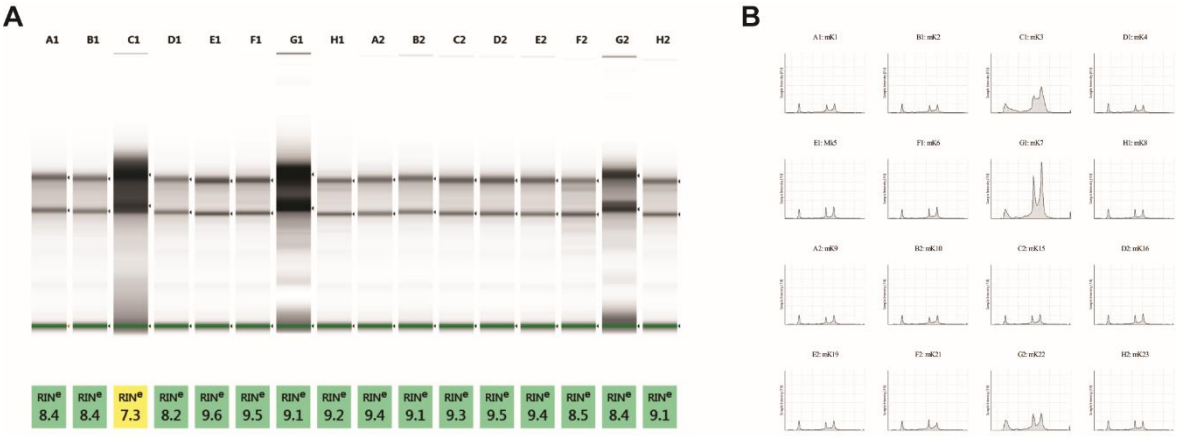

Figure 3: Exemplary results of mouse whole kidney RNA quality analysis

Libraries for cluster generation and DNA sequencing were prepared as described by Fisher and co-workers (97) using the Illumina Stranded TruSeq mRNA LT Kit. Quality and quantity of the DNA libraries were then analysed on an Agilent 2200 TapeStation (D1000 ScreenTape) and Qubit (Thermo Fisher Scientific) respectively. Cluster generation and sequencing were carried out on an Illumina Next Seq 500 using the High Output 75 cycles kit (2x36cycles, paired end reads, single index).

Quality analyses of RNA sequencing raw data files were performed by Robin Shaw (Molecular Technology Services) at the CRUK Beatson Institute using fastqc version 0.11.7 (98) and fastq_screen version 0.12.0 as described (99) and Jonatan Fernández García at the Technion, Haifa. Technical information discussed in this paragraph has been provided by Robin Shaw. RNA sequencing paired-end reads were then aligned to the GRCm38 version of the mouse genome (100) and annotated using HiSat2 version 2.1.0 (101, 102). Expression levels were determined and statistically analysed by a combination of HTSeq version 0.9.1 (103), the R environment version 3.4.4 (available online at https://www.R-project.org) utilizing packages from the Bioconductor data analysis suite (104) and differential gene expression analysis based on the negative binomial distribution using the DESeq2 package version 1.18.1 (105).

2.2.5 Metabolite extraction from body fluids and tissues

2.2.5.1 Metabolite extraction solution

- 50% HPLC grade methanol
- 30% HPLC grade acetonitrile
- 20% MilliQ water

2.2.5.2 General procedure

All biological specimens were snap-frozen and stored at -80 ºC until further use to minimise alterations in metabolite abundancies *ex vivo*. Extractions were coordinated with mass spectrometry capacities to avoid long-term storage of sample extracts before analysis. Metabolite extraction buffer was prepared freshly for each experiment, chilled to -20ºC before use and stored on ice during extractions. Samples were stored on ice throughout extraction procedures. Centrifugations as well as automated vortexing were carried out at 4 ºC.

For untargeted metabolomics, a proportionate pool of all biological samples of the experimental batch to be analysed was prepared before extraction. An aliquot of this sample pool was extracted in triplicate together with the individual samples to later serve as internal reference for technical quality of compound detection, for batch effect correction and for acquisition of compound fragmentation data (please refer to section 2.2.6). Negative controls comprised extraction buffer aliquots and procedure blanks.

A selection of stable isotope-labelled metabolites (outlined in Table 9) was added to extraction buffer preparations for untargeted metabolomics as an internal standard mix to enable potential further normalisation approaches for individual metabolites of interest.

Standard Name	Supplier	Conc. (µg/l)
L-Lysine:HCl ($^{13}C_6$, $^{5}N_2$)	Sigma Aldrich	62.5
L-Methionine ($^{13}C_5$)	Cambridge Isotope Laboratories	10
L-Ornithine:HCl ($^{13}C_5$)	Cambridge Isotope Laboratories	62.5
Citric Acid ($^{13}C_6$)	Sigma Aldrich	100
Sodium Pyruvate ($^{13}C_3$)	Omicron Biochemicals	20
Fumaric Acid (1,4 $^{13}C_2$)	Sigma Aldrich	200
Succinic Acid (D_4)	Cambridge Isotope Laboratories	62.5
D-Galactose ($^{13}C_6$)	Omicron Biochemicals	3000
D-Glucose-6-Phosphate, Disodium Salt Hydrate ($^{13}C_6$)	Omicron Biochemicals	60
Adenosine (Ribose-$^{13}C_5$)	Omicron Biochemicals	1.25
2'-Deoxyadenosine-$^{13}C_{10}$,$^{15}N_5$-monophosphate, Sodium Salt	Sigma Aldrich	50
Acetoacetyl-Coenzyme A ($^{13}C_4$), Lithium Salt Hydrate	Sigma Aldrich	1250
Calcium Pantothenate: H_2O Beta-Alanyl ($^{13}C_3$, ^{15}N)	Cambridge Isotope Laboratories	0.6

Table 9: List of stable isotope-labelled internal standards added to biological samples for untargeted metabolomics analysis. Final concentrations in extraction buffer are given. All standards were dissolved in deionised water and stored at -80ºC.

2.2.5.3 Extraction of plasma and urine

Thawed samples were centrifuged for 1 min at maximum speed (18.213 g) in a table top centrifuge to pellet particles and 5 µl of fluid were transferred to a chilled Eppendorf tube. Cold extraction buffer containing internal standards was added to achieve a final dilution of 1:100 for plasma specimens (*i.e.* addition of 495 µl extraction buffer) and 1:50 for urine samples (245 µl extraction buffer). Tubes were vortexed by hand for 30 seconds, then automatically for 10min at 4°C at 1.400 rpm (Thermomixer) and for 30 seconds by hand again. After centrifugation for 10 min at 18.213 g, the clear supernatants were transferred to a fresh cool Eppendorf tube and stored at -80ºC overnight to aid complete precipitation of residual protein or salt contaminations. Finally, extracts were centrifuged again for 10 min at maximum speed, supernatants transferred to mass

spectrometry glass vials (containing inserts for sample volumes <200 μl) and stored at -80°C until analysis.

2.2.5.4 Extraction of tissues

Snap-frozen tissue samples were grinded using the CryoCooler and CryoGrinder following instructions of the manufacturer. Aiming for an amount of approximately 15 mg, a grinded aliquot was quickly weighed on a fine scale and transferred to a fresh, chilled Eppendorf tube. Appropriate volumes of cold extraction buffer containing internal standards for untargeted metabolomics was added to achieve a final extraction ratio of 20 mg/ml:

$Volume_{extraction\ buffer}$ (μl) = $Mass_{tissue\ aliquot}$ (mg) x 50.

Add a small amount of inert glass beads were added to the mixture to increase efficacy of tissue disintegration during subsequent steps. Tubes were vortexed by hand for 30 seconds, then automatically for 10min at 4°C at 1.400 rpm (Thermomixer) and for 30 seconds by hand again. After centrifugation for 10 min at maximum speed (*i.e.* 18.213 g), the clear supernatants were transferred to a fresh cool Eppendorf tube using a 200 μl pipette (to avoid carry-over of glass beads to the next steps). Extracts were stored at -80 °C overnight to aid complete precipitation of residual protein and salt contaminations. Finally, tubes were centrifuged again for 10 min at 18.213 g, clear supernatants transferred to mass spectrometry glass vials and stored at -80°C until analysis.

2.2.6 Metabolomics

Liquid chromatography-coupled mass spectrometry of body fluids and kidney extracts was performed by Dr. David Sumpton or Niels van den Broek, Metabolomics Facility at the CRUK Beatson Institute (Head: Dr. Gillian MacKay). Technical information in this section was provided by Dr. David Sumpton.

Mass spectrometry was conducted using a UltiMate 3000 HPLC system (ThermoFisher Scientific) and a Q Exactive Plus Hybrid Quadrupole-Orbitrap Mass Spectrometer (ThermoFisher Scientific). The HPLC setup consisted of a SeQuant ZIC-pHILIC 5 μm polymer column (150 x 2.1 mm, Merck Millipore), with a SeQuant ZIC-pHILIC guard column (20 x 2.1 mm, Merck Millipore). The initial

mobile phase contained 20% 20 mM ammonium carbonate (pH 9.2) and 80% acetonitrile. Sample extracts were stored at 4°C in an auto-sampler before 5µl were injected into the system. Metabolites were separated over a 30 min mobile phase gradient decreasing the acetonitrile content to 20% at a flow rate of 100µl/min and a column temperature of 45°C. The total analysis time was 40 minutes per sample. All metabolites were detected across a mass range of 75-1000 m/z at a resolution of 70.000 (at 200m/z), with electrospray ionization (ESI) and polarity switching to enable detection of both positive and negative ions in the same analytical run.

Aiming at improving confidence in compound annotation (*i.e.* metabolite identification), a specimen pool (comprising an extracted mixture of all biological samples of the batch, please refer to 2.2.5) was analysed twice using the same HPLC conditions, but running the mass spectrometer once each in single negative and positive ionisation mode and using data dependent fragmentation (ddMS2). This approach combines a high accuracy of peak quantification in individual biological samples with an increased confidence in compound annotation due to the incorporation of fragmentation data into algorithms to assign a metabolite identity to a certain peak. MS2 data redundancy is reduced by avoiding to record fragmentation spectra for identical compounds in many individual samples and detection time can be entirely dedicated to peak scanning. Furthermore, this strategy allows applying different fragmentation strategies with reasonable experimental effort to maximise biological information. In addition, the extracted sample pool (see 2.2.5) served as a technical quality control (QC) and was repeatedly measured every ten sample injections throughout the acquisition of the randomised biological extracts. Lock masses were used. Data were acquired with Thermo Xcalibur software.

Raw data obtained for untargeted analyses were processed by Dr. David Sumpton using the CompoundDiscoverer software package. Retention times and masses were aligned across all sample data files with maximum tolerances of 2 min and 5 ppm. Unknown compound detection (minimum peak intensity 10^6) and grouping of compound adducts were carried out across all samples with a mass tolerance 5 ppm and RT tolerance of 0.7 min. Missing values were filled using the fill gap feature of the software package (mass tolerance 5 ppm, signal/noise threshold 1.5). Within Compound Discoverer, data were corrected for batch effects using

the QC replicate injection data and a QC-based area correction regression model (cubic spline regression, thresholds of >50% QC coverage and <30% RSD).

An additional data normalisation strategy that we applied only to urine samples to control for different urine concentrations is discussed in section 4.2.3.

Compound annotation (i.e. metabolite identification) was achieved by matching the mass, retention time and fragmentation spectrum of an observed peak to an in-house database generated using metabolite standards (including a commercially purchased Mass Spectrometry Metabolite Library [Sigma Aldrich]), mass tolerance 5 ppm, retention time tolerance 2 min). Peak annotations were further confirmed using mzCloud database search (ddMS2, available online at https://www.mzcloud.org, precursor and fragment mass tolerance of 10 ppm, match factor threshold 50).

For targeted quantification of metabolites of interest, the experimental settings was largely identical except for a decreased run time of 22.2 minutes due to a shortened chromatography (15 min). After LC-MS, metabolites were identified by the exact mass of the corresponding singly-charged ion, the preferred ionisation mode and comparison of retention times to the metabolite library of the CRUK Beatson Institute using the TraceFinder Software package. Total peak areas at the appropriate retention time were then compared between biological samples as a measure of metabolite abundancies.

2.2.7 Statistical approaches

The author and his co-workers were not blinded with regards to genotypes, transgene induction schedules or treatment schemes of mice. Animals were not randomised and numbers for biological replicates were not statistically predetermined in experiments. All animals received identical care in an unbiased fashion by animal technicians and myself with the exception of mice approaching clinical endpoints undergoing more frequent monitoring in accordance with local guidelines.

Statistical analyses of mouse survival data, descriptive parameters of mouse models, immunohistochemistry quantifications and targeted metabolomics data

were performed using Excel and Prism software packages. For pairwise comparisons of data sets derived from two different genotypes, I employed the two-sided unpaired Welch's unequal variances t-test under the assumption of an underlying normal distribution of the biological parameters. For comparison of ordinal skin score sum values between genotypes in the *RosaCreER^{T2}* model (chapter 5), the Mann–Whitney *U* test was employed. P values of <0.05 were considered statistically significant and are either depicted as numbers or indicated as "*" in the respective sections/figures. All error bars reflect standard deviations. To test for significant differences in survival, the Log-rank (Mantel-Cox) test was used.

Processing and statistical analysis of RNA sequencing data is illustrated in section 2.2.4 and included p value adjustment for FDR by the procedure as originally proposed (106). The number of six biological replicates for each of the four genotypes analysed was chosen for cost effectiveness as the kits used in the procedure could each accommodate a maximum of 24 biological samples.

For comparisons between genotypes in untargeted metabolomics experiments, multiple student's t-tests and FDR adjustments of p values were performed using the built in statistical tools of the CompoundDiscoverer software package. Compounds with FDR-adjusted p values <0.05 were considered discoveries. Principal component analyses coordinates of centred, transformed peak areas were extracted from the CompoundDiscoverer software package and displayed graphically using GraphPad Prism.

3 Characterisation of a genetically engineered mouse model of SDH-deficient renal cell carcinoma

3.1 Introduction

Even though most likely underdiagnosed, with only approximately 55-60 primary cases described in the scientific literature to date, SDH-deficient RCC has to be considered as an extremely rare cancer entity (59). In contrast to the two most common two most common subtypes of RCC, clear cell-type RCC and papillary RCC (type 1), which both develop by malignant transformation of epithelial cells in the proximal renal tubule (55), the currently available scientific evidence suggests that SDH-deficient RCC originates from the distal part of the nephron (57). The WHO has recently recognised the unique morphology and molecular pathology of this tumour type by formally introducing SDH-deficient RCC as a distinct RCC entity into its disease classification system (54). In turn, this means that results obtained in clinical trials as well as large-scale genetic profiling and gene expression studies from other, more common RCC subtypes cannot simply be extrapolated to the biology of SDH-deficient RCC. On the contrary, faithful model systems as well as in-depth studies of collaborating molecular events in this rare cancer type (but not other types of RCC) are needed to improve our understanding of SDH-deficient RCC. The only large scale genetic profiling data set containing a substantial number of SDH-deficient tumour samples is the recently published TCGA study of Pheo/PGL (50). In line with earlier findings (48), this study shows a strong correlation between activating mutations in the *HRAS* gene and genetic deletions at the *SDHB* locus (50). We have therefore designed a genetically engineered mouse model that combines knockout of the essential *Sdhb exon 3* with expression of the oncogenic $Hras^{G12V}$ mutant in the distal murine tubular system by *Cadherin 16* promoter-driven Cre expression.

This chapter describes the biological and histopathological characterisation of this model.

3.2 Results

3.2.1 Experimental setting

Mice carrying *Sdhb*^{fl} or/and *Hras*^{LSLG12V} alleles were crossed to *KspCre*$^{+}$ mice. In addition, a reporter of Cre activity was introduced into the cohort. Some *KspCre*$^{-}$ animals were observed for up to one year to exclude phenotypic effects of the mere presence of the transgenes (not shown) and were found to stay healthy without kidney pathologies. We could not detect an obvious shift in Mendelian ratios as an indication of embryonic or fetal lethality caused by the presence of *Sdhb*^{fl}, *Hras*^{LSLG12V} or *Rfp*^{LSL} alleles in *KspCre*$^{+}$ mice. *KspCre*$^{+}$, *Sdhb*$^{fl/fl}$ mice of both sexes were found to be sterile irrespective of *Hras* status. As expression of *KspCre* has been detected in the developing genitourinary tract (89), the above observation argues for an important role of intact SDH function in urogenital organ development.

At least ten *KspCre*$^{+}$ mice were followed up for clinical events for the nine different combinations of *Sdhb*^{fl} and *Hras*^{LSLG12V} alleles (Table 10) aiming for a balanced female:male ratio.

***KspCre*$^{+}$ Genotype**	***Hras*$^{wt/wt}$**	***Hras*$^{wt/LSLG12V}$**	***Hras*$^{LSLG12V/LSLG12V}$**
***Sdhb*$^{wt/wt}$**	*Sdhb*$^{wt/wt}$, *Hras*$^{wt/wt}$	*Sdhb*$^{wt/wt}$, *Hras*$^{wt/LSLG12V}$	*Sdhb*$^{wt/wt}$, *Hras*$^{LSLGV12/LSLG12V}$
***Sdhb*$^{wt/fl}$**	*Sdhb*$^{wt/fl}$, *Hras*$^{wt/wt}$	*Sdhb*$^{wt/fl}$, *Hras*$^{wt/LSL\ G12V}$	*Sdhb*$^{wt/fl}$, *Hras*$^{LSLGV12/LSLG12V}$
***Sdhb*$^{fl/fl}$**	*Sdhb*$^{fl/fl}$, *Hras*$^{wt/wt}$	*Sdhb*$^{fl/fl}$, *Hras*$^{wt/LSLG12V}$	*Sdhb*$^{fl/fl}$, *Hras*$^{LSLGV12/LSLG12V}$

Table 10: *KspCre*$^{+}$ genotypes of mice carrying *Sdhb*^{fl} and/or *Hras*^{LSLG12V} alleles.

Kidney morphologies were non-invasively monitored by ultrasound on a monthly basis until an age of at least eight months or to a clinical endpoint. Similarly, serial urine specimens were collected from the earliest age possible. Mice without clinical evidence of limiting kidney pathology were censored after a final sonographic examination at the age of one year. To dynamically characterise renal pathology and for metabolic studies (see chapter 4), at least five animals per genotype were sacrificed at a "young", "medium" and "old" age (5.5-11 weeks, 17-26 weeks, >30 weeks). These age groups were chosen to approximately correspond to typical survival times of the three different *Sdhb*$^{fl/fl}$ cohorts. A comprehensive set of tissue blocks derived from this model was analysed for

histopathological alterations at the Institute of Pathology, Universitätsklinikum Erlangen, Erlangen, Germany and selected blocks were used for immunohistochemical studies at the CRUK Beatson Institute.

3.2.2 *Hras^{LSLG12V}* accelerates fatal cystic degeneration of *KspCre^{+}, Sdhb$^{fl/fl}$* kidneys

3.2.2.1 Summary of ultrasound findings in *KspCre^{+}* kidneys

In monthly ultrasound examinations of at least 10 *KspCre^{+}* animals per genotype as outlined in Table 10, a progressive cystic transformation of *Sdhb$^{fl/fl}$* kidneys was observed. As some SDHB-proficient *Hras$^{LSLG12V/LSLG12V}$* showed individual cysts, a scoring system was defined to best recapitulate all different morphological observations (Table 11). A representative ultrasound image for each score value is depicted in Figure 4 and scores for examinations of individual mice in Figure 5.

Score value	Kidney parenchyma	Number and size of cysts, kidney pelvis structure
0	healthy	no cysts, no pelvis abnormalities
1	healthy	up to 2 cysts of small or medium size or/and dilated pelvis
2	healthy	up to 2 big cysts and up to 2 smaller cysts or up to 4 medium size cysts
3	slightly altered	More individual cysts than in score 2
4	significantly altered, beginning cystic transformation	multiple, generalised cysts in both kidneys
5	cystic transformation, but areas of parenchyma detectable	cystic transformation
6	complete cystic transformation, no intact parenchyma	cystic transformation

Table 11: Classification of sonographic kidney morphologies. Cyst numbers given for score values 1 and 2 correspond to the sum of all cysts detected in both kidneys.

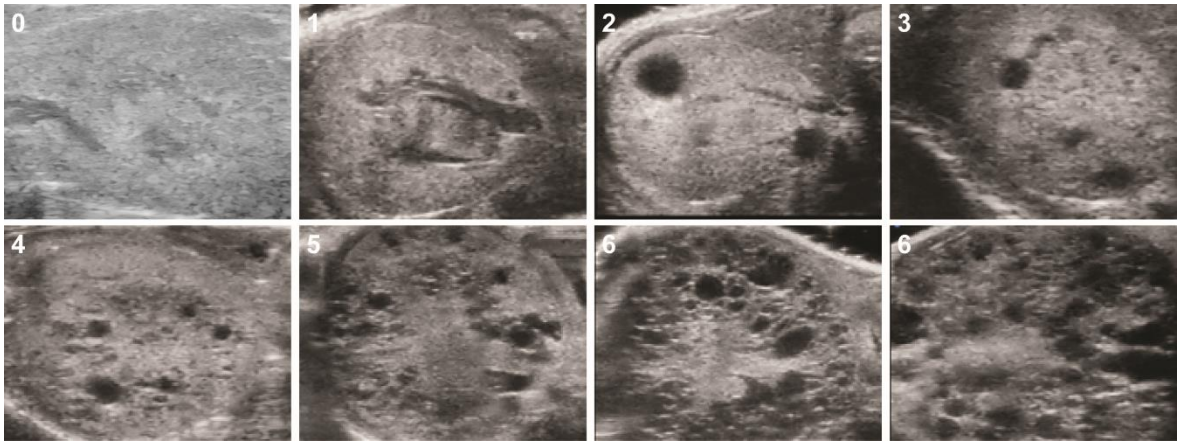

Figure 4: Exemplary images of renal morphologies corresponding to different ultrasound score values. Of note, due to the significant size increase of *KspCre*$^{+}$, *Sdhb*$^{fl/fl}$ kidneys over time, images acquired close to clinical endpoints (*i.e.* with high score values) can in many cases not capture whole kidneys. Two images are depicted for score value 6 in order to illustrate biological variance of end stage conditions.

In the *KspCre*$^{+}$, *Hras*$^{wt/wt}$ background, *Sdhb*$^{wt/wt}$ and *Sdhb*$^{wt/fl}$ kidneys did not display any significant morphological changes except for few (potentially age-related) cysts in a single *Sdhb*$^{wt/fl}$ case. In contrast, scores for *Sdhb*$^{fl/fl}$, *Hras*$^{wt/wt}$ animals increased over time to values corresponding to an (almost) entirely cystic kidney degradation (Figure 5A) close to clinical endpoints. A similar picture was observed in *KspCre*$^{+}$, *Hras*$^{wt/LSLG12V}$ cohorts with low level changes in more SDHB-proficient kidneys and much higher dynamics of score progression in *Sdhb*$^{fl/fl}$ animals (Figure 5B).

In line with their short overall survival (as will be discussed in section 3.2.2.2), most *KspCre*$^{+}$, *Sdhb*$^{fl/fl}$, *Hras*$^{LSLG12V/LSLG12V}$ mice could only be examined once and showed morphological changes corresponding to high score values at young age. An end stage score value of 6 was recorded for fewer *Sdhb*$^{fl/fl}$ mice in the *Hras*$^{LSLG12V/LSLG12V}$ than in the *Hras*$^{wt/wt}$ or *Hras*$^{wt/LSLG12V}$ setting as animals close to clinical endpoints were not subjected to the ultrasound procedure (including anaesthesia) for animal welfare reasons. It is important to notice that, albeit individual cysts were detectable in many SDHB-proficient *Hras*$^{LSLG12V/LSLG12V}$ mice, medium score values for SDHB-proficient *Hras*$^{LSLG12V/LSLG12V}$ animals remained stable (*i.e.* in contrast to scores for *Sdhb*$^{fl/fl}$ not progressive) over the (long) time scale of one year (Figure 5C).

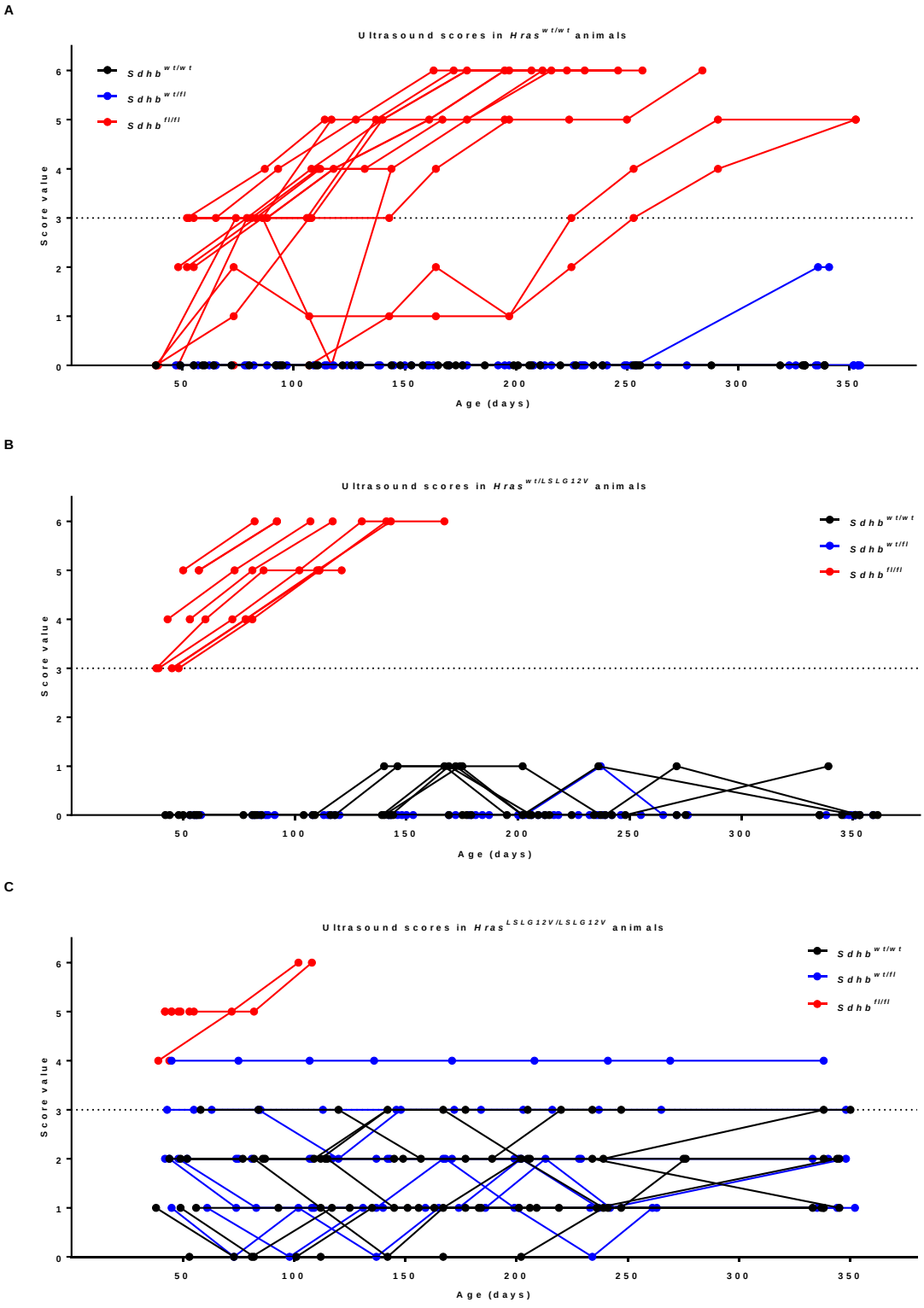

Figure 5: Sonographic score values in individual *KspCre*$^{+}$ mice over time. (A) Depicts *Hras*$^{wt/wt}$ (B) *Hras*$^{wt/LSLG12V}$ and (C) *Hras*$^{LSLG12V/LSLG12V}$ cohorts. A dotted line has been inserted at y=3 as this score value corresponds to the detectability threshold of generalised alterations of renal parenchyma.

3.2.2.2 Survival of *KspCre*$^{+}$ cohorts

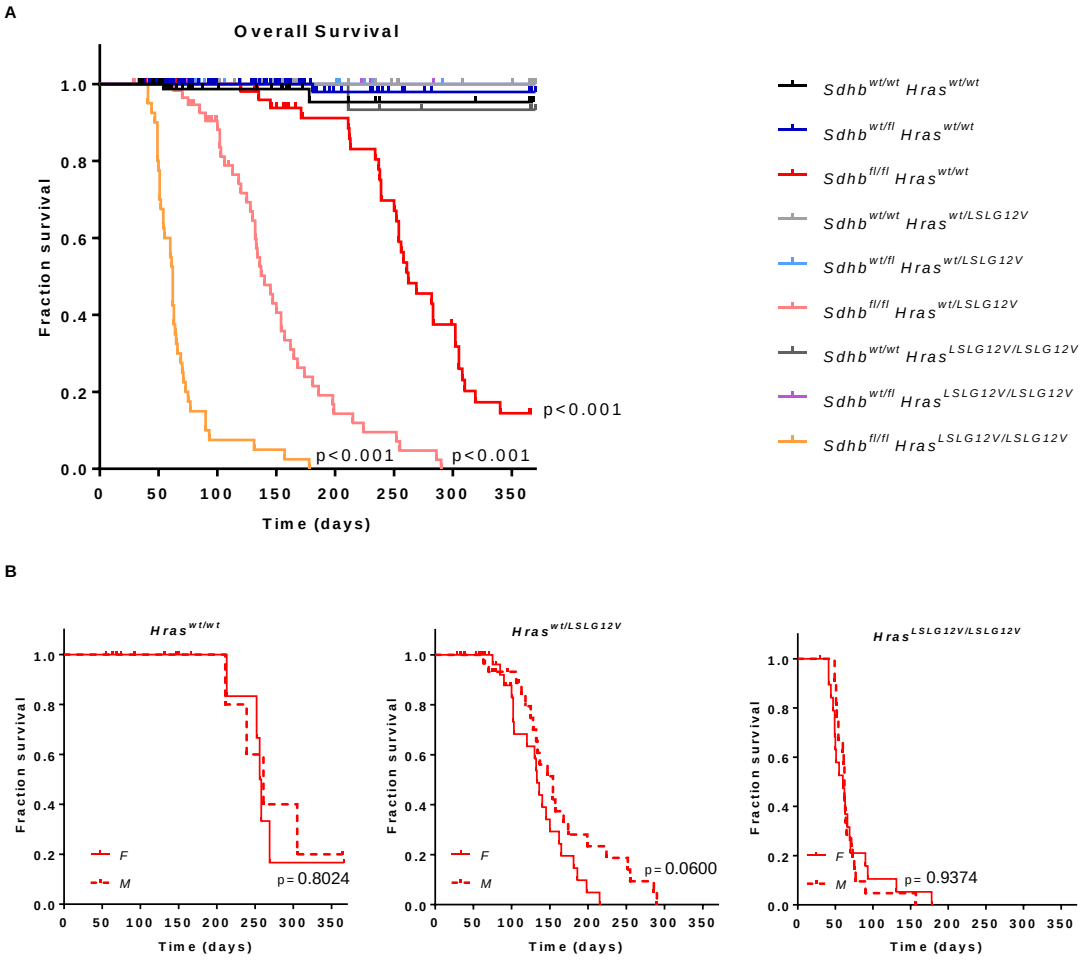

Figure 6: Kaplan-Meier curves of *KspCre*$^{+}$ cohorts. Fraction survival corresponds to mice without a model-specific clinical endpoint. (A) Survival of all genotypes. (B) Survival of female versus male *Sdhb*$^{fl/fl}$ mice matched for *Hras* genotype.

Survival data for *KspCre*$^{+}$ mice stratified for *Sdhb* and *Hras* status are summarised in Figure 6A and Table 12. The vast majority of SDHB-proficient mice did not show any clinical signs irrespective of *Hras* genotype until the end of observation time at one year of age. Most *Sdhb*$^{fl/fl}$, *Hras*$^{wt/wt}$ mice reached clinical endpoints such as hunched appearance and significantly reduced activity due to abdominal distension that was caused by the massive expansion of their kidneys (please refer to section 3.2.2.3). Median survival times of *Sdhb*$^{fl/fl}$ animals were significantly reduced by the additional presence of *Hras*^{LSLG12V} in an allele dose-dependent manner with median survival times decreasing from 262 days to 140 days and 62 days (Table 12).

Of note, albeit the very few clinical events in *Sdhb*$^{wt/wt}$ *and Sdhb*$^{wt/fl}$ animals that could not clearly be classified as non-procedural were entirely restricted to male animals (Figure 6A), median survival times were slightly higher in male than female *Sdhb*$^{fl/fl}$ cohorts (Table 12). This trend, that could potentially be explained by slightly lower fractions of cells undergoing Cre-mediated *Sdhb* deletion in male (developing) kidneys, was most pronounced in *Sdhb*$^{fl/fl}$, *Hras*$^{wt/LSLG12V}$ mice. However, despite the relatively high number of animals studied, differences in survival did not reach statistical significance for any of the comparisons (Figure 6B). As illustrated in

Table 12, presence of an *Rfp*^{LSL} allele did not exert consistent influences on survival of *Sdhb*$^{fl/fl}$ cohorts. Therefore, female and male as well as *Rfp*$^{wt/LSL}$ and *Rfp*$^{wt/wt}$ mice were grouped together in subsequent analyses.

Genotype	all mice	female	male	*Rfp*$^{wt/LSL}$	*Rfp*$^{wt/wt}$
Sdhb$^{wt/wt}$ *Hras*$^{wt/wt}$	Undefined	Undefined	Undefined	Undefined	Undefined
Sdhb$^{wt/fl}$ *Hras*$^{wt/wt}$	Undefined	Undefined	Undefined	Undefined	Undefined
Sdhb$^{fl/fl}$ *Hras*$^{wt/wt}$	262	256	283	282	258
Sdhb$^{wt/wt}$ *Hras*$^{wt/LSLG12V}$	Undefined	Undefined	Undefined	Undefined	Undefined
Sdhb$^{wt/fl}$ *Hras*$^{wt/LSLG12V}$	Undefined	Undefined	Undefined	Undefined	Undefined
Sdhb$^{fl/fl}$ *Hras*$^{wt/LSLG12V}$	140	133	154	137	145
Sdhb$^{wt/wt}$ *Hras*$^{LSLG12V/LSLG12V}$	Undefined	Undefined	Undefined	Undefined	Undefined
Sdhb$^{wt/fl}$ *Hras*$^{LSLG12V/LSLG12V}$	Undefined	Undefined	Undefined	Undefined	Undefined
Sdhb$^{fl/fl}$ *Hras*$^{LSLG12V/LSLG12V}$	62	60	62	62	62

Table 12: Median survival times of *KspCre*$^{+}$, *Sdhb*^{fl}, *Hras*^{LSLG12V} cohorts stratified for sex or *Rfp* status in addition.

3.2.2.3 Body weights and relative kidney weights of *KspCre*$^{+}$ cohorts

Besides expected higher weights of male than female mice at all ages and for all genotypes, *Sdhb*$^{fl/fl}$ animals showed significantly reduced body weights in comparison to age- and sex-matched SDHB-proficient mice at all time points studied, whereas weights of *Sdhb*$^{wt/fl}$ did not differ from *Sdhb*$^{wt/wt}$ mice at any age (Figure 7). Starting from comparable weights at young age, especially female *Hras*^{LSLG12V} allele-carrying mice showed a tendency towards lower weight gain than *Hras*$^{wt/wt}$ mice until high age (Figure 7). Taken together, these observations suggest that comparisons of renal weights and morphologies can best be performed at “young” age as SDHB-proficient cohorts show highest degree of

concordance at this time point. In order to merge kidney weight data derived from female and male mice and considering similar endpoint times for *Sdhb*$^{fl/fl}$ animals of both sexes, kidney masses were expressed relative to the body weight of the individual mice at the time of sampling.

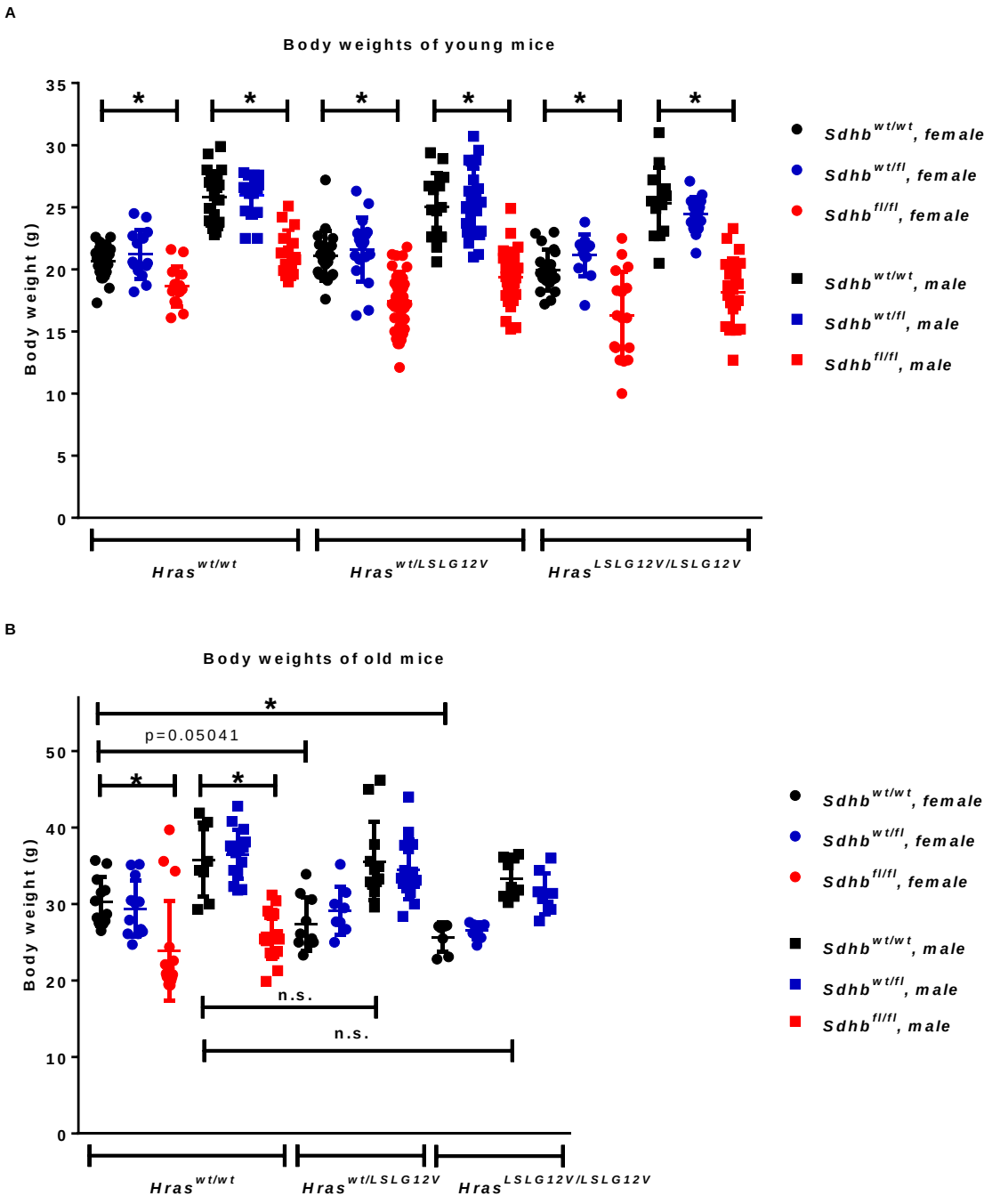

Figure 7: Body weights of young (A) and old (B) *KspCre*$^{+}$ mice for *Hras*$^{wt/wt}$ (left), *Hras*$^{wt/LSLG12V}$ (middle), and *Hras*$^{LSLG12V/LSLG12V}$ (right) cohorts. Of note, due to typical endpoint latencies of *Sdhb*$^{fl/fl}$ mice depending on *Hras* status, animal numbers are low in some of the groups. Weight differences between sex-matched *Sdhb*$^{wt/wt}$ and *Sdhb*$^{fl/fl}$ mice are significant in all comparisons for female (circles) and male (squares) animals ($p<0.05$, not indicated). Importantly, weights between *Sdhb*$^{wt/wt}$ groups of the same sex are not

significantly different at young age, but differ significantly for female mice at old age. "*", $p<0.05$.

Relative kidney weights of *Sdhb*$^{fl/fl}$ mice were significantly higher at young age in the presence of one or two *Hras*^{LSLG12V} alleles (Figure 8A). Whereas in SDHB-proficient cohorts, additional relative kidney weight fractions attributable to *Hras*^{LSLG12V} were only very modest in all comparisons with a maximum of 0.25 % for old *Sdhb*$^{wt/wt}$, *Hras*$^{LSLG12V/LSLG12V}$ *versus Sdhb*$^{wt/wt}$, *Hras*$^{wt/wt}$ mice (Figure 8C,D), at clinical endpoints, relative weights were almost doubled in *Sdhb*$^{fl/fl}$, *Hras*$^{LSLG12V/LSLG12V}$ *versus Sdhb*$^{fl/fl}$, *Hras*$^{wt/wt}$ kidneys on average (23.33% versus 12.46% of body weight). Of note, when stratified for sex, absolute kidney weights (not shown) of *Sdhb*$^{fl/fl}$ animals showed exactly the same statistically significant differences as discussed here for relative kidney weights.

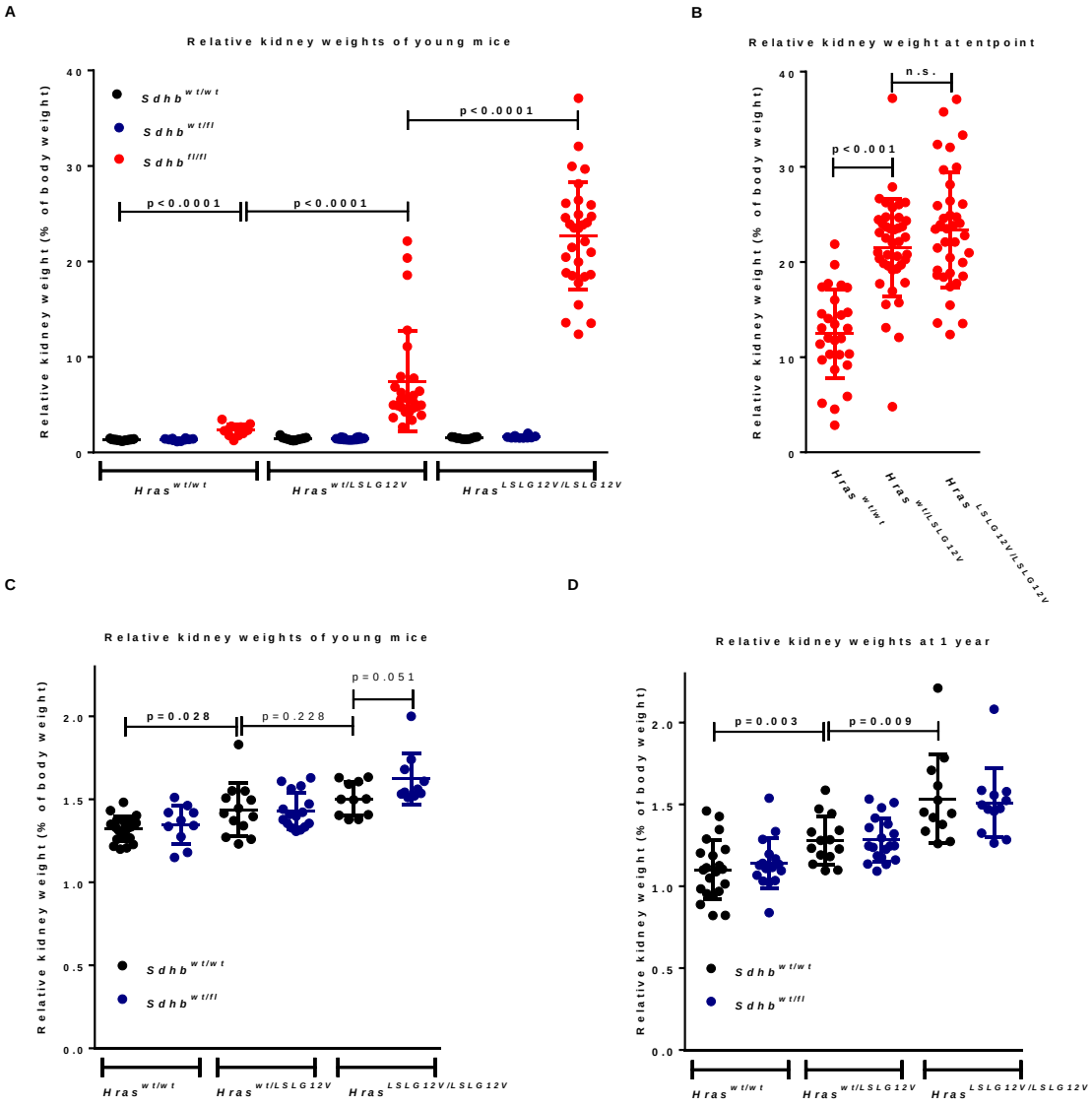

Figure 8: Kidney weights depicted relative to individual body weights (in %) for *KspCre*$^{+}$ mice of the indicated genotypes at young age (A and C), for *Sdhb*$^{fl/fl}$ cohorts at clinical clinical endpoint (B) and for SDHB-proficient mice at one year of age (D).

To gain insights into dynamics of kidney alterations in *KspCre*$^{+}$, *Sdhb*$^{fl/fl}$ mice, relative kidney weights of all mice sampled for the three cohorts were plotted against individual sampling ages. As shown in Figure 9, slope of the corresponding linear regression curves increased in a *Hras*^{LSLG12V} allele dose-dependent extent.

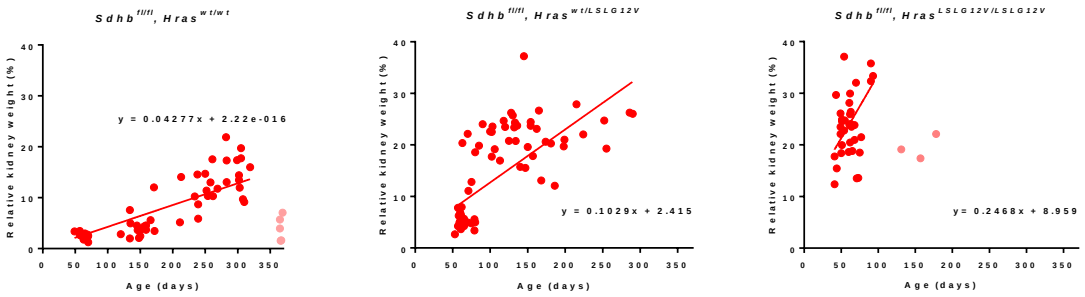

Figure 9: Linear regression (robust fit) of age-dependent relative kidney weights (normalised for individual body weights) in *KspCre*$^{+}$, *Sdhb*$^{fl/fl}$ cohorts stratified for *Hras* status. Of note, *Hras*^{LSLG12V} increases slope values of the regression functions in an allele dose-dependent manner. Obvious outliers, that have been excluded from the analyses, are marked in pink; y(0)>0 was imposed as the only constrain.

3.2.3 A dynamic histopathological description of *KspCre*$^{+}$, *Sdhb*$^{fl/fl}$, *Hras*^{LSLG12V} kidneys

3.2.3.1 Morphological comparison of *KspCre*$^{+}$ genotypes

A comprehensive set of paraffin-embedded kidney tissue blocks derived from all genotypes at the three pre-defined ages was independently analysed by a qualified pathologist at the Institute of Pathology of the Universitätsklinikum Erlangen, a reference institution for evaluation of (human) renal tumours. Figure 10 illustrates the histological appearances of typical cases at young age for all genotypes as well as for *Sdhb*$^{fl/fl}$ cohorts at clinical endpoints at low magnification after Periodic Acid Schiff (PAS) staining, a routine procedure for kidney studies that allows the discrimination between proximal and distal tubular compartments of the nephron. To determine the cellular origin of cysts in 20 distal and proximal tubule diameters per kidney were measured and are presented as averaged values for four different cases per genotype and age group in Figure 11 (A,B). These data clearly establishd the distal part of the nephron, the compartment with highest Cre expression in our model (89), as the origin of cystic alterations in *KspCre*$^{+}$, *Sdhb*$^{fl/fl}$ kidneys. In line with virtually identical diameters, proximal tubules were judged as normal across all genotypes.

Glomerulum generations, *i.e.* the maximum number of glomeruli that can be found on a representative kidney section in one diameter from the outer renal cortex to the inner medulla, can serve as a surrogate marker of a physiological kidney architecture and developmental stage (personal communication with Dr.

Markus Eckstein, Institute of Pathologie, Universitätsklinikum Erlangen). This ordinal parameter remained unchanged to the age-matched wildtype controls in SDHB-proficient kidneys irrespective of Hras status (values 6-4), but showed reduced values in *Sdhb*$^{fl/fl}$ kidneys of similar age that were most pronounced in *Hras*$^{wt/LSLG12V}$ cases (values of 1-2, Figure 11C). These changes could be indicative of a more pronounced expansion of Cre-recombined *Sdhb*$^{fl/fl}$, *Hras*^{LSLG12V} compartments.

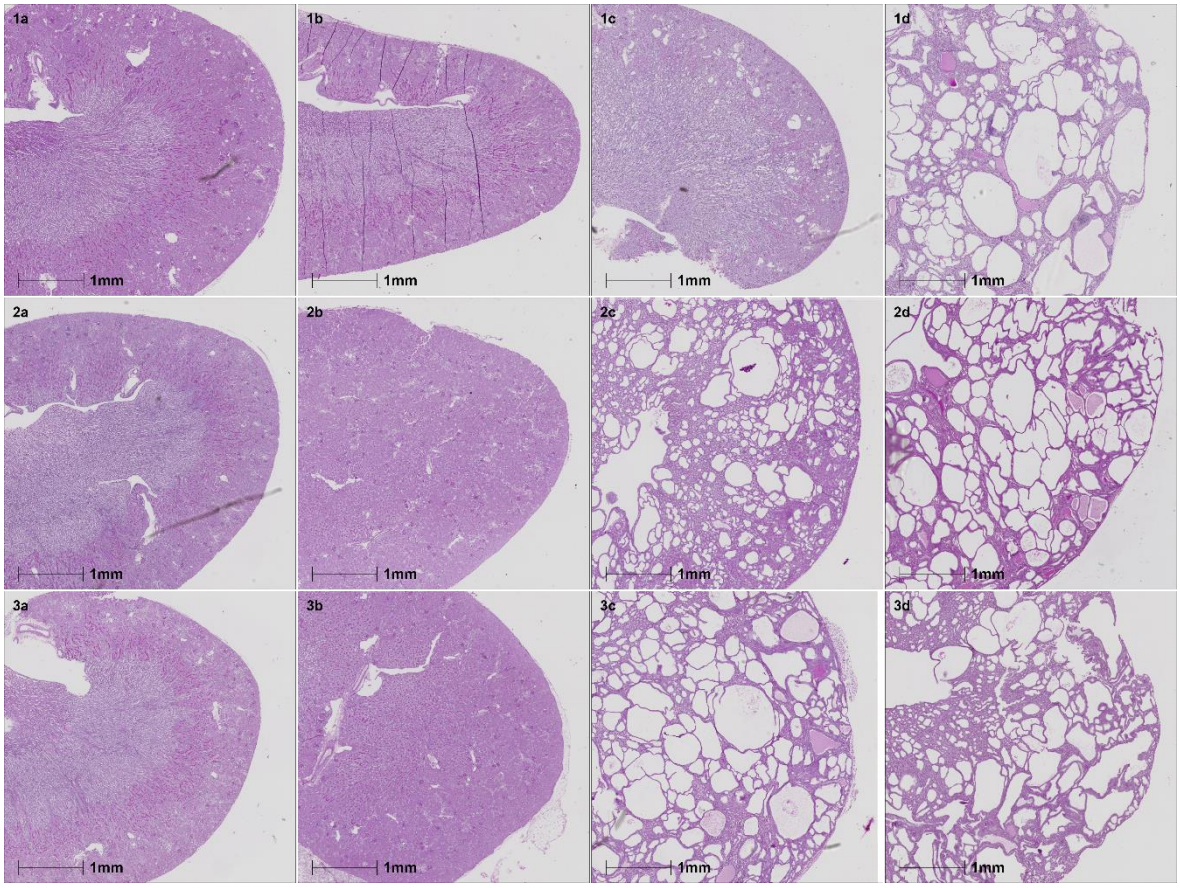

Figure 10: Exemplary overview micrographs (PAS staining) of *KspCre*$^{+}$ kidneys at young age (a-c) and at clinical endpoints (d) for *Hras*$^{wt/wt}$ (1), *Hras*$^{wt/LSLG12V}$ (2) and *Hras*$^{LSLG12V/LSLG12V}$ (3) genotypes. (a), *Sdhb*$^{wt/wt}$; (b) *Sdhb*$^{wt/fl}$, (c, d) *Sdhb*$^{fl/fl}$. Images 3c and 3d depict two different young *Sdhb*$^{fl/fl}$, *Hras*$^{LSLG12V/LSLG12V}$ cases at clinical endpoint. Please note the preserved parenchymal architecture in SDHB-proficient *Hras*$^{LSLG12V/LSLG12V}$ kidneys despite sonographic detection of individual cysts in some of the corresponding animals.

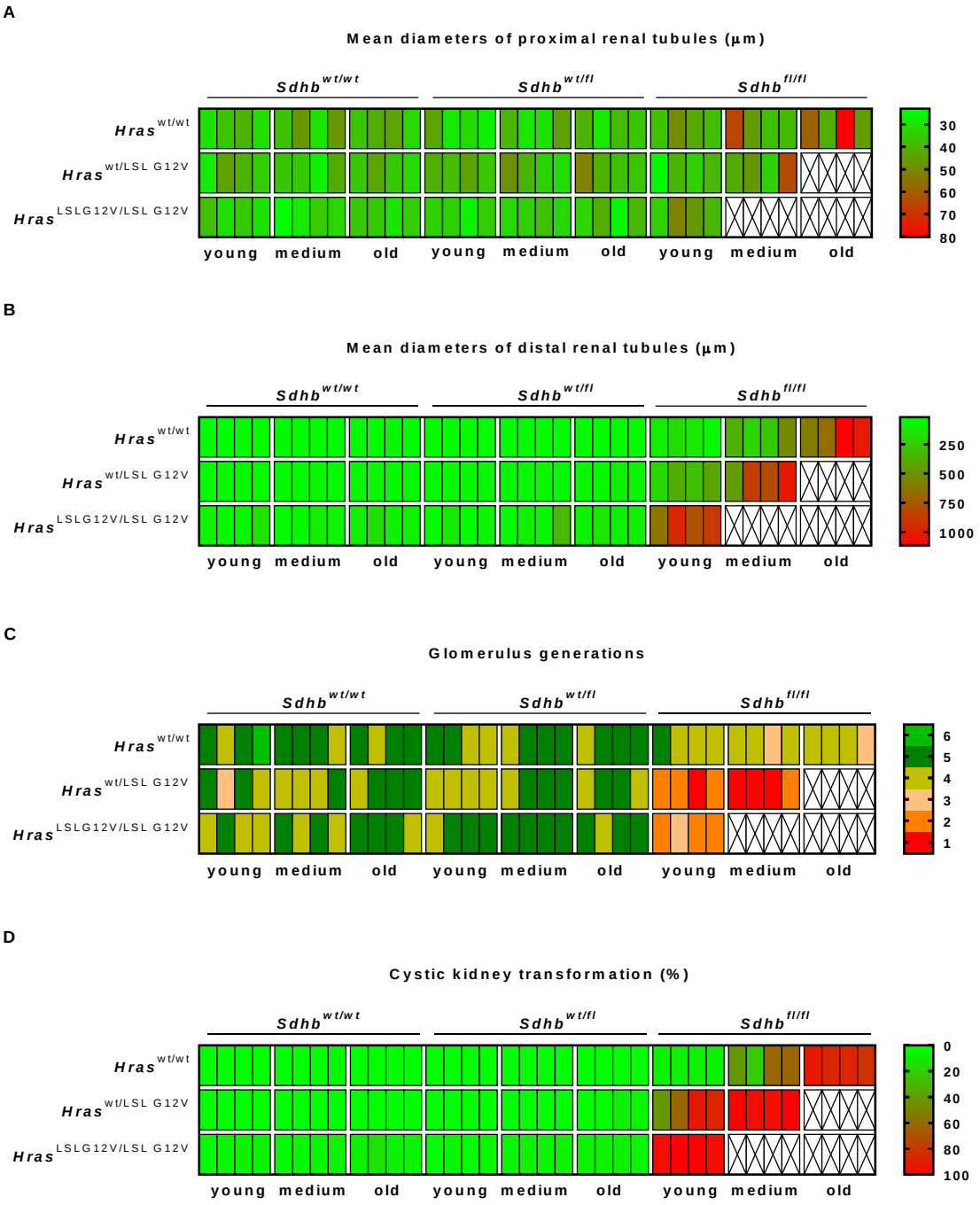

Figure 11: Summary of histopathological findings in *KspCre* mouse cohorts at different ages. Mean proximal **(A)** and distal **(B)** tubulus diameter, the ordinal number of glomerulus generations **(C)** and the degree of cystic transformation **(D)** are depicted for n=4 individual mice per age group and genotype. Of note, for *Sdhb*$^{fl/fl}$ genotypes carrying one/two *Hras*^{LSLG12V} alleles, only young and medium aged/only young kidneys were analysed due to typical endpoint latencies of these cohorts. Please not the different scales for (A) and (B).

Pathological assessment of cystic content (as % of total parenchyma) confirmed initial ultrasound observations of much earlier cystic transformations to similar end stages in *Sdhb*$^{fl/fl}$ kidneys quantitatively depending on the presence of *Hras*^{LSLG12V} alleles. In all SDHB-proficient cases analysed, cystic reorganisation did

not exceed values of 10%. Importantly, *Sdhb*$^{wt/fl}$ were virtually indistinguishable from *Sdhb*$^{wt/wt}$ kidneys by conventional histology when matched for age and genetic *Hras* status.

In addition to quantitatively assessed parameters, distal but not proximal tubules of young *Sdhb*$^{fl/fl}$, *Hras*$^{wt/wt}$ kidneys had prominent nucleoli and a few cysts in kidneys of the same genotype studied at old age showed an activated, "Hobnail cell-like" epithelium with nuclear atypia as well as focal agglomeration of multiple cell layers. As Figure 12 illustrates, these morphological pre-malignant changes were more pronounced and more frequent in *KspCre*$^{+}$, *Sdhb*$^{fl/fl}$ kidneys expressing *Hras*^{G12V}.

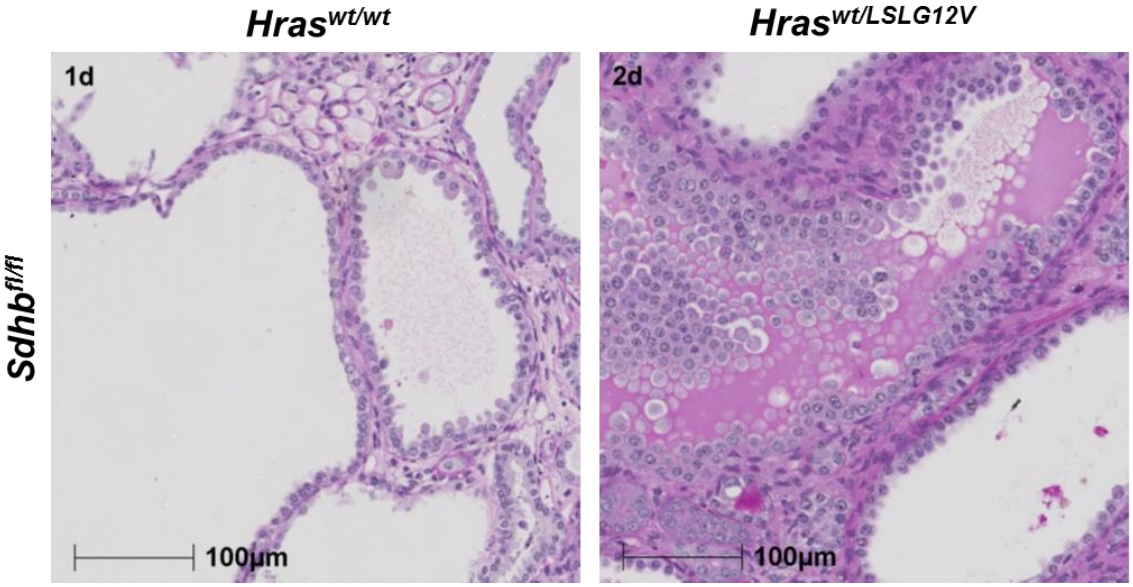

Figure 12: Exemplary ultrastructural morphologies (PAS staining) of *KspCre*$^{+}$, *Sdhb*$^{fl/fl}$, *Hras*$^{wt/wt}$ and *Hras*$^{wt/LSLG12V}$ kidneys at clinical endpoints (corresponding to panels 1d and 2d in Figure 10).

3.2.3.2 Analyses of SDHB and RFP protein expression levels

To obtain a direct evidence for the loss of SDHB protein expression due to genetic deletion of *Sdhb* exon 3 in *KspCre*$^{+}$, *Sdhb*$^{fl/fl}$ kidney cohorts, selected cases were tested for immunohistochemical SDHB reactivity under conditions that are routinely used to diagnose SDH-deficient (human) RCC. Results are illustrated in Figure 13 and scored on an ordinal scale (0-3) in Figure 14. All genotypes retained physiological levels of SDHB expression in proximal renal tubules and all *Sdhb*$^{fl/fl}$ cases selectively lacked detectable SDHB levels in distal tubular epithelium.

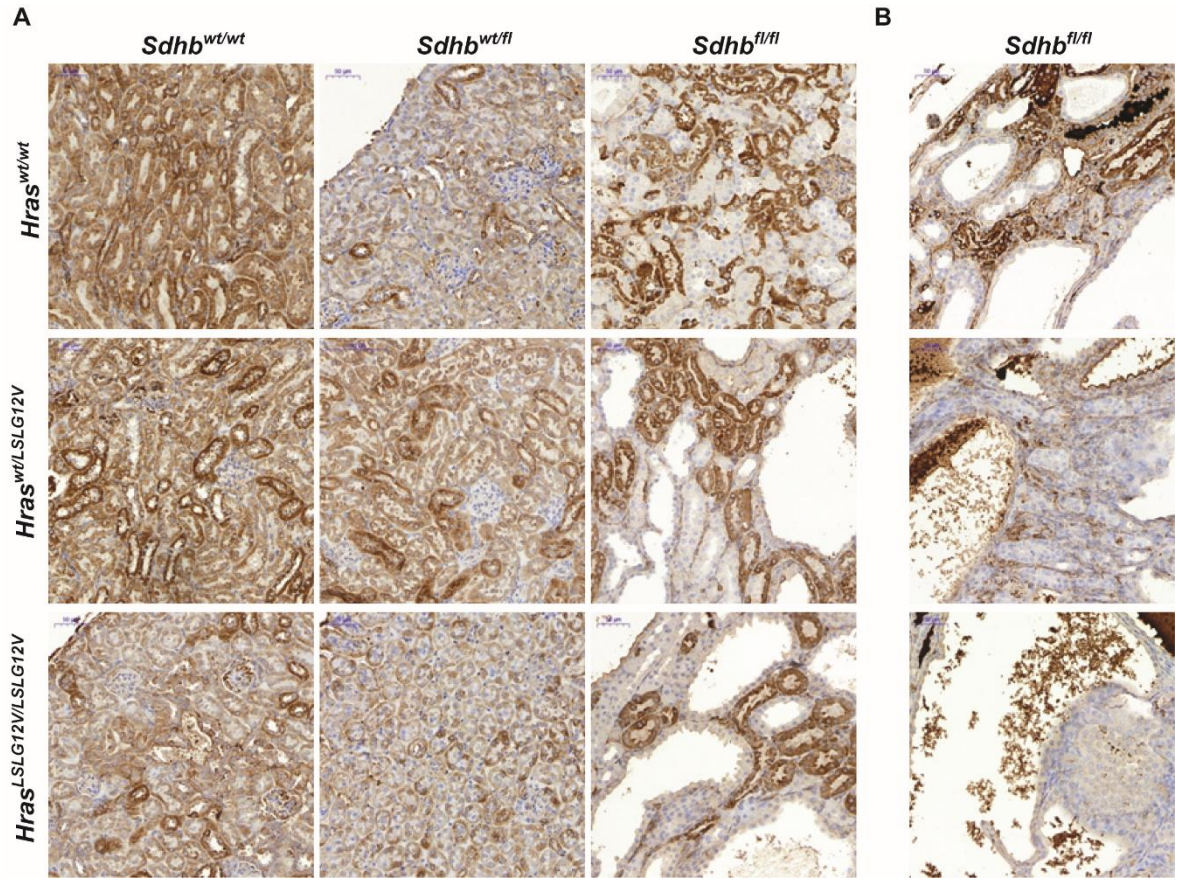

Figure 13: Representative photomicrographs of SDHB immunohistochemistry stainings of (A) *KspCre*$^{+}$ kidneys at young age and (B) *KspCre*$^{+}$, *Sdhb*$^{fl/fl}$ kidneys of the same *Hras* status as in (A) at clinical endpoints. Of note, as *KspCre Sdhb*$^{fl/fl}$ *Hras*$^{LSLG12V/LSLG12V}$ mice approached clinical endpoints at an age that corresponds to the "young" time window, two different cases are presented in A and B for this genotype. Scale bars in upper left corners correspond to 50 µm. All images were selected from photomicrographs provided by Dr. Markus Eckstein, Institute of Pathology, Universitätsklinikum Erlangen, Germany.

Despite their unremarkable morphology, *Sdhb*$^{wt/fl}$, *Hras*$^{wt/wt}$ kidneys showed preserved, but quantitatively reduced SDHB expression in distal tubules in comparison to *Sdhb*$^{wt/wt}$, *Hras*$^{wt/wt}$ cases. Similarly decreased SDHB scores resulted in distal tubules of *Sdhb*$^{wt/wt}$, *Hras*$^{wt/LSLG12V}$ and *Sdhb*$^{wt/wt}$, *Hras*$^{LSLG12V/LSLG12V}$ kidneys (Figure 14).

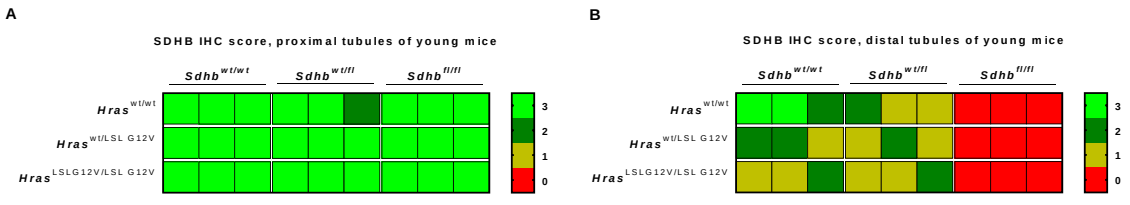

Figure 14: Ordinal SDHB immunohistochemistry scores in proximal (A) and distal (B) tubules of young *KspCre*$^{+}$ kidneys (n=3 per genotype).

Cysts in all *KspCre*$^{+}$, *Rfp*^{LSL} kidneys displayed reactivity for RFP to the same extent as the distal tubules and collecting ducts in the corresponding kidney (Figure 15), thereby providing additional evidence for an origin of cystic lesions from the Cre-recombined compartment.

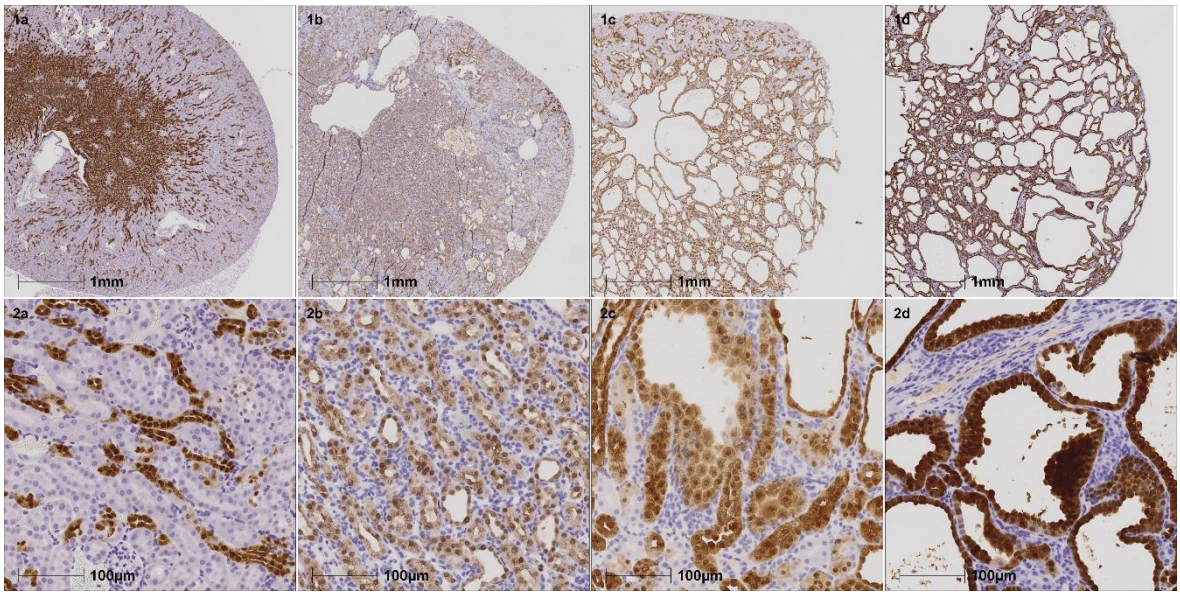

Figure 15: Exemplary RFP immunohistochemistry stainings of *KspCre*$^{+}$, *Rfp*^{LSL} kidneys at young age. Overview images are captured in panel (1), whereas panel (2) depicts images acquired at higher magnification from the same cases as in (1). Genotypes are as follows: (a) *Sdhb*$^{wt/wt}$ *Hras*$^{wt/wt}$; (b) *Sdhb*$^{fl/fl}$ *Hras*$^{wt/wt}$, (c) *Sdhb*$^{fl/fl}$ *Hras*$^{wt/LSLG12V}$, (d) *Sdhb*$^{fl/fl}$ *Hras*$^{LSLG12V/LSLG12V}$.

At young age, tissue area fractions in *Rfp*^{LSL} kidney showing cytoplasmatic reactivity for RFP were relatively higher in *Sdhb*$^{fl/fl}$, *Hras*$^{wt/LSLG12V}$ and *Sdhb*$^{fl/fl}$, *Hras*$^{LSLG12V/LSLG12V}$ samples than in the corresponding *Sdhb*$^{wt/wt}$ and *Sdhb*$^{fl/fl}$, *Hras*$^{wt/wt}$ cases. Only a trend towards increased RFP-positive tissue fractions was observed in *Sdhb*$^{wt/wt}$ groups depending on additional *Hras*$^{wt/LSLG12V}$ alleles and in *Sdhb*$^{fl/fl}$ cohorts at clinical endpoints (Figure 16).

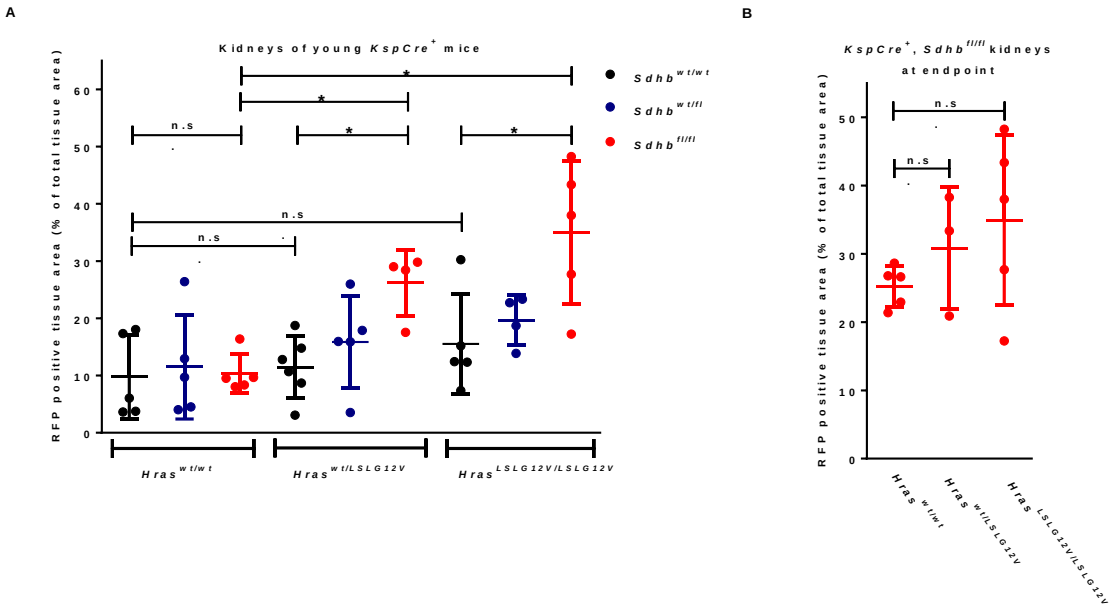

Figure 16: Quantification of RFP positive tissue areas in *KspCre*$^{+}$, *Rfp*^{LSL} kidneys that were obtained from young *Rfp*$^{LSL+}$ mice (A) or from *Rfp*$^{LSL+}$ *Sdhb*$^{fl/fl}$ mice at clinical endpoints (B)

3.2.3.3 Assessment of proliferation and DNA damage response in *KspCre*$^{+}$ kidneys

Ki-67 is a nuclear antigen that is expressed strictly associated with cellular proliferation (107). As its detection is routinely used as a marker of tumour aggressiveness in clinical pathology (107), we analysed the fraction of Ki-67-expressing cells for a selected panel of kidney tissue blocks derived from our model. Presence of *Hras*$^{wt/LSLG12V}$ alleles increased Ki-67 reactivity by a small but significant level in SDHB-proficient kidneys.

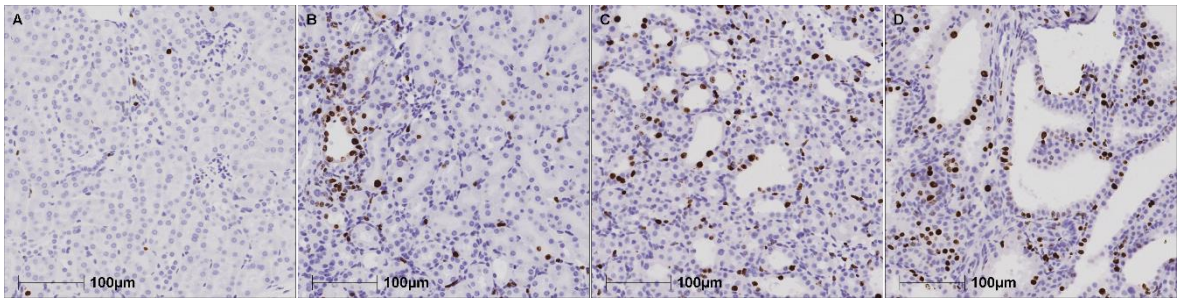

Figure 17: Illustration of Ki67 immunoreactivity in young *KspCre*$^{+}$ kidneys. (A) *Sdhb*$^{wt/wt}$, *Hras*$^{wt/wt}$; (B) *Sdhb*$^{fl/fl}$, *Hras*$^{wt/wt}$, (C) *Sdhb*$^{fl/fl}$, *Hras*$^{wt/LSLG12V}$, (D) *Sdhb*$^{fl/fl}$, *Hras*$^{LSLG12V/LSLG12V}$.

Sdhb$^{fl/fl}$ kidneys showed a quite heterogeneous staining pattern with focal areas of high Ki-67 positivity as illustrated in Figure 17 for selected cases. Nevertheless, all averages of Ki-67 positive cell ratios obtained for young *Sdhb*$^{fl/fl}$ cohorts were significantly higher than those in wildtype controls and *Hras*-matched *Sdhb*$^{wt/wt}$ samples (Figure 18A). Indicative of more pronounced cellular division, *Sdhb*$^{fl/fl}$, *Hras*$^{LSLG12V/LSLG12V}$ kidneys at clinical endpoints scored higher than *Sdhb*$^{fl/fl}$, *Hras*$^{wt/wt}$ samples (Figure 18B).

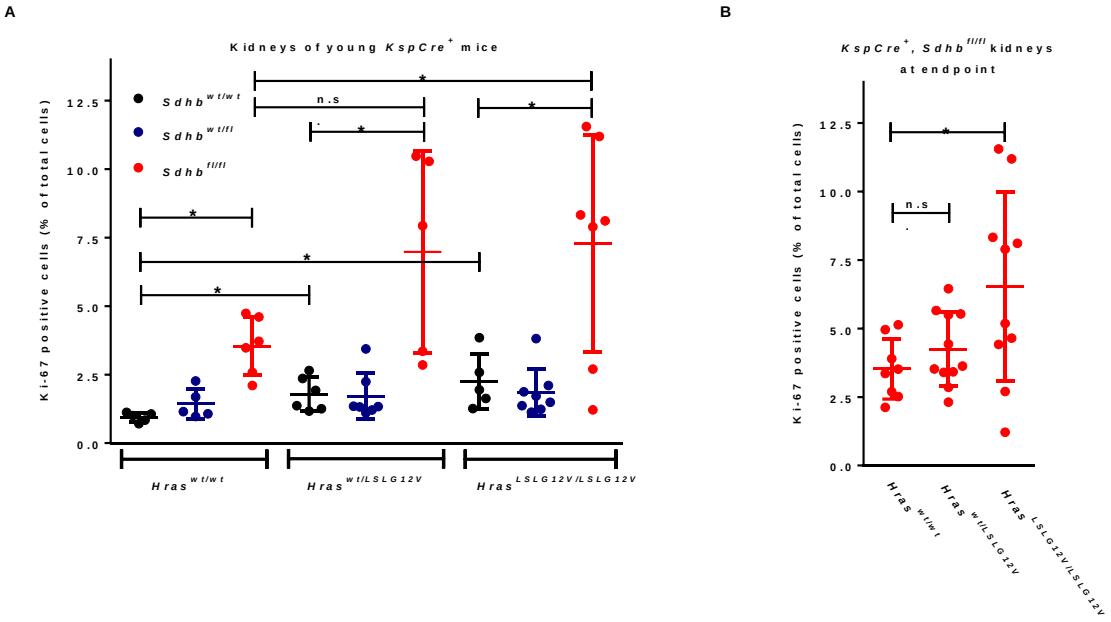

Figure 18: Analysis of Ki-67 positive cell fractions in *KspCre*$^{+}$ kidneys derived from (A) young mice or (B) from *Sdhb*$^{fl/fl}$ cohorts at clinical endpoints.

As outlined in section 1.5, it has recently been suggested that SDH-deficient tumours, similar to malignancies carrying FH or IDH1/2 mutations, possess a reduced capacity to repair DNA double strand breaks (64, 108). To validate these results in our model system, we analysed the occurrence of the Serine139-phosphorylated histone H2AX variant (γH2AX), an established early marker of the cellular response to DNA double strand breaks (109), in *KspCre*$^{+}$ kidneys (Figure 19 and Figure 20). Young SDHB-proficient cases showed similar low degrees of γH2AX reactivity irrespective of *Hras* genotype with none of the differences reaching statistical significance. In contrast, substantially higher fractions of positive cells were detected in *Sdhb*$^{fl/fl}$, *Hras*$^{wt/wt}$ kidneys with a trend (not statistically

significant in the small number of cases analysed) towards higher reactivity in kidneys carrying *Hras*^{LSLG12V} alleles in addition (Figure 20).

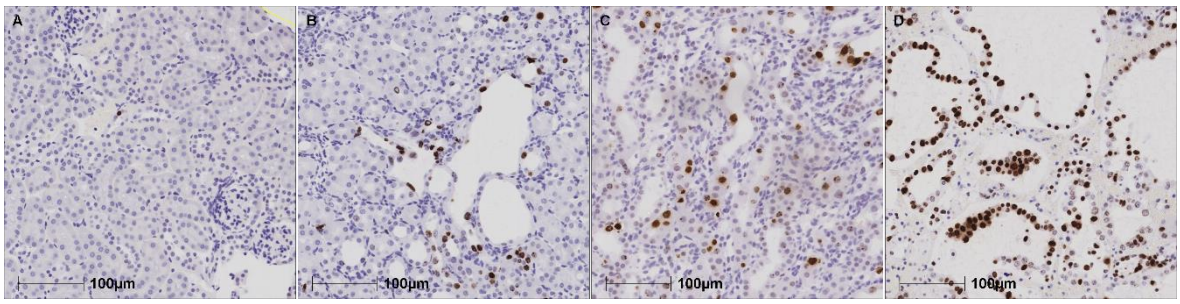

Figure 19: Illustration of γH2AX immunoreactivity in young *KspCre*$^{+}$ kidneys. (A) *Sdhb*$^{wt/wt}$, *Hras*$^{wt/wt}$; (B) *Sdhb*$^{fl/fl}$, *Hras*$^{wt/wt}$, (C) *Sdhb*$^{fl/fl}$, *Hras*$^{wt/LSLG12V}$, (D) *Sdhb*$^{fl/fl}$, *Hras*$^{LSLG12V/LSLG12V}$.

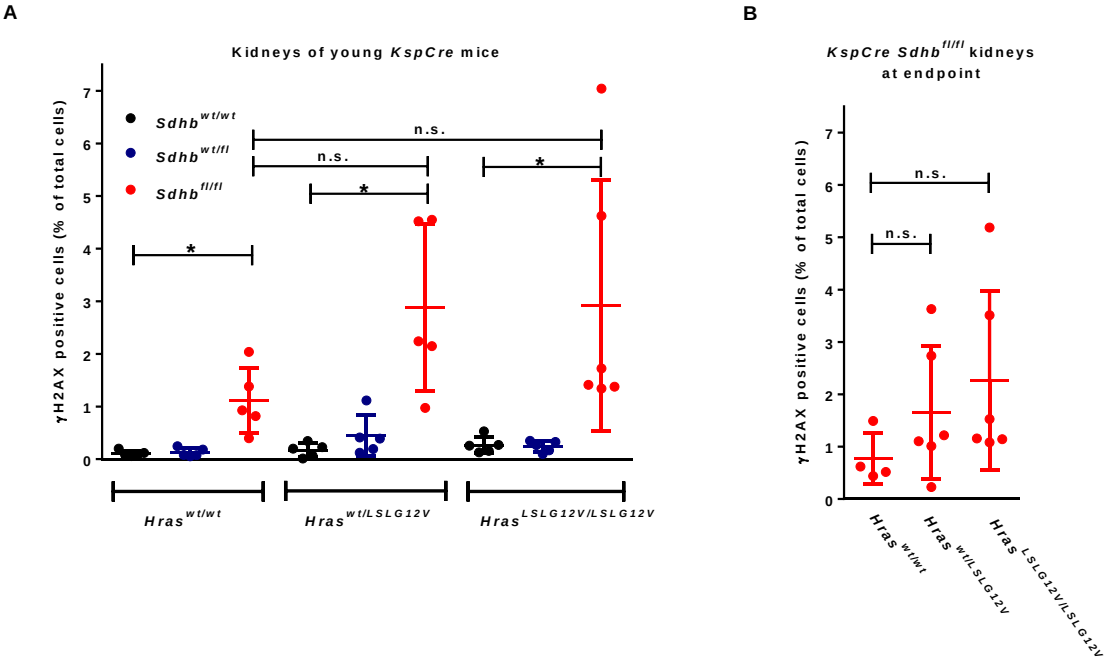

Figure 20: γH2AX reactive cell fractions stratified for *Hras* status in kidneys of (A) young *KspCre* mice and (B) KspCre Sdhb$^{fl/fl}$ mice at clinical endpoints. Differences between *Sdhb*$^{wt/wt}$ and *Sdhb*$^{wt/fl}$ groups were not statistically significant.

3.3 Discussion

Our goal of specifically targeting the suggested origin of SDH-deficient RCC, the distal renal tubular system, provided the basis for employing *KspCre*-driven recombination to conditionally delete *Sdhb* and/or activate transcription of oncogenic *Hras*^{G12V} (57). Considering several typical features of early malignancy

that we observed in our model, I believe that *KspCre*$^{+}$, *Sdhb*$^{fl/fl}$, *Hras*^{LSLG12V} mice can model important aspects of SDH-deficient renal tumourigenesis despite the lack of macroscopic tumour formation. In particular, as recently described for SDH-deficient cell lines and in xenotransplantation assays (64), our γH2AX analyses provide evidence for increased DNA damage in *KspCre*$^{+}$, *Sdhb*$^{fl/fl}$ kidneys as a potentially initiating mechanism of SDH-deficient tumourigenesis. Nevertheless, due to lack of a SDHB-proficient tumour-resembling phenotype as a control, we cannot formally exclude that higher levels of γH2AX reactivity (*i.e.* DNA damage) in *KspCre*$^{+}$, *Sdhb*$^{fl/fl}$ kidneys are merely a result of increased cellular proliferation *per se*, but not SDH deficiency in our mouse model.

As in other immunohistochemical analyses, comparisons between *Sdhb*$^{fl/fl}$ cohorts differing in *Hras*^{LSLG12V} status often resulted in trends but not always in statistically significance of changes. This argues from my point of view rather in favour of high biological or/and technical variation within than lack of differences between genotypes. Higher case numbers in future staining approaches would be an appropriate option to counteract this limitation.

It is also interesting to note that the definition of "carcinoma" in mouse models varies between researchers. The independent reference pathology institute reviewing our model chose a conservative approach in its judgement by not diagnosing microscopic lesions of multiple cell layers with several cellular abnormalities as "carcinoma", but requesting a disruption of the epithelial basal membrane (*i.e.* invasiveness) as an obligate feature of malignancy. Histomorphological features that resemble the alterations in our model system have recently been classified as "renal cell carcinomas" by other researchers (110).

The cystic phenotype that occurred in *KspCre*$^{+}$, *Sdhb*$^{fl/fl}$ kidneys is an observation that has been published for other genetic hits in *KspCre*-based models (110, 111). Even though the morphological characterisation of SDH-deficient RCC comprises a varying degree of cystic areas (58), cysts limit survival of *KspCre*$^{+}$, *Sdhb*$^{fl/fl}$, *Hras*$^{wt/LSLG12V}$ and even more of *KspCre*$^{+}$, *Sdhb*$^{fl/fl}$, *Hras*$^{LSLG12V/LSLG12V}$ mice at an age that might prevent later formation of macroscopic tumours.

While this thesis project was ongoing, Harlander and colleagues published a genetically engineered mouse model of ccRCC based on a tamoxifen-inducible variant of the *KspCre* construct, *KspCreER*^{T2}, without impairment of animal survival by generalised cyst development (112). Many features of ccRCC, could be recapitulated in this model by combined homozygous deletion of the *Rb1, Vhl* and *Tp53* genes. Given that *KspCre*-driven recombination efficacy in proximal tubules, the cellular origin of ccRCC in humans (55), is much lower than in distal tubular structures (89) (and assuming the same for *KspCreER*^{T2}), these results strongly argue for different critical genetic events in the distal compared to the proximal tubule.

The results discussed in this chapter underscore the importance of allele dose imbalances for consequences of *Hras*^{G12V} activation: in the absence of wildtype *Hras* expression and upon activation of two *Hras*^{LSLG12V} alleles (*Hras*$^{LSLG12V/LSLG12V}$), *KspCre+*, *Sdhb*$^{fl/fl}$ mice reach endpoints with a latency of less than 50% compared to mono-allelic *Hras*^{G12V} in the presence of a remaining *Hras* wildtype allele (Table 12). Cysts in SDHB-proficient kidneys became evident virtually exclusively in *Hras*$^{LSLG12V/LSLG12V}$ cohorts and could potentially be a correlate of oncogene-induced senescence triggered by strong Hras^{G12V} signalling. Together with sequential ultrasound data for individual mice, higher slopes of kidney weight regression curves over time argue for more dynamic kidney degeneration in the presence of Hras activity and against only basal *Hras*-induced kidney changes that add to a phenotype that is caused by *Sdhb* loss.

As a key point from this chapter arises the question for a mechanism of an interaction between *Hras*^{G12V} and *Sdhb* loss. In contrast to genomic and transcriptomic TCGA data demonstrating *HRAS* activation exclusively in Pho/PGL cases with mono-, but not bi-allelic SDHB deletions, our renal cell carcinoma model revealed *Hras*^{G12V}-mediated phenotypic interactions with genetic *Sdhb* inactivation in mice with homozygous *Sdhb* deletion only. If a genetic association with HRAS activation and is biologically relevant in tumourigenesis of SDH loss-related malignancies, these differences could be explained by cancer-/tissue-specific requirements: Whereas shallow *SDHB* deletions could be sufficient to induce a certain, in the context of activating *HRAS* mutations (or alternative tumour-promoting cellular events) critical degree of functional SDH deficiency in

Pheo/PGL, homozygous genetic loss of *Sdhb* might be needed in order to trigger a similar interaction in renal cell carcinoma.

Tanner and colleagues could recently demonstrate that acute RAS overexpression activates all of the four steps that control the rate of glycolytic flux (113). This RAS-mediated metabolic reprogramming could function as a mechanism to facilitate survival and proliferation of cells with defects in oxidative metabolic pathways such as in the case of *Sdhb* deletion. Another line of thought would be triggering of SUCNR1, a receptor that is highly expressed in the kidney and at least in some organs shares downstream effectors with RAS, by increased succinate concentrations in *KspCre*$^{+}$, *Sdhb*$^{fl/fl}$ tubular cells (21, 65).

3.4 Summary

This chapter described our efforts to develop the first genetically engineered mouse model of SDH-deficient RCC. The major phenotype that resulted from specific loss of SDHB expression in the distal renal tubular system of *KspCre*$^{+}$, *Sdhb*$^{fl/fl}$ mice, the compartment in which Cre-mediated recombination occurs at high efficacy in our experimental system, was a progressive cystic kidney degeneration. This pathology, that was significantly accelerated as well as more pronounced by additional activation of the oncogenic *Hras*^{G12V} mutation in the same compartment, limited survival of all *KspCre*$^{+}$, *Sdhb*$^{fl/fl}$ cohorts.

Whilst we did not observe any macroscopic tumours in our model, SDHB loss-related cysts displayed typical (immuno-)histological and cytological features of early malignancy. It is tempting to speculate that the detrimental global transformation of *KspCre*$^{+}$, *Sdhb*$^{fl/fl}$ kidneys imposes a latency of clinical endpoints that, at least in *Sdhb*$^{fl/fl}$, *Hras*$^{wt/LSLG12V}$ and *Sdhb*$^{fl/fl}$, *Hras*$^{LSLG12V/LSLG12V}$ cohorts, is too short to allow formation of macroscopic tumours in this model.

4 Metabolomic investigations in a mouse model of kidney-specific SDHB deficiency

4.1 Introduction

As discussed in chapter 3, we have generated a kidney-specific, genetically engineered *Sdhb*-deleted mouse model. Even though this model can recapitulate some, but not all features of SDH-deficient renal cell carcinoma, it allowed us to generate a substantial number of biological replicates for animals with a relevant mass of SDHB-deficient renal tissue (evidenced by direct immunohistochemistry for SDHB in section 3.2.3.2). This chapter outlines our ongoing work to identify new systemic metabolic biomarkers of SDH-deficient cancers. Even more than the other result chapters of my thesis, this section describes preliminary results of work in progress.

In order to study all genotypes of interest in screening approaches, specimens of mice at young age had to be compared. It had to be expected that the concordance of progressive renal failure with the *Sdhb*-deficient condition would introduce another layer of complexity to the work, as systemic elevation of certain metabolites (such as creatinine in human plasma), that is associated with worsening kidney function, occurs long before renal pathology becomes evident and has been used for decades as a means of clinical routine.

Since tumours usually arise in a background of normal cells that will largely define the metabolic profile of body fluids, an ideal tumour-specific biomarker would be a malignancy-associated substance that is of low abundance in blood and urine of healthy individuals and rises in concentration with tumour development/ size increase.

4.2 Results

4.2.1 Experimental setting

Eight biological replicates of kidney, urine and plasma samples derived from young (but not identical for all three experiments) *KspCre*$^{+}$ mice of all genotypes under investigation (Table 10) were extracted and subjected to the untargeted metabolomics approach described in section 2.2.6 (with the exception of *Sdhb*$^{wt/fl}$

for plasma analytics). Before data that had been acquired by mass spectrometry were processed by the CompoundDiscoverer software, they were checked by a targeted analysis for read-outs of *Sdhb* deficiency (succinate and aspartate abundancies) and renal dysfunction (creatinine).

4.2.2 Targeted analyses of creatinine, succinate and aspartate abundancies and monitoring of water intake rates

Creatinine concentrations in kidneys of *KspCre*$^{+}$, *Sdhb*$^{fl/fl}$ were significantly higher than in the corresponding wildtype conditions, if two obvious outliers were excluded for the *Sdhb*$^{fl/fl}$, *Hras*$^{LSLG12V/LSLG12V}$ condition even in a strictly allele dose-dependent fashion. As expected, *Sdhb*$^{fl/fl}$ kidneys showed massively increased succinate abundancies that were, to my surprise, very similar between the three cohorts despite the dramatic biological differences depending on *Hras* status. Conversely, *Sdhb*$^{fl/fl}$ kidneys showed decreased aspartate abundancies, and, interestingly, means of all SDHB-proficient genotypes carrying *Hras*^{LSLG12V} alleles were higher than for the *Sdhb*$^{wt/wt}$ reference group (Figure 21).

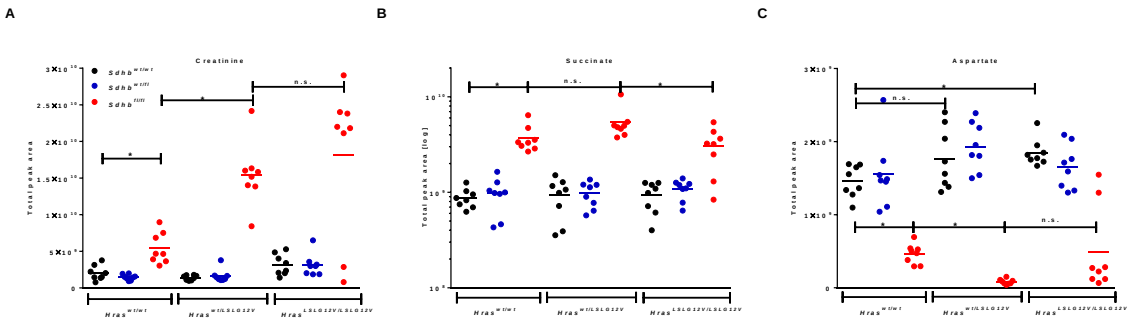

Figure 21: Creatinine (A), succinate (B) and aspartate abundancies in young *KspCre+* kidneys. Please note the logarithmic y-axis in (B)

In line with renal dysfunction and opposite to kidney tissue levels, significantly lower creatinine concentrations were detected in all *Sdhb*$^{fl/fl}$ urines irrespective of *Hras* genotype, and, much less pronounced, in SDHB-proficient *Hras*$^{LSLG12V/LSLG12V}$ mice. In line with increased consumption by *Sdhb*$^{fl/fl}$ kidney tissue, aspartate was found to be depleted in the corresponding urines as well (Figure 22).

Substantially different urinary creatinine abundancies between genotypes were highly suggestive of generally varying concentrations of urines, i.*e*. altered total urine excretion rates compared to *KspCre*$^{+}$, *Sdhb*$^{wt/wt}$, *Hras*$^{wt/wt}$ mice. Such a

biological phenomenon would be extremely important to detect in order to justify normalisation strategy for measured metabolite abundancies. As a surrogate parameter for general fluid turnover in the *KspCre*$^{+}$ model, I measured water intake (for technicalities please refer to section 2.2.1.3) in numerous individual mice of all genotypes at different ages. This approach was chosen as an easy and less stressful procedure over direct monitoring of urine volumes as the latter would have required much more labour-intensive long-term observation of numerous mice in metabolic cages. Following the reasonable assumption of a correlation between oral water intake and total urine output within a sufficiently long time interval (5 days in this experiment), together with absolute metabolite abundancies in urines, the values depicted in Figure 23 imply a higher succinate excretion rate in young *KspCre*$^{+}$, *Sdhb*$^{fl/fl}$, *Hras*$^{wt/LSLG12V}$ and *KspCre*$^{+}$, *Sdhb*$^{fl/fl}$, *Hras*$^{LSLG12V/LSLG12V}$ than in *KspCre*$^{+}$, *Sdhb*$^{fl/fl}$, *Hras*$^{wt/wt}$ animals. Furthermore, Figure 23 outlines a significant functional impact of HRAS activation on kidney function.

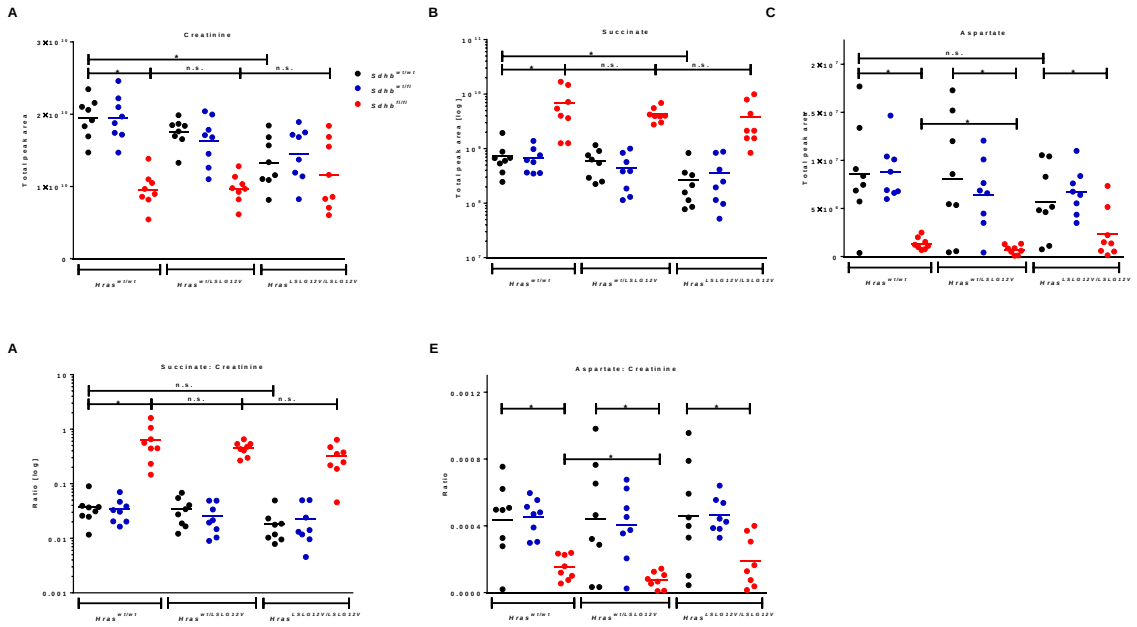

Figure 22: Creatinine (A), succinate (B) and (C) aspartate abundancies in urines of young *KspCre*+ mice as total peak areas, and normalised to individual creatinine abundancies for succinate (D) and aspartate (E).

Age-matched plasma (studied without *Sdhb*$^{wt/fl}$ cohorts) displayed only very few genotype-dependent changes in the three chosen metabolites (Figure 24). In particular, plasma succinate concentrations scattered around similar means between the cohorts. Only *KspCre*$^{+}$, *Sdhb*$^{fl/fl}$, *Hras*$^{LSLG12V/LSLG12V}$ plasma (derived

from young mice at clinical endpoints) showed significantly increased plasma creatinine concentrations in comparison to healthy controls.

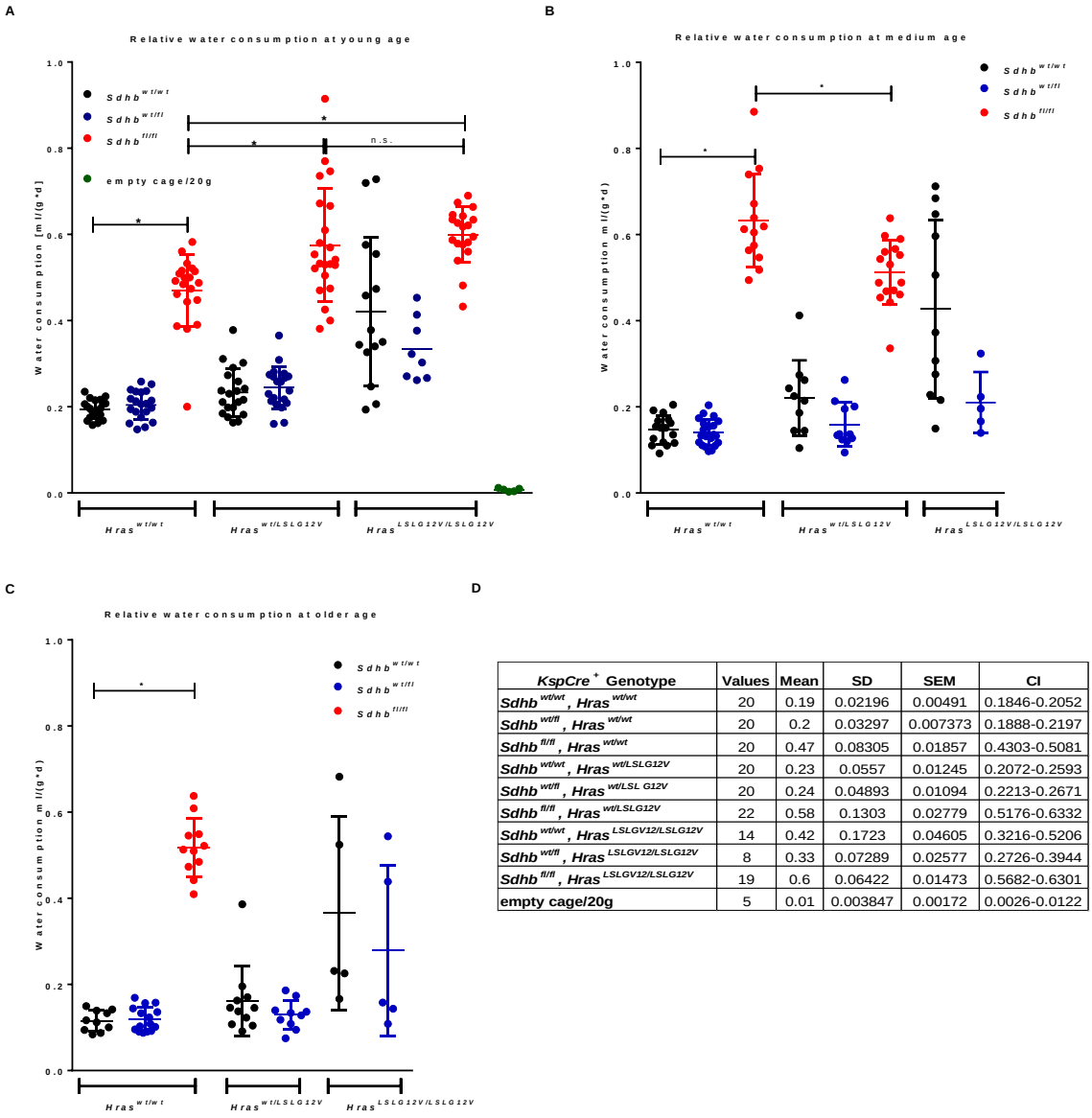

D

KspCre⁺ Genotype	Values	Mean	SD	SEM	CI
Sdhb $^{wt/wt}$, ***Hras*** $^{wt/wt}$	20	0.19	0.02196	0.00491	0.1846-0.2052
Sdhb $^{wt/fl}$, ***Hras*** $^{wt/wt}$	20	0.2	0.03297	0.007373	0.1888-0.2197
Sdhb $^{fl/fl}$, ***Hras*** $^{wt/wt}$	20	0.47	0.08305	0.01857	0.4303-0.5081
Sdhb $^{wt/wt}$, ***Hras*** $^{wt/LSLG12V}$	20	0.23	0.0557	0.01245	0.2072-0.2593
Sdhb $^{wt/fl}$, ***Hras*** $^{wt/LSL\ G12V}$	20	0.24	0.04893	0.01094	0.2213-0.2671
Sdhb $^{fl/fl}$, ***Hras*** $^{wt/LSLG12V}$	22	0.58	0.1303	0.02779	0.5176-0.6332
Sdhb $^{wt/wt}$, ***Hras*** $^{LSLGV12/LSLG12V}$	14	0.42	0.1723	0.04605	0.3216-0.5206
Sdhb $^{wt/fl}$, ***Hras*** $^{LSLGV12/LSLG12V}$	8	0.33	0.07289	0.02577	0.2726-0.3944
Sdhb $^{fl/fl}$, ***Hras*** $^{LSLGV12/LSLG12V}$	19	0.6	0.06422	0.01473	0.5682-0.6301
empty cage/20g	5	0.01	0.003847	0.00172	0.0026-0.0122

Figure 23: Relative water intake of *KspCre*⁺ cohorts at different ages. Water intake was measured at young **(A)**, medium **(B)**, and older **(C)** age and expressed as intake per day normalised to individual body weights. Numerical details for measurements in young animals are given in **(D)**.

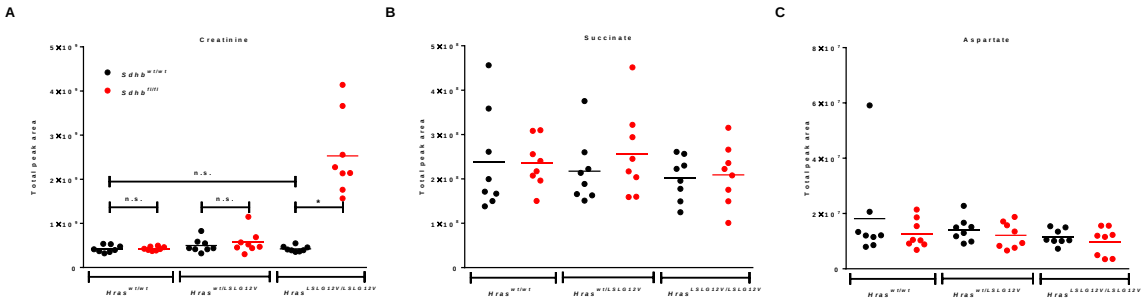

Figure 24: Creatinine (A), succinate (B) and aspartate (C) abundancies in plasma specimens of young *KspCre+* mice.

Taken together, whereas I could measure increased succinate abundancies, depleted aspartate levels and inverse creatine concentration changes in young kidneys and urines of all *KspCre*$^{+}$, *Sdhb*$^{fl/fl}$ cohorts, stable plasma samples most likely reflected the capacity of the organism to buffer pathological conditions of single organs.

4.2.3 Global evaluation of untargeted metabolomic data obtained in *KspCre*$^{+}$ plasma, kidney and urine specimens

The total number of compounds that we could detect in the three untargeted metabolomics data sets increased from plasma over kidney to reach a maximum of 6642 in urine. At the current stage of investigation, I cannot state if this observation is a result of lower run alignment quality in our urine and kidney data sets, is caused by higher extraction dilution of plasma than urine samples, or is a reflection of a true higher biological complexity. I believe that higher rates of individual compounds that pass our correction algorithm threshold (relative standard deviation of <30% between the technical QC replicates) in kidney and urine argue in favour of the latter assumption.

Data set	Total compound Number	Compounds retained after QC	Compound fraction retained after QC
Plasma	1398	813	0.58
Kidney	3518	2440	0.69
Urine	6642	5269	0.79

Table 13: Overview of compound numbers and ratios of retained compounds after QC correction in untargeted KspCre metabolomics.

For a first global overview, compound abundancies were subjected to principal component analyses first without and subsequently after correction and filtering

of individual compound abundancies using technical QC replicates. Results are presented in Figure 25, Figure 26 and Figure 27.

Plasma specimens (Figure 25) clustered together relatively independent of sex and genotype with exception of most *KspCre*$^{+}$, *Sdhb*$^{fl/fl}$, *Hras*$^{LSLG12V/LSLG12V}$ samples (that had been derived from animals of substantially impaired general condition). Applying our QC correction and filtering strategy did neither substantially improve group separation nor increase amounts of biological variance explained by the first two principal components. When analysed separately, *Sdhb*$^{wt/wt}$ genotypes were mainly separated by sex irrespective of *Hras* genotype in contrast the *Sdhb*$^{fl/fl}$ condition, where *Hras*$^{LSLG12V/LSLG12V}$ remained the major discriminator.

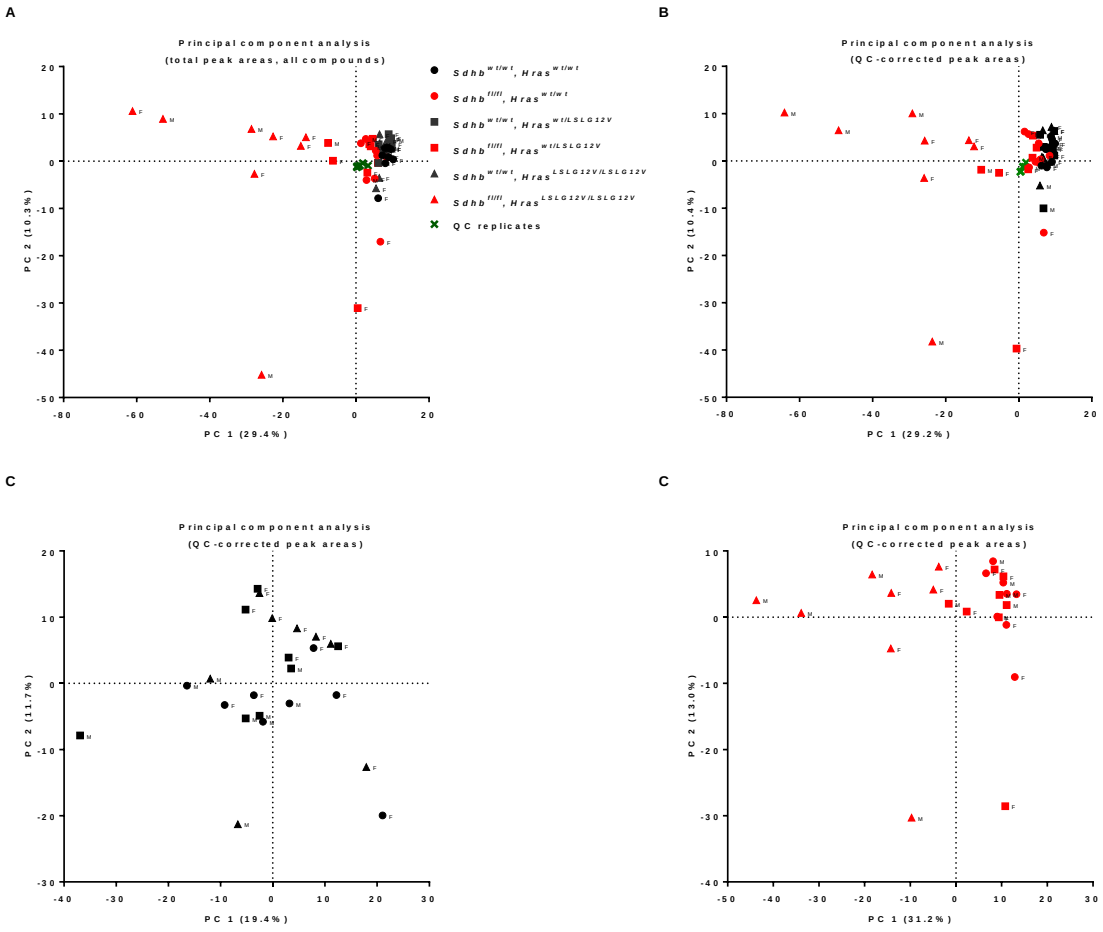

Figure 25: Principal component analyses of untargeted metabolomic data obtained from *KspCre*$^{+}$ plasma samples. Results for all genotypes and quality control (QC) replicates based on raw peak areas of all compounds detected **(A)**, after correction for technical quality control replicates **(B)**, for *Sdhb*^{wlwt} genotypes after QC correction **(C)** and for *Sdhb*$^{fl/fl}$ samples after QC correction **(D)**. Legends presented in (A) apply to all panels. F, female, M, male.

Hras^{LSLG12V}-dependent separation of the *Sdhb*$^{fl/fl}$ genotypes became more evident in the kidney data set where *Sdhb*$^{fl/fl}$ tissues were set apart from the SDHB-proficient cluster by *Hras* activation (with the exception of two *Sdhb*$^{fl/fl}$, *Hras*$^{LSLG12V/LSLG12V}$ outliers that had been identified in the previous targeted analyses). Focussing on SDHB-proficient tissues, a remarkable separation by female and male origin, but not *Sdhb*$^{wt/wt}$ *versus* *Sdhb*$^{wt/fl}$ or *Hras*$^{wt/wt}$ *versus* *Hras*^{LSLG12V} as in *Sdhb*$^{fl/fl}$ kidneys resulted. (Figure 26).

Surprising at first glance, the urine data set depicted an inverse picture with most *Sdhb*$^{fl/fl}$ (and very few SDHB-proficient) samples clustering in a small area and *Sdhb*$^{wt/wt}$ *as well as* *Sdhb*$^{wt/fl}$ specimens showing a high degree of variation (Figure 27A,B).

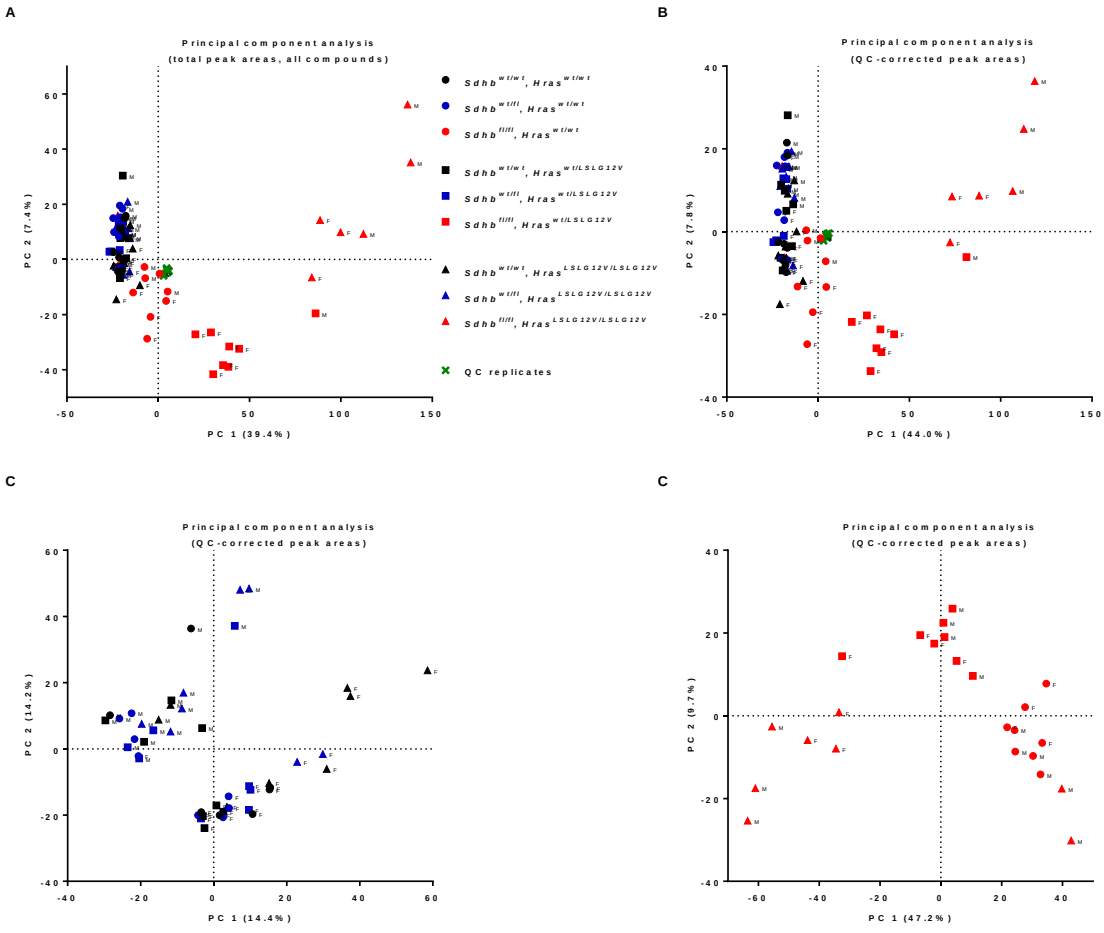

Figure 26: Principal component analyses of untargeted metabolomics data obtained from *KspCre*$^{+}$ kidneys. Results are depicted for all genotypes and technical quality control (QC) replicates based on raw peak areas of all compounds detected **(A)**, after correction for technical quality control replicates **(B)**, for SDHB-proficient genotypes after QC correction **(C)** and for *Sdhb*$^{fl/fl}$ specimens only after QC correction **(D)**. Legends presented in (A) apply to all panels. Please note changes in values for PC1 and PC2 between the panels. F, female, M, male.

Dramatically higher fluid intake rates in *Sdhb*$^{fl/fl}$ than in *Sdhb*$^{wt/wt}$ and *Sdhb*$^{wt/fl}$ mice (and inevitably resulting higher general urine metabolite dilutions, *cf*. Figure 22) as shown in Figure 23 provide the most probable explanation for these results. We thus applied an additional layer of data correction to the urine data set using a "constant sum" algorithm that substantially improved separation of the genotypes and will be used in subsequent analyses of these data (Figure 27C-E).

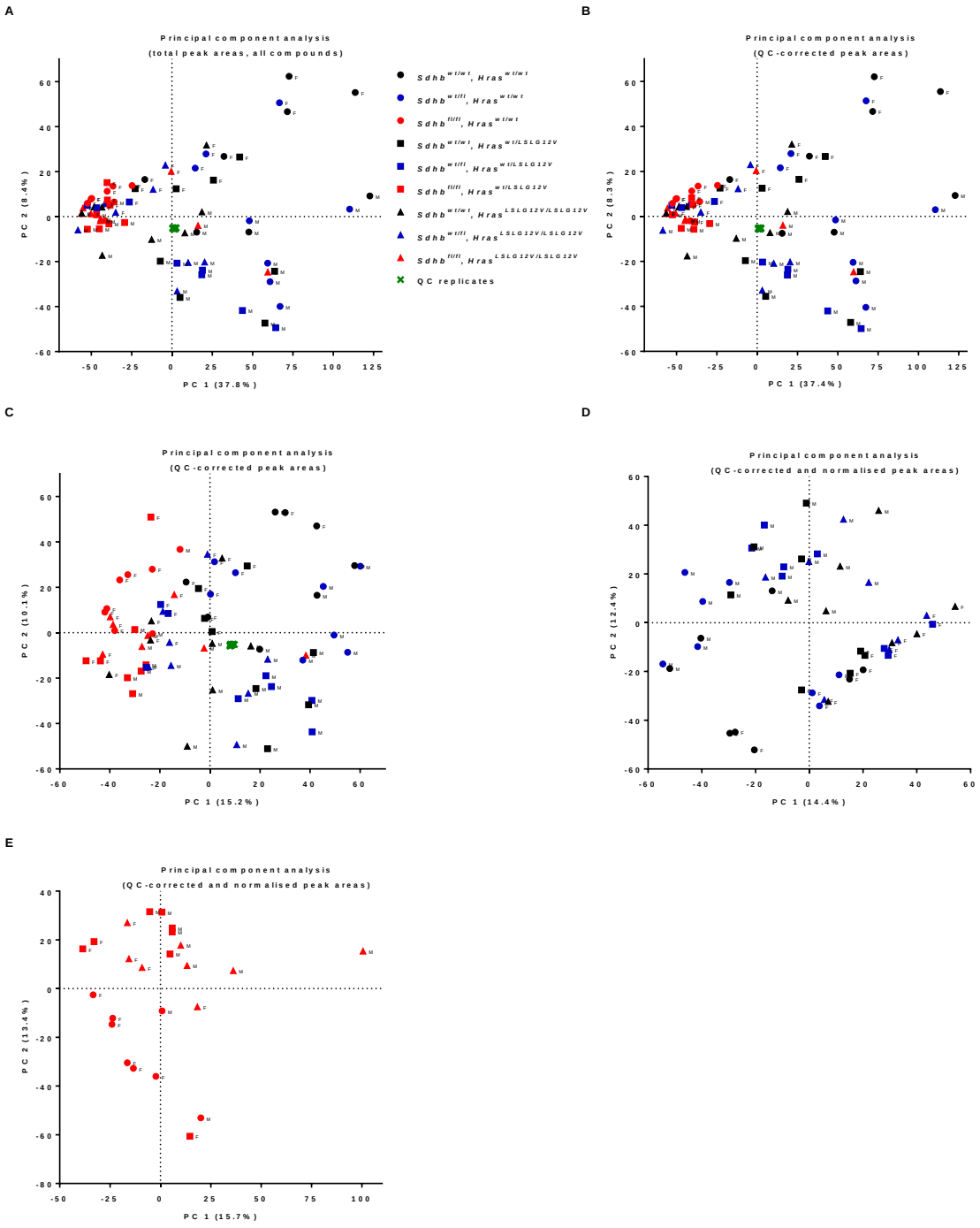

Figure 27: Principal component analyses of untargeted metabolomics data obtained from *KspCre*$^{+}$ urine samples. Data are presented for all genotypes and quality control replicates (QC) based on raw peak areas of all compounds detected **(A)**, after correction for QC replicates **(B)**, after additional normalisation using a 'constant sum' approach **(C)**, for SDHB-proficient genotypes after QC correction and 'constant sum' normalisation **(D)** and **(E)** for *Sdhb*$^{fl/fl}$ specimens after identical processing as in (D).

4.2.4 A first approach to identifying SDHB loss-related biomarkers in the *KspCre*$^{+}$ model

It became obvious from PCA data that the plasma data set contained least complexity and from a global view only gradual deviations in *Sdhb*$^{fl/fl}$, *Hras*$^{wt/wt}$

and $Sdhb^{fl/fl}$, $Hras^{wt/LSLG12V}$ samples from controls. Therefore, I queried this data set for potential discoveries (FDR-adjusted p value <0.05) comparing $Sdhb^{fl/fl}$ to $Sdhb^{wt/wt}$ specimens matched for *either* $Hras^{wt/wt}$ or $Hras^{wt/LSLG12V}$ genotype that would additionally show significant difference (p<0.05) in the other comparison.

Query A: FDR-adjusted p($Sdhb^{fl/fl}$, $Hras^{wt/wt}$ *vs.* $Sdhb^{wt/wt}$, $Hras^{wt/wt}$) <0.05
AND
p($Sdhb^{fl/fl}$, $Hras^{wt/LSLG12V}$ *vs.* $Sdhb^{wt/wt}$, $Hras^{wt/LSLG12V}$) <0.05

Query B: FDR-adjusted p($Sdhb^{fl/fl}$, $Hras^{wt/LSLG12V}$ *vs.* $Sdhb^{wt/wt}$, $Hras^{wt/LSLG12V}$) <0.05
AND
p($Sdhb^{fl/fl}$, $Hras^{wt/wt}$ *vs.* $Sdhb^{wt/wt}$, $Hras^{wt/wt}$) <0.05

Of note, the $Hras^{LSLG12V/LSLG12V}$ condition was not employed in biomarker screening approaches as kidney dysfunction was most pronounced in $KspCre^{+}$, $Sdhb^{fl/fl}$ mice of this *Hras* background.

Query A resulted in exactly one compound (MW: 139.02690; RT: 5.096) that fulfilled the condition. Subsequently, kidney and urine data set were searched for corresponding compounds. In both of them, two potential candidate matches were identified and are plotted in Figure 28, of which potential matches with slightly higher retention time in kidneys and urines would fulfil ideal conditions for a biomarker (elevated in kidney, plasma and urine). In contrast, the compounds with lower retention times would rather display a predicted pattern of accumulation as a result of renal insufficiency (high in kidney and plasma, lower excretion in urine). Automated identification algorithms suggest Hydroxynicotinate as a potential identity of the compound and, disappointingly, analyses of MS2 spectra suggested urine and kidney compounds with lower RT to be genuine matches of the potential plasma biomarker. The result of query A was therefore not followed up.

Query B retrieved, in addition to the compound discussed above, another 15 additional compounds that are listed in Table 14. These were recapitulated in kidney and plasma data sets as well with only one of them (MW: 351.16332, RT: 9.694) fulfilling the condition of increased levels in $Sdhb^{fl/fl}$ genotypes in all three data sets (Figure 29). In the kidney data set, the compound does not pass the QC

correction threshold, so uncorrected total peak areas were analysed here. Besides a suggested a structural similarity to the amino acid valine, the identity of the corresponding metabolite still needs to be uncovered.

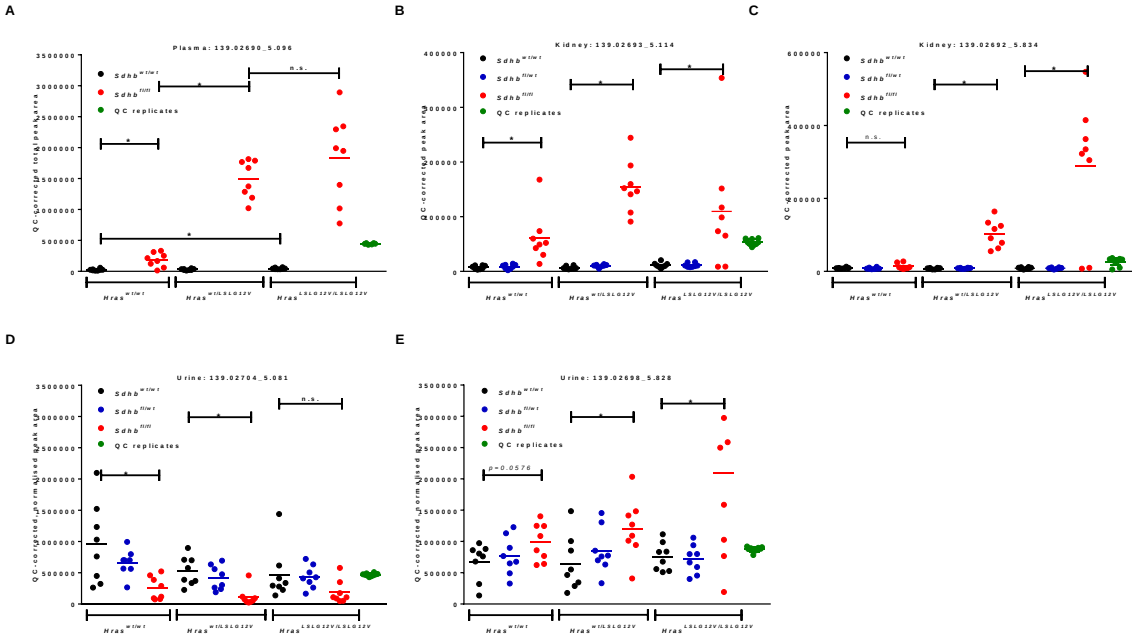

Figure 28: (A) Detected levels of plasma compound 139.02690_5.096 and two potential corresponding compounds in kidney (B, C) and urine (D, E)

Hit no.	MW	RT [min]	Ratio: *Hras*$^{wt/wt}$	Ratio: *Hras*$^{wt/LSLG12V}$	Ratio: *Hras*$^{LSLG12V/LSLG12V}$	p (*Hras*$^{wt/wt}$)	p (*Hras*$^{wt/LSLG12V}$)	p (*Hras*$^{LSLG12V/LSLG12V}$)	FDR-adj. p (*Hras*$^{wt/wt}$)	FDR-adj. p (*Hras*$^{wt/LSLG12V}$)	FDR-adj. p (*Hras*$^{LSLG12V/LSLG12V}$)	urine change *Sdhb*$^{fl/fl}$:*Sdhb*$^{wt/wt}$	kidney change Sdhb$^{fl/fl}$:Sdhb$^{wt/wt}$
1	104.02248	7.658	2.119	1.968	9.476	0.02989719	0.002017911	1.19804E-12	1	0.033984769	3.10991E-11	down	(up)
2	128.05856	12.742	1.898	2.38	6.398	0.01097054	6.5583E-05	1.14941E-12	0.878421722	0.002539	3.10991E-11	no change	(up)
3	128.05859	11.945	2.953	5.508	4.22	0.00823955	0.000444368	0.025049306	0.744306102	0.012902536	0.066576531	no change	(up)
4	129.07891	8.16	3.322	6.404	6.497	0.0005422	1.54906E-10	1.04952E-10	0.220405297	6.29693E-08	1.35438E-09	no change	up
5	129.07892	9.69	2.073	3.983	11.839	0.01785704	3.41412E-07	1.53155E-12	0.919828771	3.96526E-05	3.3475E-11	no change	up
6	139.0269	5.096	7.913	52.353	46.866	1.8758E-06	1.0586E-12	1.06937E-12	0.001525058	8.6064E-10	3.10991E-11	up/no change	up
7	160.08483	10.596	1.986	2.552	3.331	0.03062988	0.001075416	0.032354185	1	0.023008249	0.08350461	(down)	not found
8	164.06902	9.014	1.408	2.563	1.584	0.00236788	1.23502E-09	0.000854351	0.385017965	3.34692E-07	0.002882104	no change	up
9	169.08502	9.967	1.593	3.136	2.837	0.01464261	3.16904E-08	1.43212E-07	0.915726251	5.15287E-06	8.62454E-07	down	no change
10	174.10036	11.037	2.511	2.845	3.01	0.0178431	1.38581E-06	1.21007E-05	0.919828771	8.66667E-05	5.20522E-05	no change	(up)
11	177.99738	7.771	3.121	8.062	9.311	0.00082636	5.29344E-09	7.37086E-09	0.223944802	1.07589E-06	5.65331E-08	no change	up
12	189.1112	13.145	2.539	4.106	9.037	0.01257686	3.35701E-06	4.43592E-10	0.878421722	0.000194946	4.39805E-09	down	up
13	202.13176	11.93	3.247	3.327	3.832	0.00361928	0.000251039	3.19981E-05	0.420353109	0.007849785	0.00130072	no change	up
14	270.06261	9.725	4.012	10.046	30.909	0.00355317	1.2925E-06	1.60962E-11	0.420353109	8.66667E-05	2.37932E-10	no unique match	up
15	272.05964	9.723	4.194	11.427	29.348	0.0018593	1.5926E-07	5.30376E-12	0.377903413	2.15797E-05	8.13576E-11	no unique match	up
16	351.16332	9.694	3.268	5.903	26.815	0.00818304	4.52348E-07	1.08114E-12	0.744306102	4.59699E-05	3.10991E-11	up	up

Table 14: Overview of "hits" in query B and alterations in *Sdhb*$^{fl/fl}$ kidneys and urines. Ratios, p values and adjusted p values refer to the *Sdhb*$^{fl/fl}$ *vs* *Sdhb*$^{wt/wt}$ comparison for the given *Hras* genotype in plasma.

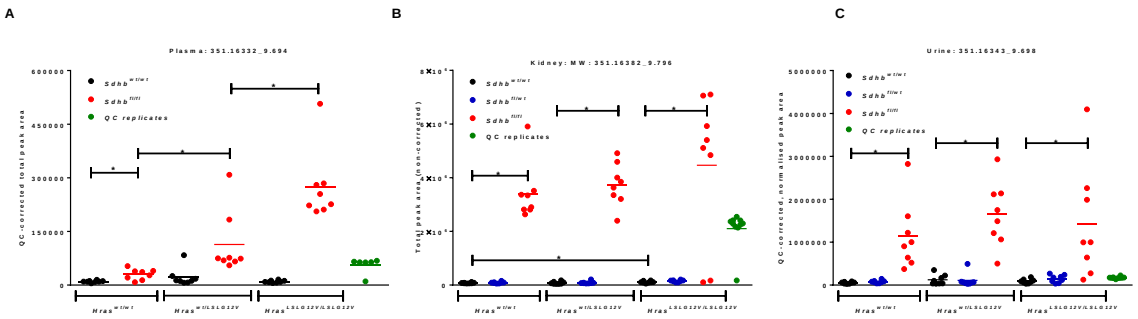

Figure 29: (A) Profiles of plasma compound 351.16332_9.694 and corresponding compounds in kidney (B) and urine (C).

4.2.5 Discussion

This chapter has introduced ongoing untargeted metabolomic approaches to find new biomarkers of SDH-deficient tumours by integrating studies of different biomaterials derived from the *KspCre*$^{+}$, *Sdhb*^{fl}, *Hras*^{LSLG12V} model. The most interesting findings from targeted analyses of the three biological sample classes are for me the elevated aspartate levels in SDHB-proficient mice carrying *Hras*^{LSLG12V} alleles, lack of differences in succinate levels between *Sdhb*$^{fl/fl}$ cohorts and similar abundancies of aspartate and succinate in plasma for all genotypes. These data could even argue for a metabolic route of succinate "detoxification" to sustainable levels induced by *Hras*^{G12V} in SDH-deficient compartments. However, in order to accurately determine individual metabolite levels in a targeted approach, serial dilutions of metabolite standards need to be processed in parallel to the biological samples to ensure detection of metabolites of interest within a linear response range of the mass spectrometer. Results of the corresponding experiment are currently still outstanding.

PCA analyses clearly show the different dynamics of *Sdhb*$^{fl/fl}$ and *Hras*^{LSLG12V} effects in metabolic profiles of kidney tissue, plasma and urine: Whereas urines of young *Sdhb*$^{fl/fl}$, *Hras*$^{wt/wt}$ animals are already dramatically altered, their plasma metabolom still closely resembles the wildtype condition. Besides, the structure of the data set has revealed until then not entirely recognised, substantial sex-specific variation within genotypes.

Much higher fluid intake in *KspCre*$^{+}$, *Sdhb*$^{fl/fl}$ mice and lower creatinine abundancies in their urines are highly suggestive of generally diluted urine metabolomes in these animals and justify a biological normalisation step for the

urine data set with the aim to properly control for urine concentration. It can even be speculated that increased renal succinate concentrations directly trigger glomerular hyperfiltration with higher consecutive urine excretion similar to the diabetic condition (22).

Metabolic alterations due to progressive renal failure need to be identified as a confounder in biomarker studies employing *KspCre*$^{+}$, *Sdhb*$^{fl/fl}$ mice. I am convinced that reasonable assumptions about expected reaction patterns of SDH-related biomarkers in kidney, blood and urine can help to distinguish them from alterations that are caused by kidney dysfunction. In this regard, succinate with its high abundance in *Sdhb*$^{fl/fl}$ kidneys (reflecting increased production) combined with high urinary excretion is altered in an entirely different pattern from creatinine, a typical marker of renal function (high in kidney and plasma due to impaired urinary excretion). Starting from the least complex of our metabolomics data sets (plasma), two candidate compounds have already been identified and now need to be annotated and validated. Furthermore, similar approaches starting from the other two data sets now have to be advanced and could equally lead to promising candidate biomarkers.

4.3 Summary

Chapter 4 describes still preliminary results of our first steps into untargeted metabolomics approaches in order to identify new biomarkers of SDH-deficient tumours. Employing established methods for detection of small polar metabolites combined with the CompoundDiscoverer software platform, we have profiled kidneys, plasma and urines in eight biological replicates per genotype. Metabolic alterations in the *Sdhb*$^{fl/fl}$ condition were generally most pronounced in urine and least evident in plasma samples, and major sex-related differences in metabolic profiles were noted in *Sdhb*$^{wt/wt}$ mice. Excretory kidney insufficiency is a model-inherent limitation that has to be taken into account for biomarker studies in the *KspCre* model. However, integration of information from the three data sets that I have generated in this model might be a successful strategy to circumvent this problem and has already led to two candidate compounds that will be further investigated after submission of this thesis.

5 Phenotypic and metabolic effects of *RosaCreER^{T2}*-driven recombination in *Sdhb$^{fl/fl}$* mice

5.1 Introduction

In chapters 3 and 4, I have discussed findings in a mouse model that is based on a constitutively-expressed, genetically encoded Cre activity in a defined cellular compartment from an early developmental stage on.

This chapter summarises our approach to study consequences of acutely inactivating *Sdhb* in different healthy adult tissues by temporary inducing nuclear Cre translocation and activity using a *RosaCreER^{T2}* system. An initial goal of this strategy was to identify organs that are specifically vulnerable to loss of SDH activity. Furthermore, we were also aiming at testing if certain tissues can be neoplastically transformed by combined deletion of *Sdhb* and activation of oncogenic *Hras* (*Hras$^{wt/LSLG12V}$*).

It is conceptually important to clarify here that tamoxifen-induced *RosaCreER^{T2}* Cre activity primarily targets the genome, but does not directly interfere with expression of functional RNA transcripts and translated proteins. This means that in tissues with low cellular turnover or proliferation rate, at least proteins with a high half-life time would be predicted to remain relatively unaffected by deletion strategies (*i.e.* in *Sdhb$^{fl/fl}$* animals) even in the event of recombination of both conditional alleles in the same cell. Furthermore, genetic recombinations of individual conditional alleles in the same cell have to be considered as independent biological events that (for reasons that have been discussed in section 2.1.1.2.) occur with different efficacy, especially in a context of a temporarily induced Cre activity (such as in the *RosaCreER^{T2}* system). The extent of Cre activity in different tissues will be directly correlated to the dose of the transgene-inducing agent applied and might reach levels that become systemically toxic to the entire organism. Therefore, biological outcomes can be dose-dependent and diverse.

5.2 Results

5.2.1 Experimental setting

Initially, *RosaCreER^{T2+}, Sdhb$^{wt/wt}$, Hras$^{wt/wt}$*, *RosaCreER^{T2+}, Sdhb$^{fl/fl}$, Hras$^{wt/wt}$* and subsequently *Sdhb* and *Hras^{LSLG12V}* heterozygous mice of the same model were subjected to a locally well established transgene induction dose (a single intraperitoneal [i.p.] injection of tamoxifen at 80 mg/kg body weight, termed "high" dose induction throughout this chapter, please refer to Table 8 for details on induction schemes as well). As this approach turned out to cause short-term toxicity in SDHB-deficient mice that prevented long-term (tumour development) studies, "low" (30 mg/kg body weight) and "medium" (50 mg/kg body weight) dose inductions were conducted in at least 10 mice per genotype. Even after exposure to "low" dose transgene induction, SDHB-proficient *RosaCreER^{T2+}, Hras$^{LSLG12V/LSLG12V}$* mice succumbed to poor clinical condition, weight loss and general skin inflammation/proliferation (not shown) within the first few weeks and were thus excluded from further studies.

At least 10 mice of all *Sdhb* genotypes in *Hras$^{wt/wt}$* and *Hras$^{wt/LSLG12V}$* backgrounds were clinically monitored for 18 months after low dose transgene induction. To recapitulate and maximise phenotypic differences between *Sdhb$^{wt/wt}$, Hras$^{wt/LSLG12V}$* and *Sdhb$^{fl/fl}$, Hras$^{wt/LSLG12V}$* mice and avoid age-related malignancies (that turned out to be a confounder in the 18 months experiment), we lastly induced transgene expression in *Sdhb$^{wt/wt}$* and *Sdhb$^{fl/fl}$* cohorts at a "medium" dose and censored mice one year afterwards.

At the time of thesis submission, only H & E-stained slides of peripheral tissues derived from "high" and "low" dose induction experiments were reviewed for morphological alterations by an independent pathologist, while the "medium dose" experiment was still ongoing.

5.2.2 Progressive weight loss is a selective toxicity of transgene induction in *RosaCreER^{T2+}, Sdhb$^{fl/fl}$* mice

When *RosaCreER^{T2+}, Sdhb$^{fl/fl}$, Hras$^{wt/wt}$* mice were subjected to a single tamoxifen application of 80 mg/kg body weight i.p., a dosing scheme that has been routinely used to induce Cre-mediated recombination in several other *RosaCreER^{T2+}*-based

mouse models at the CRUK Beatson Institute, we noticed a progressive loss of body weight in these mice (Figure 30A). As a consequence, with only two exceptions, all *RosaCreER*$^{T2+}$, *Sdhb*$^{fl/fl}$, *Hras*$^{wt/wt}$ cases had to be sampled within the first six weeks after Cre activation, whilst *RosaCreER*$^{T2+}$, *Sdhb*$^{wt/wt}$, *Hras*$^{wt/wt}$ and *RosaCreER*$^{T2+}$, *Sdhb*$^{wt/fl}$, *Hras*$^{wt/wt}$ animals continued to indistinguishably accumulate body mass (Figure 30B). SDHB-proficient *RosaCreER*$^{T2+}$, *Hras*$^{wt/LSLG12V}$ animals gained less weight over time than their *Hras*$^{wt/wt}$ counterparts. Detrimental weight loss appeared to be less rapid for a subgroup of *RosaCreER*$^{T2+}$, *Sdhb*$^{fl/fl}$, *Hras*$^{wt/LSLG12V}$ animals (Figure 30C, D), but this delay did not significantly prolong survival in comparison to the *RosaCreER*$^{T2+}$, *Sdhb*$^{fl/fl}$, *Hras*$^{wt/wt}$ cohort (Figure 31).

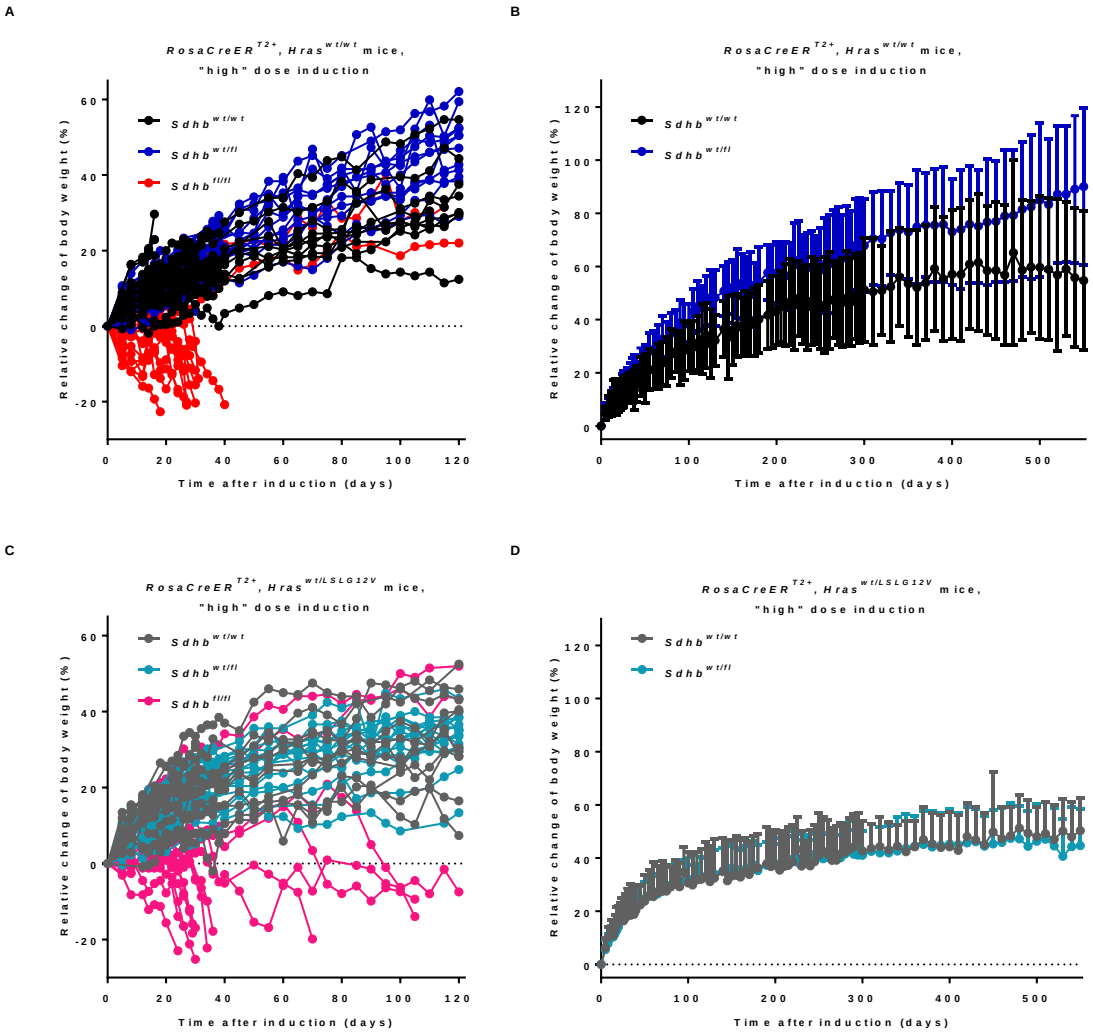

Figure 30: Weight changes relative to body weight at transgene induction of *RosaCreER*$^{T2+}$, *Hras*$^{wt/wt}$ (A, B) and *RosaCreER*$^{T2+}$, *Hras*$^{wt/LSLG12V}$ (C, D) cohorts for individual mice over the first 4 months (A, C) and averaged per SDHB-proficient genotype over 18 months (B, D) after transgene induction at "high" dose (80 mg/kg).

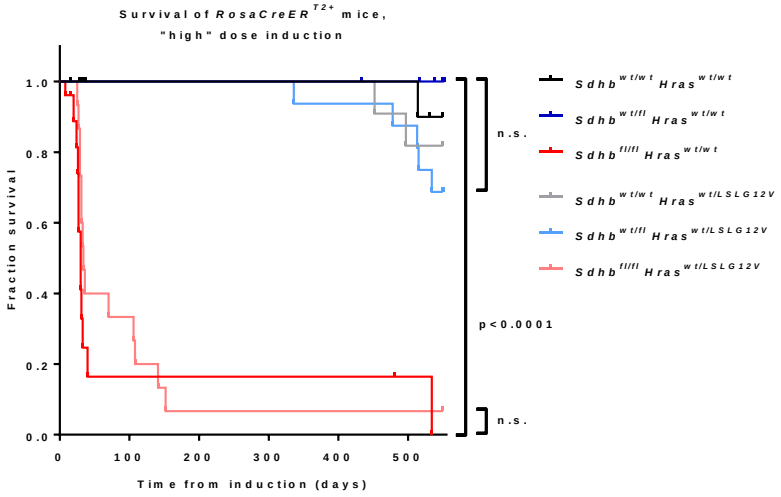

Figure 31: Survival of *RosaCreER*$^{T2+}$ mice after a "high" transgene induction dose (80mg/kg tamoxifen i.p.)**.**

Compared to samples collected from *RosaCreER*$^{T2+}$, *Sdhb*$^{wt/wt}$, *Hras*$^{wt/wt}$ mice, succinate progressively accumulated to endpoints in urine specimens of *RosaCreER*$^{T2+}$, *Sdhb*$^{fl/fl}$, *Hras*$^{wt/wt}$ animals, while aspartate abundancies were reduced to much lower values (Figure 32) and creatinine levels (used to normalise individual samples for urine concentration) were not significantly changed between groups (Figure 32C, D, E). We therefore reasoned that the detrimental cachexia observed in *RosaCreER*$^{T2+}$, *Sdhb*$^{fl/fl}$ animals was most likely a direct consequence of SDHB deletion in at least one peripheral organ.

However, besides an obvious loss of white adipose tissue, I could not identify any macroscopic abnormalities in *RosaCreER*$^{T2+}$, *Sdhb*$^{fl/fl}$ animals at clinical endpoints (irrespective of *Hras*^{G12V} activation). To our surprise, an independent histomorphological review of four representative cases per genotype failed to detect an organ pathology caused by SDHB loss (personal communication with Dr. Markus Eckstein, Institute of Pathologie, Universitätsklinikum Erlangen).

We next analysed aspartate and succinate contents in snap-frozen organs of three *RosaCreER*$^{T2+}$, *Sdhb*$^{fl/fl}$, *Hras*$^{wt/wt}$ mice against an equal number of *RosaCreER*$^{T2+}$, *Sdhb*$^{wt/wt}$, *Hras*$^{wt/wt}$ animals (that had been censored at a comparable time-point after tamoxifen application) as a metabolic read-out of SDHB function loss.

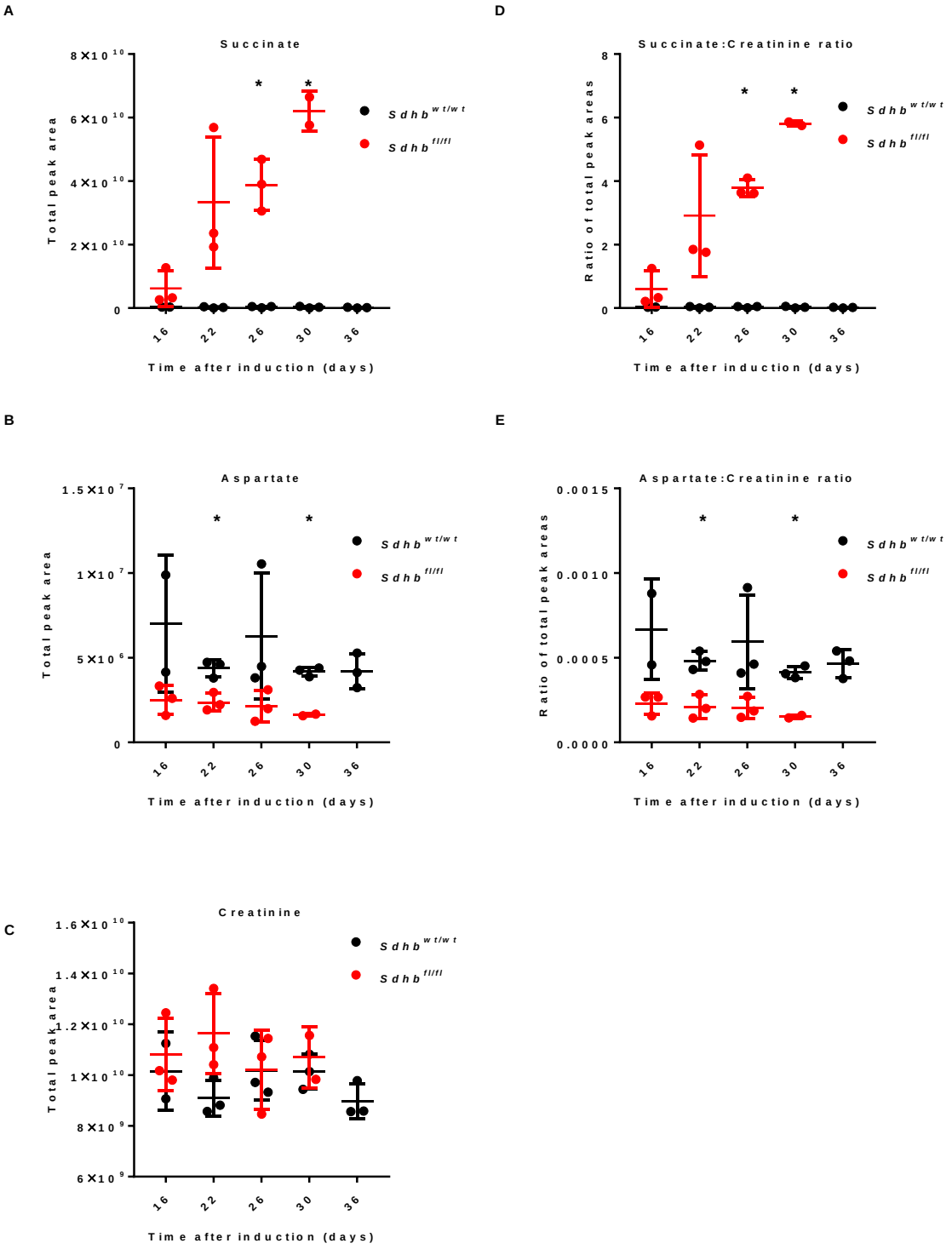

Figure 32: Succinate accumulation (A), aspartate depletion (B) and creatinine abundancies (C) in urines of *RosaCreER*$^{T2+}$, *Hras*$^{wt/wt}$ mice after "high" dose transgene induction. n=3 per genotype for days 16, 22 and 26. As one and three *Sdhb*$^{fl/fl}$ mice had reached endpoints before day 26 and day 30 respectively, less samples could be analysed from day 26. "*" indicates significance ($p<0.05$).

As all tissue specimens were extracted by the same method (*i.e.* at an identical concentration see section 2.2.5) and processed together as one analytical batch, absolute succinate abundancies and variations within the same genotype differed

substantially between organs (Figure 33 A, C) with liver specimens showing the highest succinate abundancies. To best control for different extraction efficacies in various organs, results are depicted as relative changes in individual *Sdhb*$^{fl/fl}$, *Hras*$^{wt/wt}$ compared to the mean of identical *Sdhb*$^{wt/wt}$, *Hras*$^{wt/wt}$ organs in addition (Figure 33 B. D). The highest, significantly increased succinate ratios relative to wildtype controls were noticed in *Sdhb*$^{fl/fl}$, *Hras*$^{wt/wt}$ livers, spleens and, importantly, whole blood samples (Figure 33B). Aspartate ratios (given in Figure 33D) appeared less dramatically altered in general with changes between *Sdhb*$^{wt/wt}$, *Hras*$^{wt/wt}$ and *Sdhb*$^{fl/fl}$, *Hras*$^{wt/wt}$ groups not reaching significance for most organs.

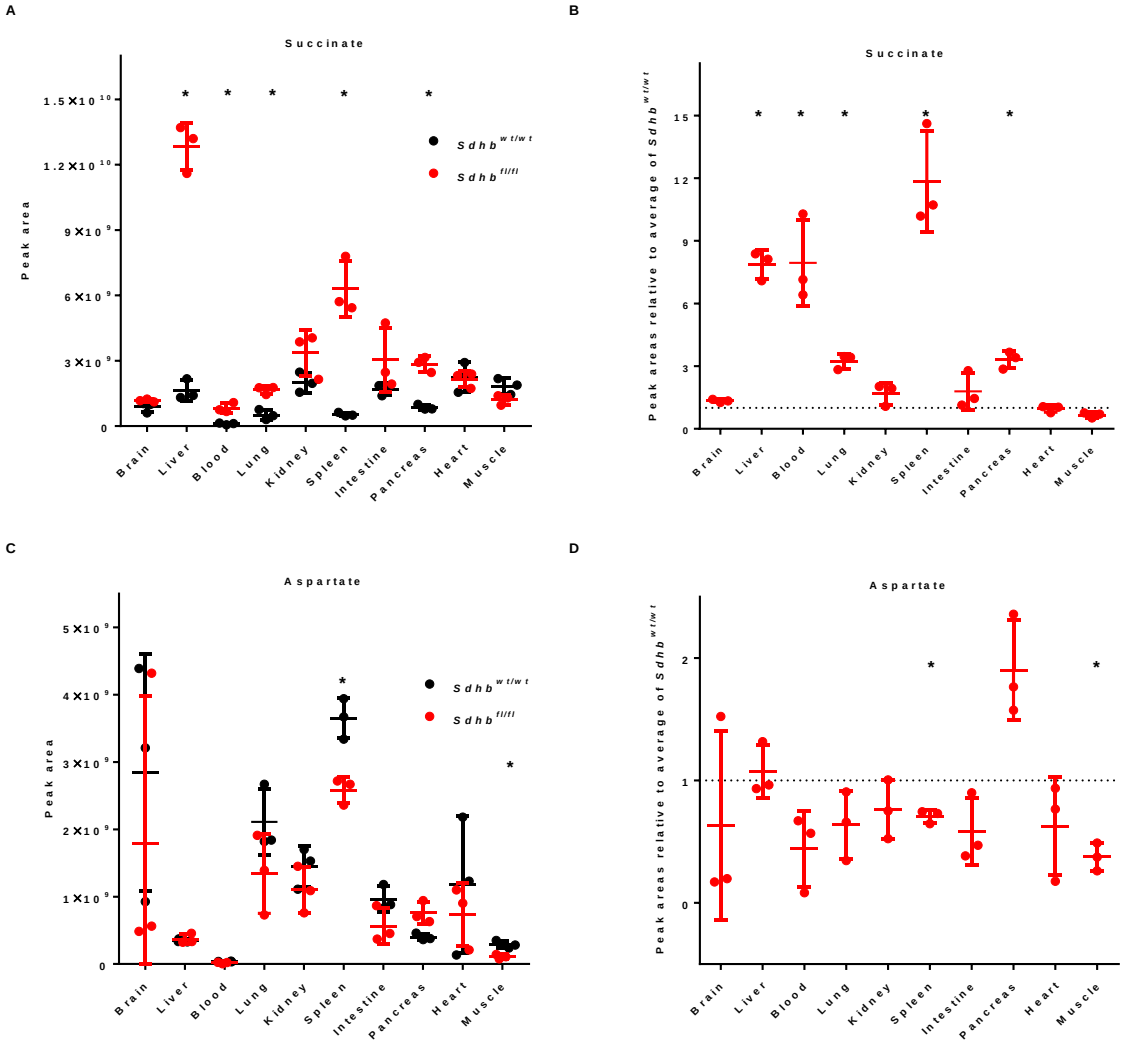

Figure 33: Succinate (A, B) and Aspartate (C, D) concentrations in indicated organs of *RosaCreER*$^{T2+}$, *Sdhb*$^{wt/wt}$, *Hras*$^{wt/wt}$ and *RosaCreER*$^{T2+}$, *Sdhb*$^{fl/fl}$, *Hras*$^{wt/wt}$ mice at clinical endpoints after "high" dose transgene induction (A, C), and in *RosaCreER*$^{T2+}$, *Sdhb*$^{fl/fl}$, *Hras*$^{wt/wt}$ mice relative to the organ-specific average of the equally induced *RosaCreER*$^{T2+}$, *Sdhb*$^{wt/wt}$, *Hras*$^{wt/wt}$ animals (B, D). n=3 per genotype, "*" indicated statistical significance ($p<0.05$).

Our findings of rapid, inevitably detrimental body mass loss in *RosaCreER^{T2+}, Sdhb$^{fl/fl}$* mice after "high" dose transgene induction combined with significantly higher concentrations of circulating succinate in *RosaCreER^{T2+}, Sdhb$^{fl/fl}$* mice and lack of morphologically detectable organ toxicity of our "high" dose transgene induction could be explained by recently published data. Work by Mills and colleagues has established systemically increased succinate levels to function as an activator of thermogenic (*i.e.* uncoupled) respiration in brown adipose tissue and to reduce body weight gain under otherwise obesity-causing feeding conditions (32).

In contrast to corresponding *Hras$^{wt/wt}$* mice, under long-term observation, SDHB-proficient *RosaCreER^{T2+}, Hras$^{wt/LSLG12V}$* animals developed papillomatous skin lesions at locations as outlined in Table 15. These *Hras*-driven changes were scored for each body site based on their maximum diameter and converted into a sum score of sum of site-specific values for each animal. Neither typical papilloma locations nor added scores per animal differed significantly between *RosaCreER^{T2+}, Sdhb$^{wt/wt}$, Hras$^{wt/LSLG12V}$* and *RosaCreER^{T2+}, Sdhb$^{wt/fl}$, Hras$^{wt/LSLG12V}$* mice (Figure 34A).

Location		**Diameter (mm)**	**score**
Face		No change	0
Ears		>0 and <3	1
Forefeet		>2.9 and <6	2
Hindfeet		>6	3
Urogenital			
Tail			
Other (specified for each mouse)			

Table 15: Algorithm for scoring of proliferative skin changes in *RosaCreER^{T2+}* mice

Until censoring 18 months after tamoxifen treatment, several lymphomas formed in *RosaCreER^{T2+}* mice and some *RosaCreER^{T2+}, Hras$^{wt/LSLG12V}$* animals developed tumours of suspected parotid gland origin. A detailed pathological review of these neoplasias as well as of mucosal stomach swellings, that occurred in virtually all *RosaCreER^{T2+}, Hras$^{wt/LSLG12V}$* animals irrespective of *Sdhb* genotype, is still outstanding. However, presence of one *Sdhb^{fl}* allele did not substantially increase

frequency of *Hras*^{LSLG12V}-related internal tumours in the "high" dose transgene induction setting (Figure 34B).

A

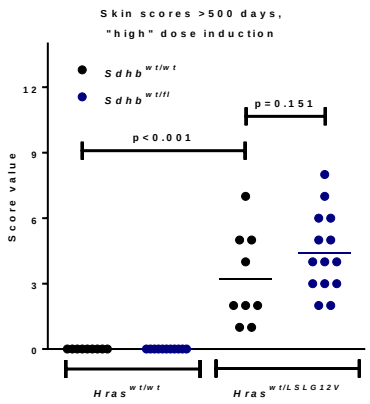

B

RosaCreER $^{T2+}$ Genotype	*Hras* $^{wt/wt}$	*Hras* $^{wt/LSLG12V}$
Sdhb $^{wt/wt}$	2/9 (22.22%)	4/10 (40%)
Sdhb $^{wt/fl}$	0/11 (0%)	7/15 (46.67%)

Figure 34: Total skin tumour scores (A) and frequencies of internal tumours (B) in SDHB-proficient *RosaCreER*$^{T2+}$ cohorts after "high" dose transgene induction (tamoxifen 80 mg/kg). Statistics: Mann–Whitney *U* test.

5.2.3 *Hras*-related skin tumourigenesis is facilitated in *RosaCreER*$^{T2+}$, *Sdhb*$^{fl/fl}$ mice

As toxicity of the initially applied transgene induction strategy had turned out to prevent long-term studies in *RosaCreER*$^{T2+}$, *Sdhb*$^{fl/fl}$ mice irrespective of *Hras* genotype, a substantially lower tamoxifen concentration (a single injection of 30 mg/kg body weight i.p., "low" dose induction) was subsequently applied to at least 10 *RosaCreER*$^{T2+}$, *Hras*$^{wt/wt}$ and *RosaCreER*$^{T2+}$, *Hras*$^{wt/LSLG12V}$ mice of each *Sdhb* genotype. Cre activity in peripheral tissue could still be indirectly confirmed by induction of RFP protein expression as a result of *Rfp*^{LSL} recombination with this treatment (Figure 35).

In contrast to the "high" dose induction scheme, urines of *RosaCreER*$^{T2+}$, *Sdhb*$^{fl/fl}$, *Hras*$^{wt/wt}$ mice were virtually equal with regards to succinate and aspartate content (Figure 36, depicted relative to individual creatinine abundancies) to treatment- and time-matched *Sdhb* wildtype controls. Most importantly, neither progressive accumulation of succinate nor consistent aspartate depletion over the first month after "low" dose transgene induction (cf. Figure 32 for the "high" dose scheme) were detected in *Sdhb*$^{fl/fl}$ specimens.

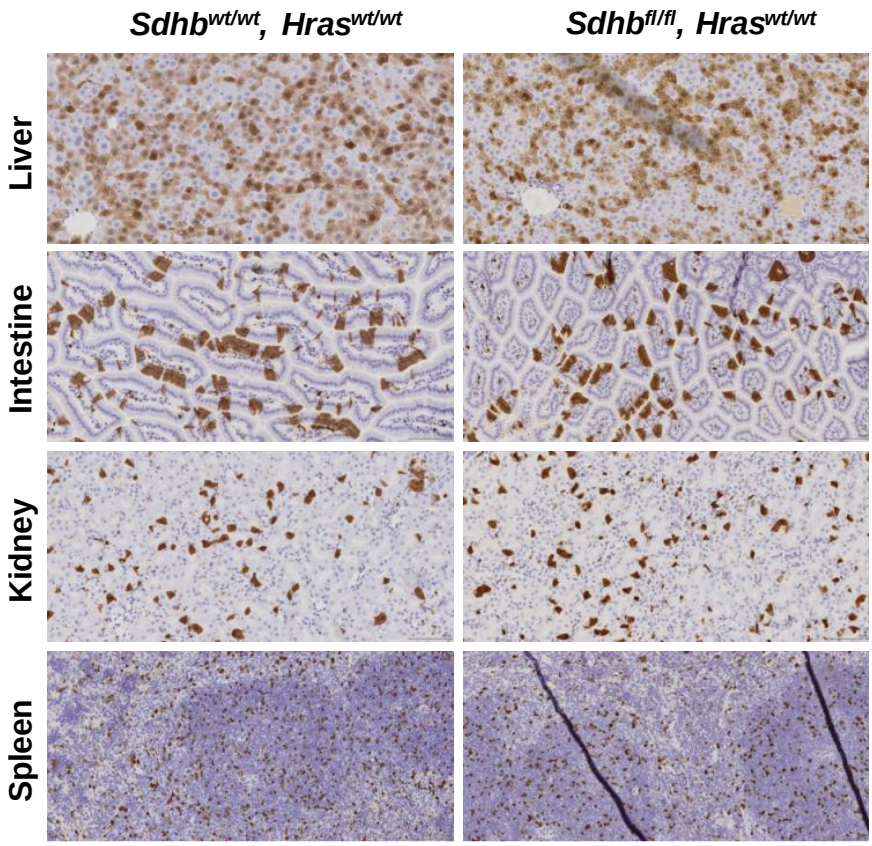

Figure 35: RFP reactivity in two representative *RosaCreER*$^{T2+}$, *Hras*$^{wt/wt}$ cases approx. 5 weeks after "low" dose transgene induction..

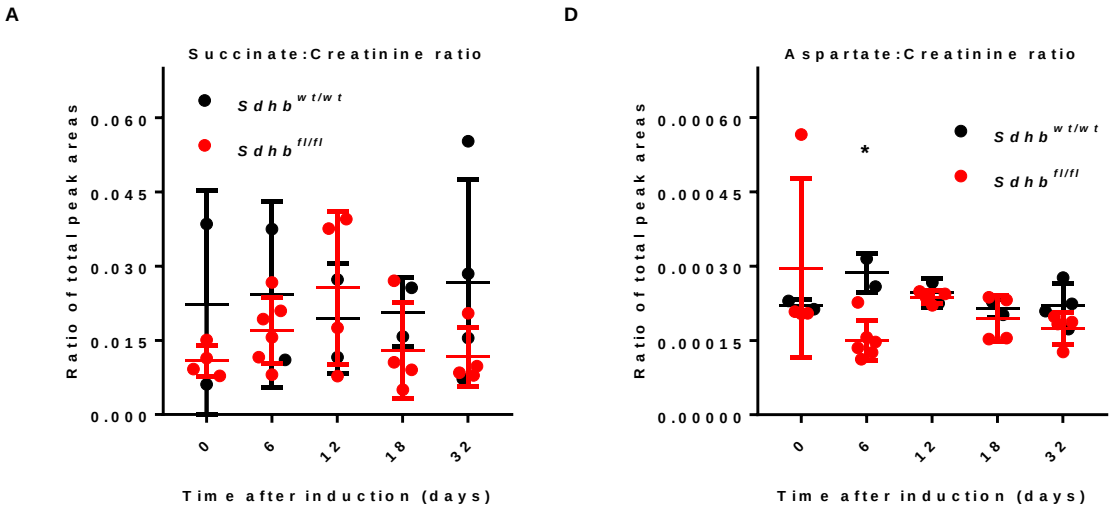

Figure 36: Succinate (A) and aspartate (B) ratios relative to individual creatinine levels in urines of *RosaCreER*$^{T2+}$, *Hras*$^{wt/wt}$ mice after "low" dose transgene induction. n=(2-6) per genotype and time point. Except for aspartate ratios after 6 days, all comparisons between genotypes are non-significant. "*" indicates significance ($p<0.05$).

Using the "low" dose transgene induction scheme, we were able to study all genotypes without loss of *Sdhb*$^{fl/fl}$ animals due to cachexia development, but again noticed reduced weight gain in *Hras*$^{wt/LSLG12V}$ compared to *Hras*$^{wt/wt}$ cohorts (Figure

37) as well as stomach alterations in all *Hras*$^{wt/LSLG12V}$ animals under long-term observation (not shown).

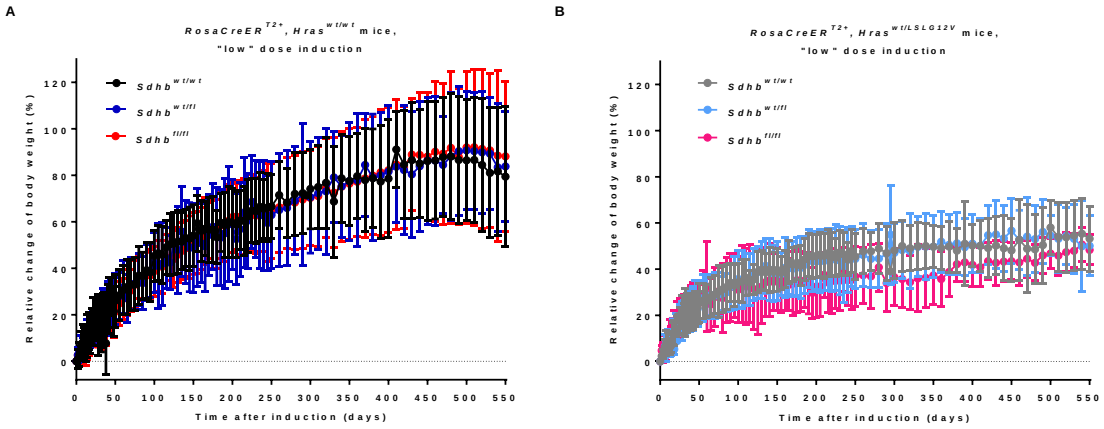

Figure 37: Weight changes (relative to body weight at transgene induction) of *RosaCreER*$^{T2+}$, *Hras*$^{wt/wt}$ (A) and *RosaCreER*$^{T2+}$, *Hras*$^{w/tLSLG12V}$ (B) cohorts averaged per genotype over 18 months after transgene induction at "low" dose (30 mg/kg).

As the most striking clinical difference between *RosaCreER*$^{T2+}$, *Sdhb*$^{wt/wt}$, *Hras*$^{wt/LSLG12V}$ and *RosaCreER*$^{T2+}$, *Sdhb*$^{fl/fl}$, *Hras*$^{wt/LSLG12V}$ animals, a more severe degree of papillomatous skin alterations evolved in *RosaCreER*$^{T2+}$, *Sdhb*$^{fl/fl}$, *Hras*$^{wt/LSLG12V}$ cases (exemplified in Figure 38), whilst not significantly impairing overall survival in comparison to *RosaCreER*$^{T2+}$, *Sdhb*$^{wt/wt}$, *Hras*$^{wt/LSLG12V}$ mice (Figure 39A). As a result, when applying the same skin evaluation scheme as described in section 5.2.2 18 months after tamoxifen injection, I noticed significantly higher total skin score values in this genotype (Figure 39B). As a qualitative distinction, besides at skin areas that are typically exposed to high degrees of mechanical stress (such as feet and face), some (but not all) *RosaCreER*$^{T2+}$, *Sdhb*$^{fl/fl}$, *Hras*$^{wt/LSLG12V}$ mice developed lesions in skin areas that were almost never (ears) or never (tail) affected in other genotypes.

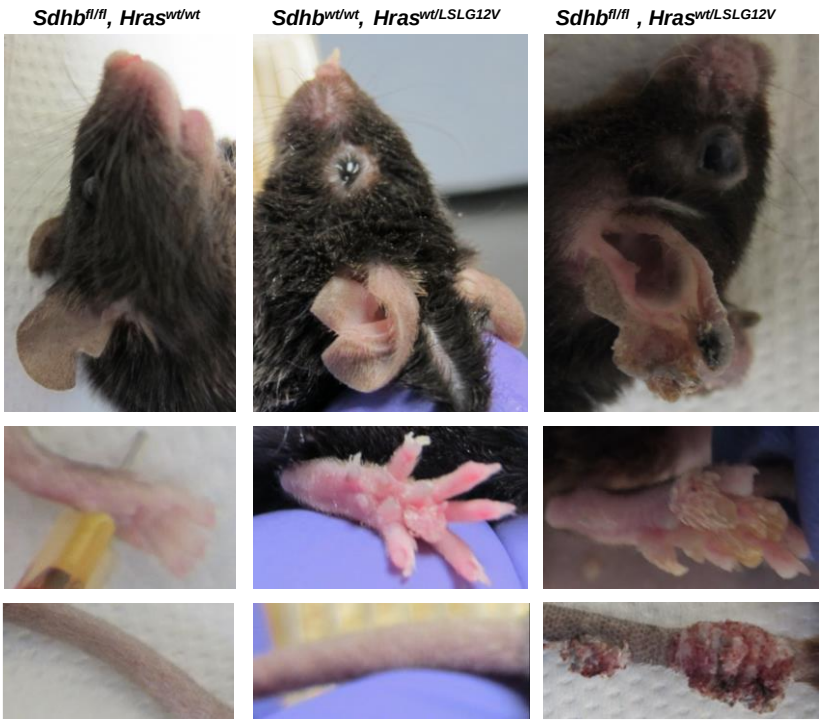

Figure 38: Examples of proliferative skin changes in *RosaCreER*$^{T2+}$ animals of the indicated genotypes approximately 18 months after "low" dose transgene induction.

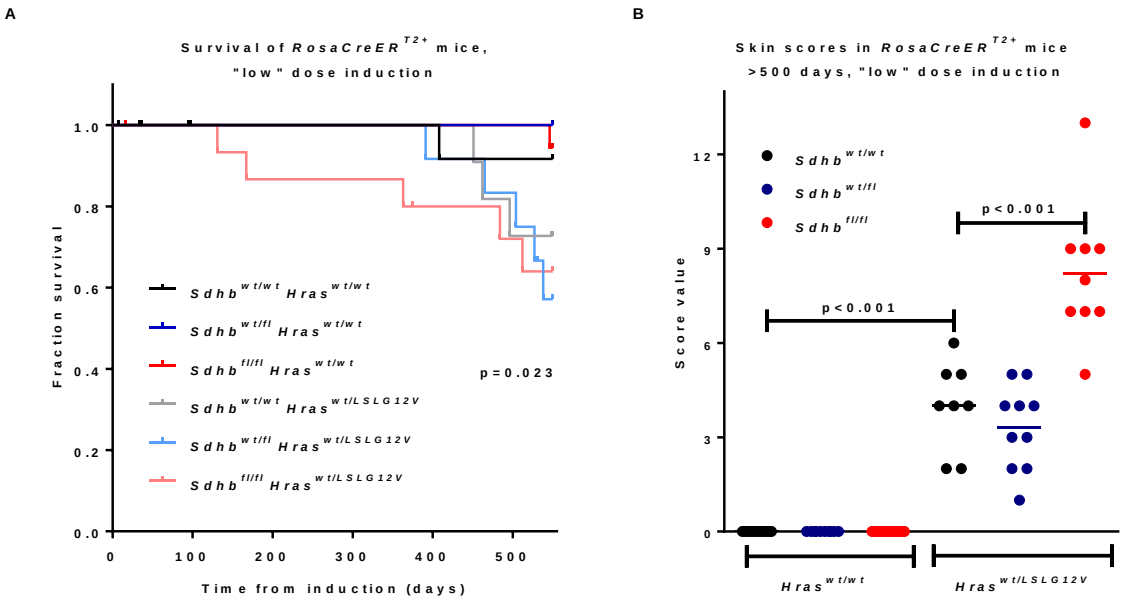

C

RosaCreER $^{T2+}$ Genotype	*Hras* $^{wt/wt}$	*Hras* $^{wt/LSLG12V}$
Sdhb $^{wt/wt}$	3/12 (25%)	4/11 (36.36%)
Sdhb $^{wt/fl}$	2/10 (20%)	4/11 (36.36%)
Sdhb $^{fl/fl}$	3/17 (17.64%)	3/13 (23.08%)

Figure 39: Overall survival (A), skin tumour scores (B) and frequencies of internal tumours (C) in *RosaCreER*$^{T2+}$ cohorts after "low" dose transgene induction (tamoxifen 30 mg/kg). Differences in survival between the three *Hras*$^{wt/LSLG12V}$ cohorts are not significant.

None of the internal tumour types that occurred in the cohorts after "low" transgene induction dose could be clearly associated specifically with the *Sdhb*$^{fl/fl}$ genotype (Figure 39C).

Lastly, in order to circumvent age-related tumour onset in our *RosaCreER*$^{T2+}$-based models and to increase recombination efficacy, we decided to apply a third, "medium" tamoxifen concentration (50 mg/kg body weight as a single injection i.p.) to *RosaCreER*$^{T2+}$, *Sdhb*$^{wt/wt}$ and *RosaCreER*$^{T2+}$, *Sdhb*$^{fl/fl}$ cohorts of both *Hras*$^{wt/wt}$ and *Hras*$^{wt/LSLG12V}$ background and to monitor animals for one year instead of 18 months. *Sdhb*$^{wt/fl}$ cases were excluded from this approach as these had already been shown to be clinically indistinguishable from *Sdhb*$^{wt/wt}$ controls 18 months after the "high" dose induction scheme (chapter 5.2.2). This experiment is still ongoing at the time of thesis submission, but the majority of animals have been sampled with none of them revealing any macroscopic internal tumours. With regards to weight changes, the "medium" dose induction resulted in a mixed picture with long-term tolerability to most *Sdhb*$^{fl/fl}$ mice (Figure 40) but by trend (*Hras*$^{wt/wt}$) or significantly (*Hras*^{wtLSLG12V}) lower weight gains than *Sdhb*$^{wt/wt}$ animals in at the end of observation (Figure 41A).

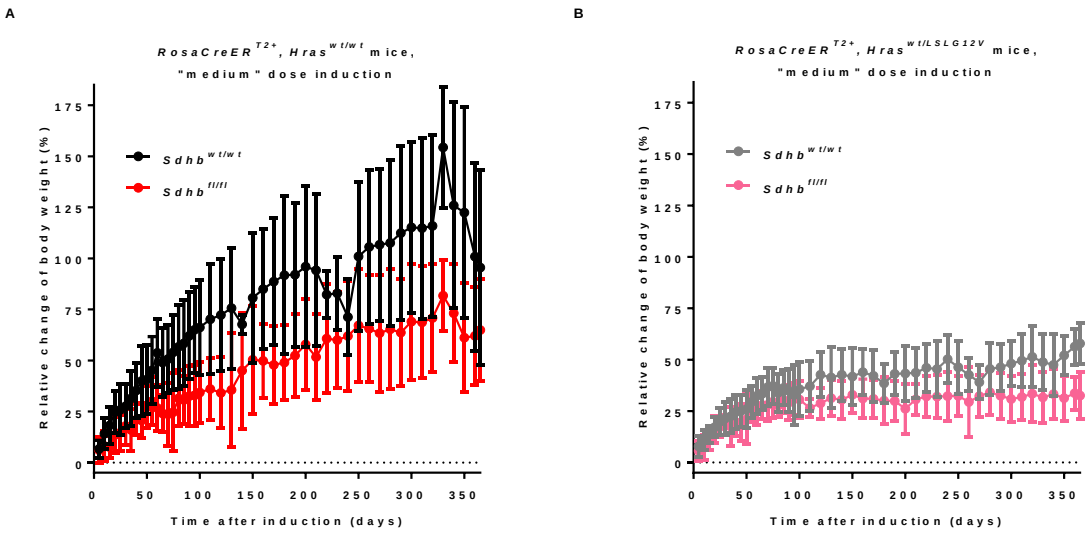

Figure 40: Weight changes (relative to body weight at transgene induction) of *RosaCreER*$^{T2+}$, *Hras*$^{wt/wt}$ (A) and *RosaCreER*$^{T2+}$, *Hras*$^{w/tLSLG12V}$ (B) cohorts averaged per genotype over 12 months after transgene induction at "medium" dose (tamoxifen 50 mg/kg).

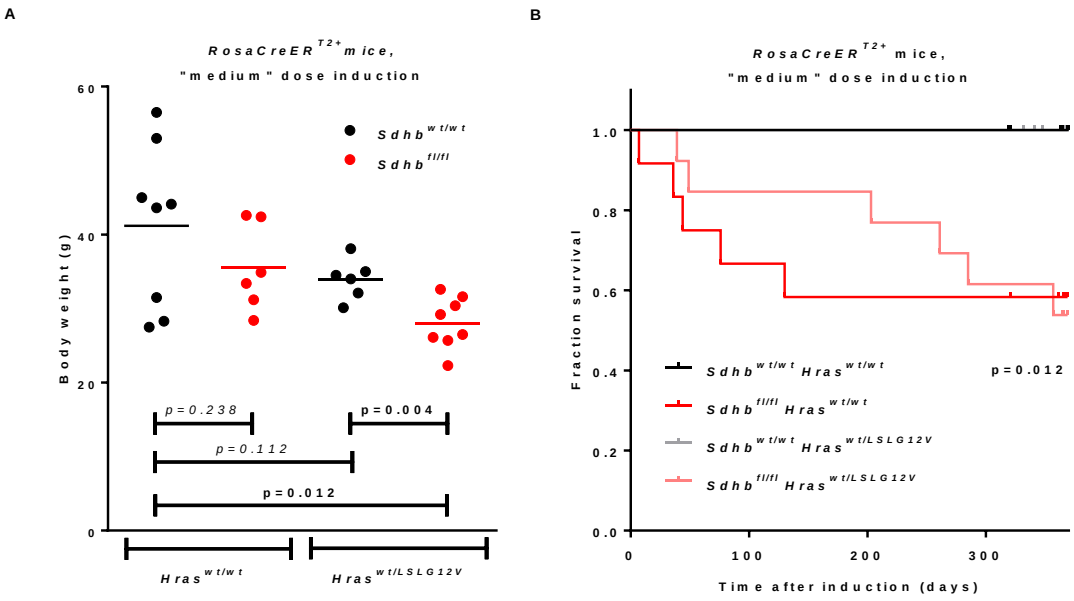

Figure 41: (A) Body weights after 1 year (357-370 days) and survival (B) of the indicated *RosaCreER*$^{T2+}$ cohorts in response to "medium" dose tamoxifen induction (50mg/kg). To illustrate trends towards lower body weights compared to the wildtype condition, individual p values are indicated in (A). Survival of the two *Sdhb*$^{fl/fl}$ cohorts is significantly different to *Sdhb*$^{wt/wt}$ genotypes, but not between *Sdhb*$^{fl/fl}$, *Hras*$^{wt/wt}$ *and* *Sdhb*$^{fl/fl}$, *Hras*$^{wt/LSLG12V}$.

In line with reduced weight gains from transgene induction to censoring after one additional year in young, healthy adult mice (Figure 41), at the current stage of analysis, absolute organ weights of livers and both kidneys determined at censoring do not show significant differences between the genotypes, whereas increases in organ-to-body weight ratios rather reflect body weight reductions (Figure 42). In sharp contrast, the mass of *Sdhb*$^{fl/fl}$, *Hras*$^{wt/LSLG12V}$ spleens increased to almost twofold of other genotypes on average. Due to their very low mass, weights of individual adrenals are very difficult to accurately determine and have to be judged with great care, but current data imply increases due to *Sdhb*$^{fl/fl}$ and *Hras*$^{wt/LSLG12V}$ recombination as well. Scheduled histopathological tissue examinations of "medium" dose cohorts will thus devote particular attention to spleens and adrenals.

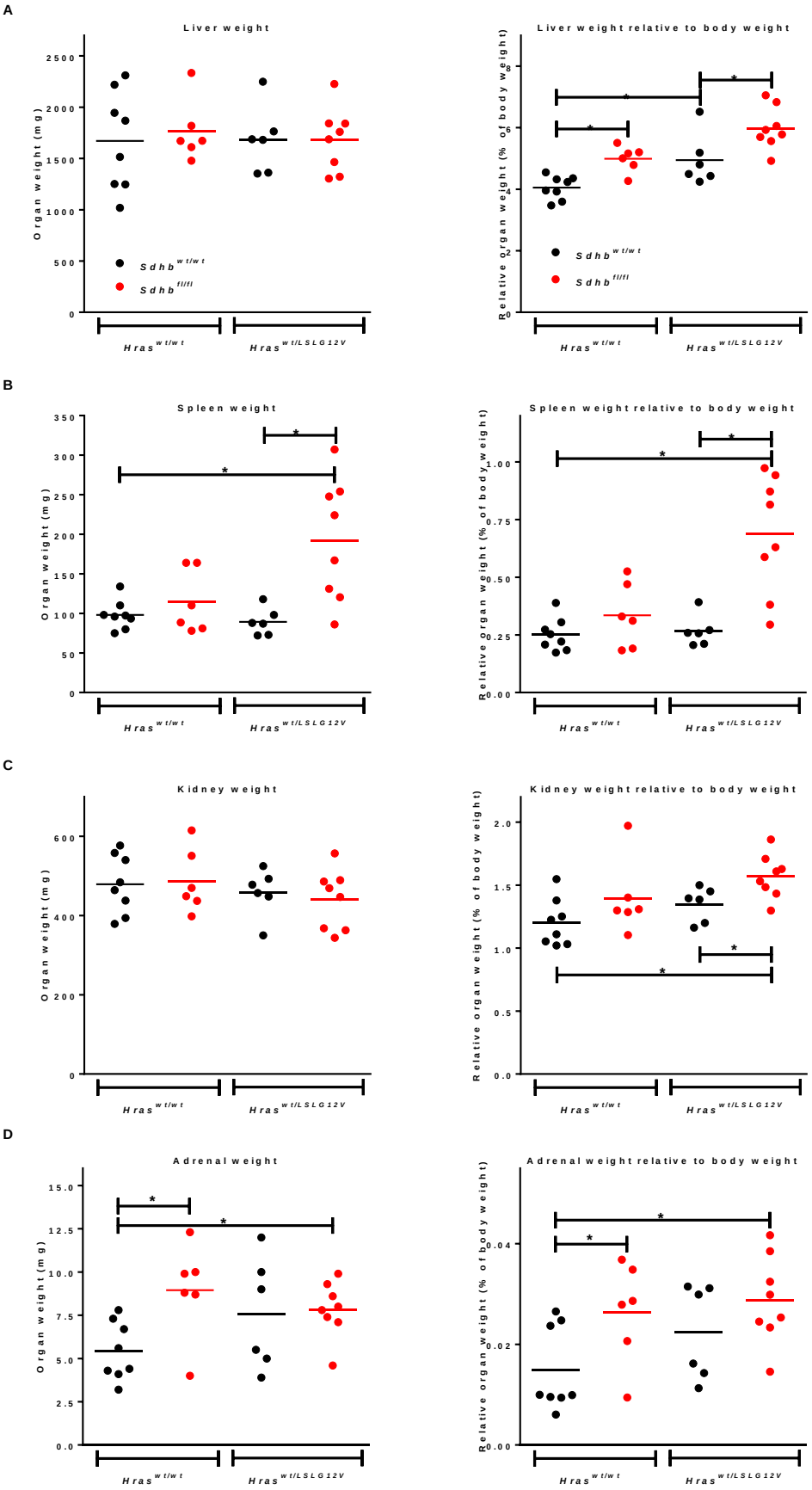

Figure 42: Selected organ weights of *RosaCreER*$^{T2+}$ mice one year after "medium" dose transgene induction plotted as absolute (left) values and relative to body weight (right). (A) Liver, (B) spleen, (C), kidneys, (D), adrenals. Sums of masses of both kidneys and adrenals have been plotted in (C) and (D).

5.3 Discussion

The initial approach to the *RosaCreER*$^{T2+}$ model resulted in progressive, detrimental cachexia selectively in *Sdhb*$^{fl/fl}$ animals. Weight loss in some *Sdhb*$^{fl/fl}$, *Hras*$^{wt/LSLG12V}$ animals appeared to be delayed; differences in survival between the two genetic *Sdhb*$^{fl/fl}$ groups did however not reach statistical significance (Figure 31), arguing against a substantial protective effect of *Hras*^{G12V} in this setting. Disappointingly, we could not detect any phenotypic evidence of *Sdhb* haplo-insufficiency or tumour predisposition in the *Sdhb*$^{wt/fl}$ setting even in the presence of activated *Hras*^{LSLG12V} under monitoring for up to 18 months after transgene induction.

Together with the lack of histologically detectable pathologies in peripheral organs, these observations strongly argue for systemic succinate accumulation itself, but not cellular dysfunction as a result of SDH inactivation as the major mediator of cachexia in *RosaCreER*$^{T2+}$, *Sdhb*$^{fl/fl}$ mice. This interpretation would be in line with the recently described function of succinate as an uncoupler of respiration in brown adipose tissue in mice (32). It is also interesting to note that in response to all three different transgene induction regimens tested, SDHB-proficient *RosaCreER*$^{T2+}$, *Sdhb*$^{fl/fl}$, *Hras*$^{wt/LSLG12V}$ animals gained much less weight than *Hras* wildtype controls and that our models to a certain extent thus recapitulates a central feature of patients carrying germline mutations in the *HRAS* gene (72). Despite several cervical (most likely salivary gland) tumours as typical *Hras*-associated cancer entities (Figure 2), virtually all *RosaCreER*$^{T2+}$, *Hras*$^{wt/LSLG12V}$ animals showed an altered stomach morphology with thickening of the mucosa and macroscopic size increase of the organ. This phenotype still needs to be pathologically defined and could be explained by studies that have detected *Hras* mutations in 4% of stomach cancer cases (and >10% *RAS* gene mutations altogether) in large patient cohorts (114).

Progressive succinate increases in urines of *RosaCreER*$^{T2+}$, *Sdhb*$^{fl/fl}$ mice and higher levels of this metabolite in some, but not all peripheral organs also provide evidence for varying degrees of successful recombination of both *Sdhb*^{fl} alleles after “high” dose transgene induction. Besides site-specific efficacy of genetic recombination, SDHB protein loss in peripheral *Sdhb*$^{fl/fl}$ tissues is most likely also

determined by the rates of proliferation and mitochondrial protein turnover in different organs, since these processes require translation of new SDHB protein.

Despite the very low number of biological replicates per genotype analysed in metabolomics studies in this model, these experiments depict a consistent picture of much more pronounced succinate accumulation than aspartate depletion, with the exception of skeletal muscles showing significantly decreased aspartate abundancies despite succinate levels close to the wildtype condition. As muscle wasting is a common clinical challenge in patients with advanced cancer, studying the influence of succinate (and signalling *via* GPR91) on muscle metabolism could be a promising future area of investigation.

Transgene induction resulted in fatal short-term toxicity in all (n=7) *RosaCreER*^{T2} *Hras*$^{LSLG12V/LSLG12V}$ animals even with the lowest of the three tamoxifen concentrations and irrespective of *Sdhb* status due to poor general body condition skin proliferation. Therefore, these genotypes are not discussed in detail in this thesis. Together with the SDHB loss-imposed upper threshold for transgene induction intensity, limits for studying the effect of *Sdhb* deletions and *Hras*^{LSLG12V} in the *RosaCreER*^{T2} model only permitted long-term analyses with tamoxifen doses presumably resulting in low recombination efficacy for two *Sdhb*^{fl} alleles in the same genome (30 and 50 mg/kg body weight).

The more severe occurrence of skin tumours in *RosaCreER*$^{T2+}$, *Sdhb*$^{fl/fl}$, *Hras*$^{wt/LSLG12V}$ than *RosaCreER*$^{T2+}$, *Sdhb*$^{wt/wt}$, *Hras*$^{wt/LSLG12V}$ animals (again without evidence for *Sdhb* haplo-insufficiency) constitutes the major finding of our long-term observation in this model. The papillomatous neoplasias typically occurred at sites of higher mechanical exposure and were quantitatively (bigger papillomas at typical sites) as well as qualitatively (*i.e.* occurring at sites that were never involved in *Sdhb*$^{wt/wt}$ animals, namely ear and tail) increased in the *Sdhb*$^{fl/fl}$ condition. Non-melanoma skin tumours are not part of the typical *SDH*-deficient cancer spectrum, but amongst the classical *HRAS*-associated tumour types in humans (Figure 2) (75, 114). I find it extremely exciting that, conversely to our *KspCre*-driven renal cell carcinoma model, loss of *Sdhb* or its metabolic consequences here support development of *Hras*-dependent tumourigenesis. The first question to address before committing to further in-depth mechanistic studies of this interaction would from my point of view be if

the observation in our *RosaCreER*$^{T2+}$ model has relevance to human disease. Until submission of my thesis, I could not identify any publically available non-melanoma skin cancer data sets of suitable quality to screen for mutations and copy number alterations in *SDH* genes in this tumour type. An alternative future approach could be to test SDHB protein expression in *Hras*-mutated *versus* non-mutated skin cancer samples.

In general, several mechanisms can be hypothesised as underlying an oncogenic interaction between *Hras* activation in the skin and a certain degree of systemic and/local *Sdhb* deletion: The first obvious thing to analyse (besides classical intracellular actions of the onco-metabolite succinate, please refer to section 1.5) would be auto-/para- or endocrine signalling of succinate through its receptor Gpr91. Of note, the skin is one of the organs with detectable GPR91 expression and downstream effectors of this receptor include typical targets of HRAS (26, 30). Another potential candidate metabolite that can induce a growth-stimulation response *via* downstream effectors of *Hras* and that is secreted by highly glycolytic SDH-deficient cells could be lactate (if found elevated in Sdhb$^{fl/fl}$ skins) (66, 115).

An important technical limitation of my work in the *RosaCreER*$^{T2+}$ system results from the biological independence of recombination events for different individual conditional alleles (*i.e.* they do not necessarily have to occur at similar frequencies or in identical cells at the same time) especially in the context of an only temporary nuclear Cre activity in *RosaCreER*$^{T2+}$ models (88). In contrast to *Hras*$^{wt/LSLG12V}$ and *Rfp*$^{wt/LSL}$, two alleles need to be recombined in Sdhb$^{fl/fl}$ genomes to generate a phenotypic difference which could result in much lower tissue fractions of fully *Sdhb*- compared to *Hras*- or *Rfp*-recombined cells. The finding of only partial RFP reactivity in skin tumours that formed in *RosaCreER*$^{T2+}$, Sdhb$^{fl/fl}$, *Hras*$^{wt/LSLG12V}$ animals (exemplified in Figure 43) underscores this concern and would also be in line with additional clonal selection of selectively recombined cells in these neoplasias.

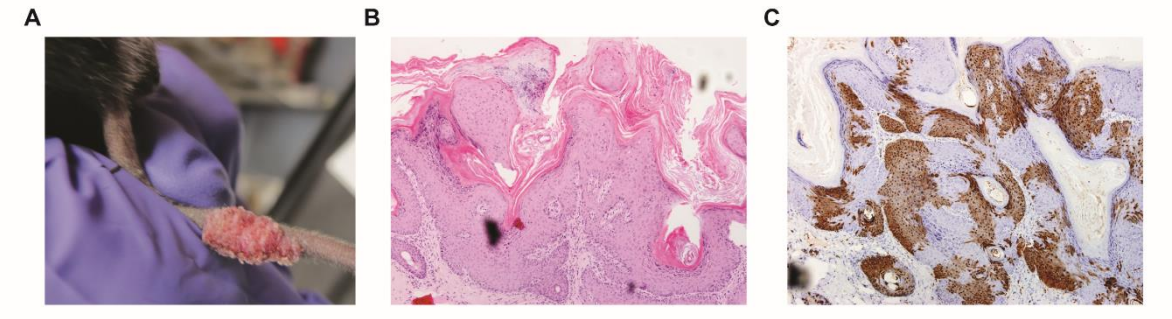

Figure 43: (A) Macroscopic morphology, (B) H&E overview and (C) RFP reactivity in a tail tumour of a *RosaCreER*$^{T2+}$, *Sdhb*$^{fl/fl}$, *Hras*$^{wt/LSLG12V}$ mouse at clinical endpoint (152 days after "high" dose transgene induction).

5.4 Summary

In chapter 5, I have discussed our investigations of a *RosaCreER*^{T2}-driven model that carries conditional *Sdhb* (*Sdhb*$^{fl/fl}$) and Hras^{G12V} (*Hras*$^{wt/LSLG12V}$) alleles. Our initial Cre activation strategy resulted in selective weight loss in *Sdhb*$^{fl/fl}$ cohorts that was paralleled by succinate accumulation and a trend towards aspartate depletion in whole blood, urine and several peripheral tissues. With the exception of progressive cachexia, no macroscopic or histological organ pathology has been identified in these mice yet. Based on recent work by other researchers (32), our current hypothesis to explain these observations thus suggests succinate itself to mediate this type of short-term toxicity.

With transgene induction schemes of lower intensity and long-term tolerability to the host, survival of cohorts was not significantly altered by *Sdhb* status in this model. However, in the *Hras*$^{wt/LSLG12V}$ background, compared to *RosaCreER*$^{T2+}$, *Sdhb*$^{wt/wt}$ animals, *RosaCreER*$^{T2+}$, *Sdhb*$^{fl/fl}$ mice developed a higher severity of skin tumours, a classical *Hras*-associated pathology in humans and mice (81, 114). Validation of this result by a topical skin carcinogenesis experiment in our *RosaCreER*^{T2} model is ongoing. In addition, increased masses of spleens and adrenals in *RosaCreER*$^{T2+}$, *Sdhb*$^{fl/fl}$, *Hras*$^{wt/LSLG12V}$ subjected to a transgene induction level of maximum long-term tolerability warrant further histological and metabolic studies of these organs.

6 Conclusions, limitations and future directions

6.1 Conclusions and limitations

The work that is presented in this thesis has been conducted in two conceptually very different genetically engineered mouse models: *KspCre*$^{+}$, *Sdhb*$^{fl/fl}$, *Hras*^{LSLG12V} animals delete *Sdhb* (exon 3) and activate an oncogenic *Hras* mutation in distal tubular epithelial cells from an early stage of development due to constitutively expressed Cre activity. In contrast, Cre can only temporarily act on the genome of some healthy, adult *RosaCreER*$^{T2+}$, *Sdhb*$^{fl/fl}$, *Hras*^{LSLG12V} cells to an extent that varies depending on transgene induction scheme as well as target gene and tissue-specific factors (please refer to section 2.1.1.2.)

Interestingly, both mouse models hint towards phenotype-augmenting interactions between the two genetic events under investigation: In our *KspCre*$^{+}$ model of SDH-deficient RCC, the additional presence of *Hras*^{LSLG12V} alleles accelerates and aggravates cystic kidney degeneration as a clearly *Sdhb* loss-initiated pathology. In turn, *Hras*^{G12V}-triggered papillomatous skin tumours in *RosaCreER*$^{T2+}$, *Hras*^{LSLG12V} mice reach higher severities as a result of SDH inactivation in conditions that do not cause clinical symptoms due to *Sdhb* loss alone. These data still need to be functionally elucidated as discussed in section 6.2.

A major disappointment during my work results from the lack of macroscopic, specifically *Sdhb* loss-related tumour formation in our models. Besides the need for other genetic events than *Hras*^{G12V} activation to enable tumourigenesis in kidneys of Cre-exposed *Sdhb*$^{fl/fl}$ mice, the early onset of strong Cre activity in distal renal tubules (or the resulting succinate accumulation) of *KspCre*$^{+}$ mice might lead to renal failure before macroscopic tumours can develop. In the *RosaCreER*$^{T2+}$ system, the recombination efficacy of both *Sdhb*^{fl} alleles in identical cells must be very low as no detectable organ changes result under experimental conditions with long-term tolerability to the host. Alternative strategies to facilitate efficient Cre activity on kidney cells without causing toxicity to other organs could potentially include kidney-specific viral Cre constructs or a *KspCreER*^{T2} system that has already been successfully applied to establish a model of clear cell-type RCC (112).

In none of our models, we could clearly attribute pathological alterations to the *Sdhb*$^{wt/fl}$ genotype. Even though SDHB protein expression in distal tubules of *Ksp Cre*$^{+}$ *Sdhb*$^{wt/fl}$, *Hras*$^{wt/wt}$ mice is quantitatively reduced in comparison to the wildtype condition (Figure 11), corresponding kidneys do not show histological or substantial metabolic differences. This is particularly disappointing as association of oncogenic *HRAS* mutations with genetic losses at the human *SDHB* locus in Pheo/PGL occurs in cases with shallow, but not bi-allelic *SDHB* deletions (50). However, until now, only biological specimens of young mice have been compared against each other and slight metabolic changes might only become apparent at later stages of observation. Therefore, it would be interesting to metabolically profile *KspCre*$^{+}$, *Sdhb*$^{wt/fl}$ against *KspCre*$^{+}$, *Sdhb*$^{wt/wt}$ kidneys and urines at old age.

The fact that both genetically engineered mouse models that I have discussed in this thesis were generated in mixed genetic backgrounds has probably introduced substantial biological variation into experimental results. Nevertheless, together with sufficiently high mouse numbers in all experiments and litter mates of different genotypes, the lack of pathologies in heterozygous animals for either *Sdhb*^{fl} or *Hras*^{LSLG12V} strongly argues against strain effects as a biological cause of detected interactions between *Sdhb* loss and *Hras* activation.

Lastly, significant sex-specific metabolic (and transcriptional) differences between the same genotype in our *KspCre*$^{+}$ model became only obvious towards the end of this thesis project. Biological samples in untargeted metabolomic investigations and the gene expression approach (please refer to section 6.2) are not perfectly balanced in this aspect. On the other hand, any potential biomarker or metabolic vulnerability of SDH-deficient tumours should ideally be valid for both male and female individuals.

6.2 Ongoing work and future directions

In spite of limitations that I have discussed in this chapter, two important open tasks hold potential to successfully complete the research that has been started within this thesis project:

Firstly, two mouse models imply a collaborative interaction between *Sdhb* deletion and activation of the oncogenic *Hras*^{G12V} mutation in the distal renal

tubular system and the skin, but a mechanistic understanding of this collaboration is still lacking. It is of course tempting to speculate about a metabolic synergy of the two events, especially as targeted analyses in *KspCre*$^{+}$, *Sdhb*$^{wt/wt}$ kidneys show a significantly higher aspartate content in the presence of *Hras*$^{LSLG12V/LSLG12V}$ (and as a trend with *Hras*$^{wt/LSLG12V}$ as well, Figure 21). Ongoing analyses of the untargeted kidney metabolomics data set (section 4.2.4) will help to address this hypothesis. Quantitative, targeted metabolomics analysis (including a succinate standard dilution curve) of (highly diluted) specimens derived from the *KspCre*$^{+}$ model will help to clarify if the current observation of similar succinate urine and kidney tissue levels in all Sdhb$^{fl/fl}$ cohorts despite substantial differences in phenotypic severity is caused by saturation of the detection system or a biological reality.

To address a potential *Sdhb* loss-*Hras*^{G12V} interaction on a transcriptional level in an unbiased way, I have recently subjected a set of whole *KspCre*$^{+}$ kidneys to RNA sequencing (Figure 44). In order to reach biologically meaningful conclusions from the resulting data, it is crucial to consider that they have been generated from whole organ extracts. More specifically, detection of different transcript levels can correspond to either altered expression in a defined compound of kidney tissue or changes in relative abundance of this structure. In the *KspCre* model for example, in contrast to expectations towards SDH-deficient tissues (66), the *Pcx* gene transcript (encoding pyruvate carboxylase) is detected at lower levels in *Sdhb*$^{fl/fl}$ than in *Sdhb*$^{wt/wt}$ samples. This could be explained by reduced expression in distal tubular cells due to *Sdhb* loss, but alternatively by an expansion of distal relative to proximal tubular and interstitial structures and generally lower *Pcx* expression in distal tubular cells, but without transcriptional changes in each compartment of these kidneys occurring due to alteration of *Sdhb*.

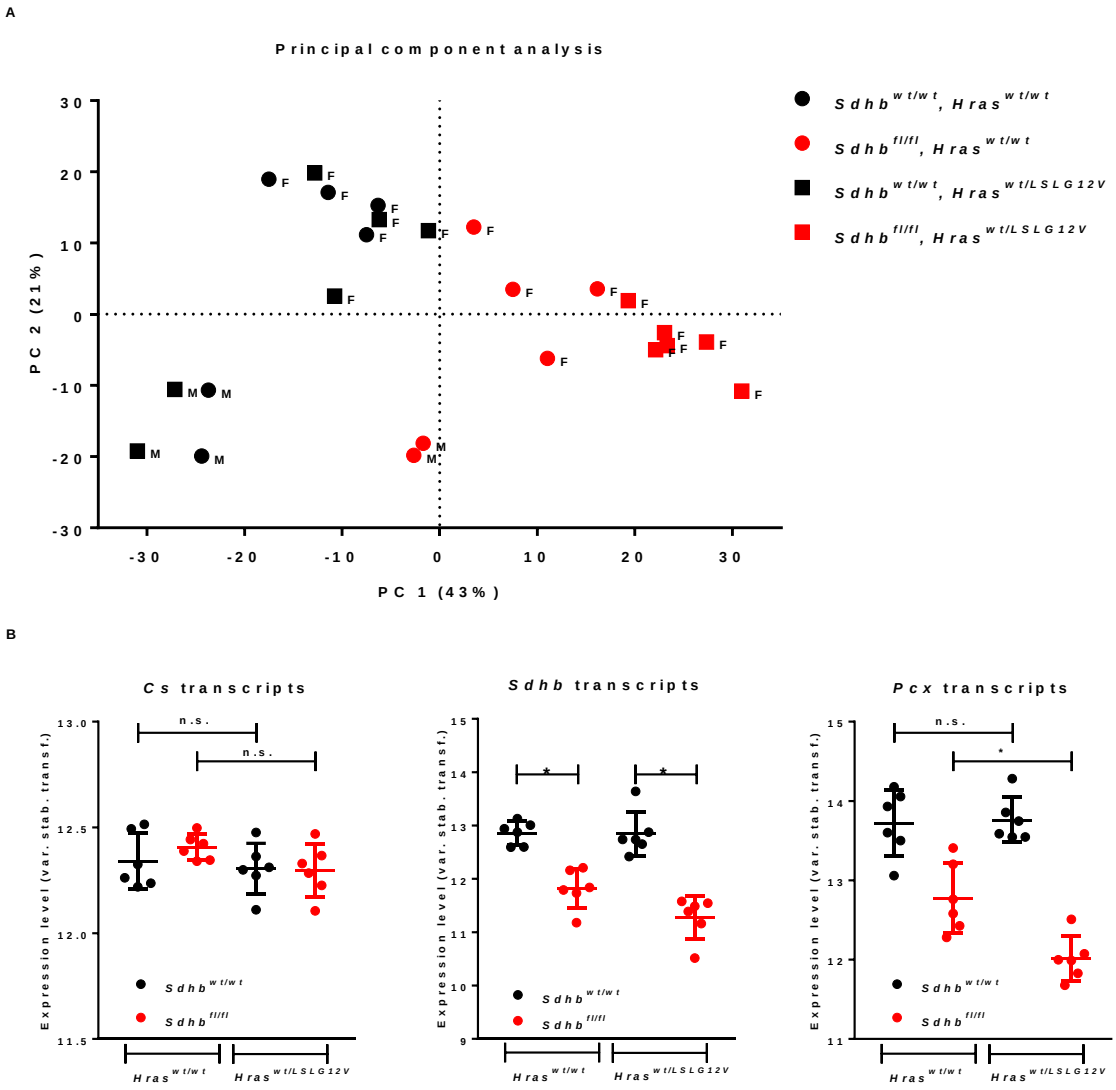

Figure 44: Overview of RNA sequencing data obtained from *KspCre*$^{+}$ kidneys at young age. (A) First Principal component analysis. (B) Transcript levels (variance stabilising transformed values) of *citrate synthase* (*Cs*, left) *Sdhb* (centre) and Pcx (right). Of note, PC1 separates *Sdhb*$^{fl/fl}$ from *Sdhb*$^{wt/wt}$ samples and further sub-stratifies *Sdhb*$^{fl/fl}$ (but not *Sdhb*$^{wt/wt}$) kidneys according to *Hras* status. PC2 reflects sex-specific transcriptional differences. PC3 does not improve separation between genetic groups (not shown). F, female; M, male.

Together with similar mRNA expression values for the mitochondrial marker transcript citrate synthase (encoded by the *Cs* gene) in all genotypes, significantly lower *Sdhb* transcript levels in *Sdhb*$^{fl/fl}$, *Hras*$^{wt/wt}$ and *Sdhb*$^{fl/fl}$, *Hras*$^{wt/LSLG12V}$ whole kidney extracts compared to *Sdhb*$^{wt/wt}$ controls underscore profound global transcriptional differences depending on SDHB status. As any functional validation attempts, an in-depth analysis of this data set will have to be completed after final submission of my thesis. I find it still worthwhile mentioning here that a first pathway enrichment analysis comparing *Sdhb*$^{fl/fl}$, *Hras*$^{wt/wt}$ to *Sdhb*$^{wt/wt}$, *Hras*$^{wt/wt}$ cases has pointed towards induction of Mitogen-activated protein kinase (MAPK)

signalling by the mere loss of *Sdhb* (Figure 45A). Importantly, a classical gene set enrichment analysis also confirmed higher transcriptional MAPK kinase pathway activity in the *Sdhb*$^{fl/fl}$, *Hras*$^{wt/LSLG12V}$ group compared to *Sdhb*$^{wt/wt}$, *Hras*$^{wt/LSLG12V}$ kidneys (Figure 45B), arguing for transcriptionally higher MAPK pathway levels in SDH-deficient distal tubular cells even when compared against SDH-proficient specimens in the presence of oncogenic *Hras*. I am very excited by this preliminary finding (that still needs further experimental investigation) as it points towards a common biological downstream effect of *Hras* mutation and *Sdhb* deletion and might thereby explain the observed interaction between the two genetic events in our RCC model.

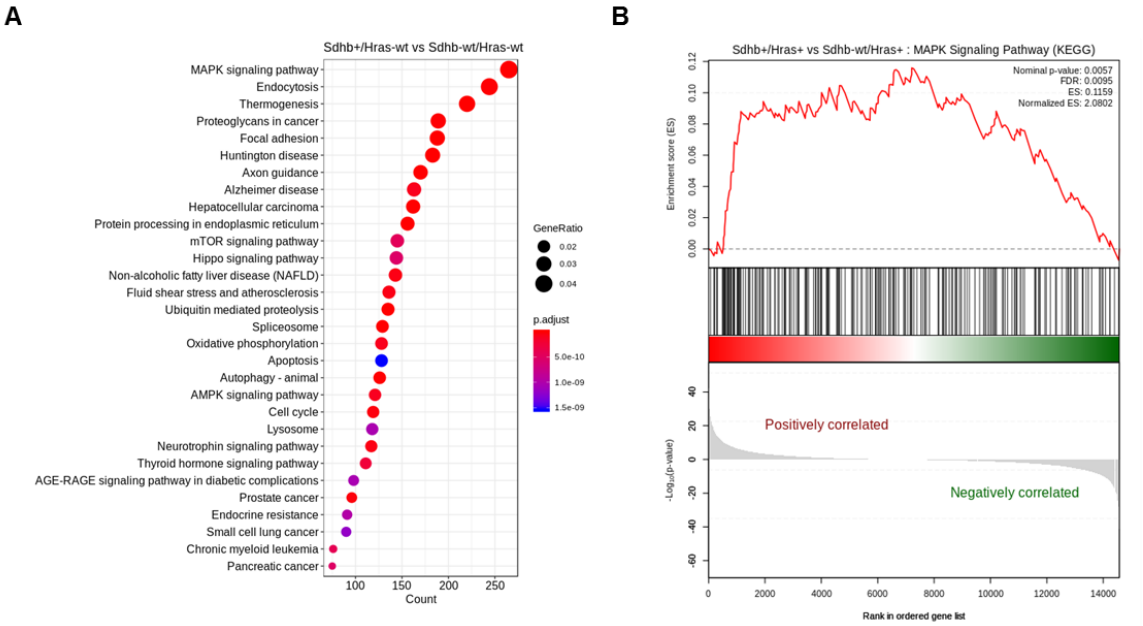

Figure 45: Transcriptional induction of MAPK (Mitogen-activated protein kinase) signalling pathway in *KspCre*$^{+}$, *Sdhb*$^{fl/fl}$ kidneys. (A) Pathway enrichment analyses for KEGG (Kyoto Encyclopedia of Genes and Genomes) terms comparing *Sdhb*$^{fl/fl}$, *Hras*$^{wt/wt}$ kidneys to *Sdhb*$^{fl/fl}$, *Hras*$^{wt/wt}$ controls. (B) Gene set enrichment for the KEGG term "MAPK signalling" in *Sdhb*$^{fl/fl}$, *Hras*$^{wt/LSLG12V}$ relative to *Sdhb*$^{wtl/wt}$, *Hras*$^{wt/LSLG12V}$ kidneys. All analyses were performed by Jonatan Fernandez-Garcia at the Technion, Haifa, Israel.

A comprehensive interpretation of the three untargeted metabolomics experiments conducted in the kidney-specific *Sdhb* knockout model (chapter 4) constitutes the second line of analyses that still have to be undertaken. Development of experimental workflows and methodology at the CRUK Beatson Institute has been an elaborate and ongoing learning process over the last years with reliable assignment of metabolite identities to compounds of interest, a limiting step that is typically encountered in untargeted metabolomics approaches (116), remaining a challenge. The concordance of *Sdhb* loss-related alterations

(such as succinate accumulation and aspartate depletion) with metabolic changes that are caused by progressive excretory renal insufficiency (*e.g.* increased local and systemic creatinine abundancies) in the *KspCre*$^{+}$-based genetically engineered mouse model introduces an additional, biological confounder. However, validation of potential "hit" candidates by longitudinal analyses for individual *KspCre*$^{+}$ mice and in other biological settings such as the *RosaCreER*^{T2} model (for both of which an extensive number of specimens has been acquired already) will hopefully allow a metabolic separation of *Sdhb* deficiency from renal failure.

Moreover, after ethics approval of our research application to the National GIST Biobank, we have recently obtained a set of 32 fresh-frozen gastrointestinal stroma tumour (GIST) tissue samples. 10 of these cases had been identified as "SDH-deficient" by (molecular) pathological evaluation, whilst all remaining 22 specimens carried mutation in the *cKIT* or *PDGFR*α genes, *i.e.* one of the two most frequent driver mutations in GIST (117). This independent set of samples has given us the option to test our mouse model-derived metabolic results for transferability to a different SDH loss-related cancer entity in humans.

Initially, all specimens were subjected to the identical untargeted metabolomics approach as our *KspCre*$^{+}$ model-derived samples. A first unbiased data evaluation (by principal component analysis) demonstrated a dramatic metabolic alteration of samples that had been accidentally thawed during processing at the Biobank irrespective of underlying genetic driver mutation (Figure 46A). Furthermore, two of the SDH-deficient tumour tissues displayed an extremely fibrotic morphology that prevented adequate cryogrinding and resulted in significant metabolic deviations from other SDH-deficient cases. Based on these observations, thawed and inadequately grinded samples were excluded from further analyses. Comparing the eight representative SDH-deficient tumours against all adequately handled SDH-proficient specimens demonstrated expected differences in both succinate and aspartate abundancies (Figure 46B,C) between the groups, even though three SDH-deficient samples only showed a modest degree of succinate accumulation (Figure 46B). Similarly decreased aspartate abundancies in all SDH-deficient tumours and a lack of correction of the succinate level difference by repeating all analytical steps from extraction as well as applying an additional internal normalisation step (constant sum approach, not shown) could argue for a

biological difference within the SDH-deficient sample group. Nevertheless, technical/pre-analytical problems cannot be excluded as potential reasons for this observation and it will thus be interesting to correlate individual succinate abundancies with underlying SDH subunit mutations and, if possible, to repeat the metabolic analysis in an independent set of SDH-deficient GIST samples.

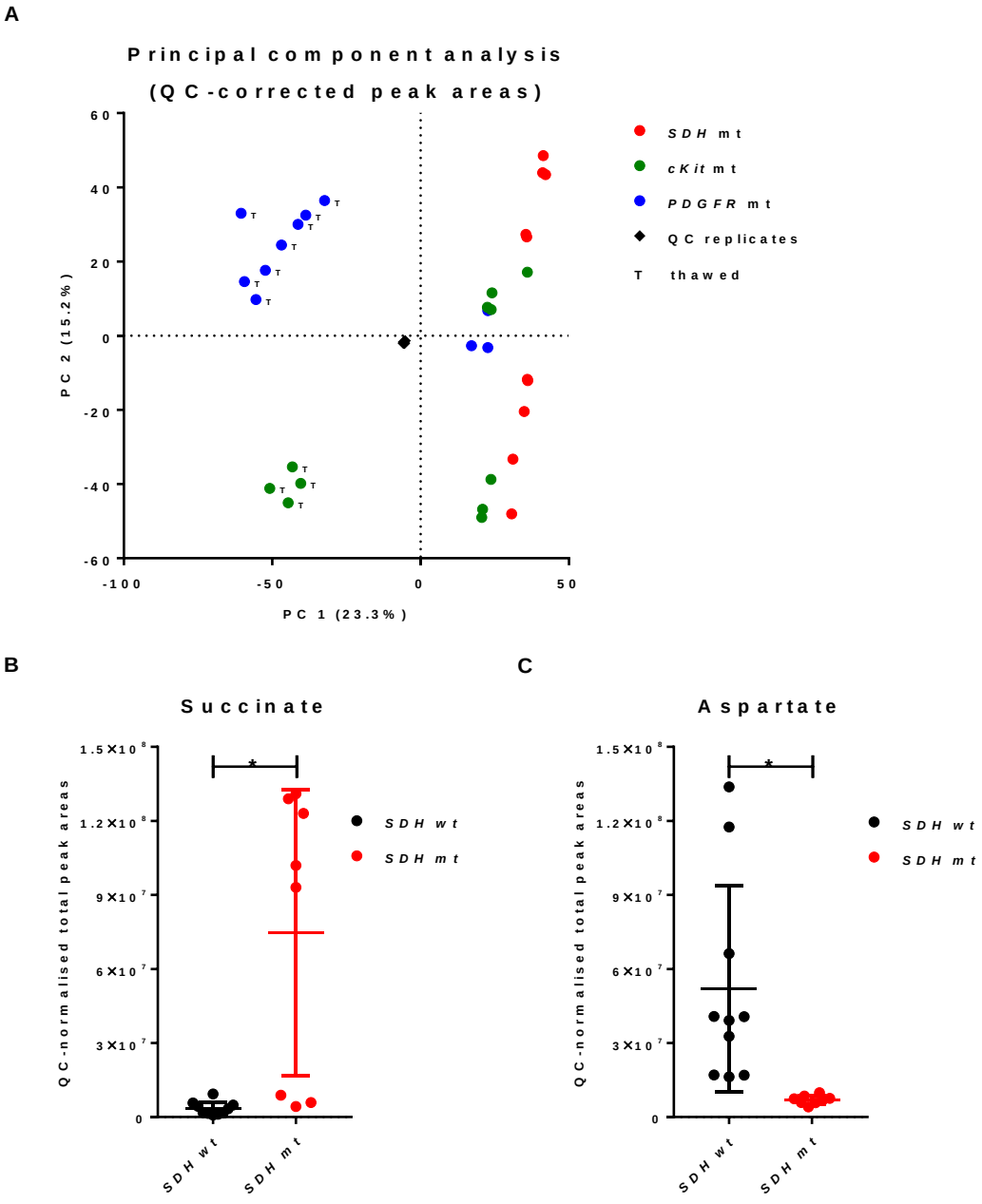

Figure 46: Succinate accumulation and aspartate depletion are typical features of human SDH-deficient GIST tissues. (A) PCA (PC1 and PC2, all detected and quality control [QC]-corrected peak areas) of an untargeted metabolomics experiment in a set of human GIST samples. Abundancies of succinate (B) and aspartate (C) as measured by LC-MS in SDH-deficient and SDH-proficient (i.e. cKIT-mutated combined with PDGFRα-mutated) tumours after exclusion of thawed ("T") samples and two additional fibrotic tissue samples. "*", $p<0.05$.

So far, despite the varying degrees of succinate accumulation discussed above, all eight sufficiently processed SDH-deficient GIST cases have been included in subsequent attempts to recapitulate potential metabolic biomarker candidates obtained in our *KspCre+* model in this primary human tumour data set. Assuming production of a biomarker by SDH-deficient (tumour) cells and consequently increased abundancy in the body fluid of interest in young *KspCre*$^{+}$, *Sdhb*$^{fl/fl}$, *Hras*$^{wt/LSLG12V}$ mice, a first analysis has resulted in five potential biomarker candidates, amongst them, as expected, succinate (together with the closely related metabolite succinic anhydride) (Table 16). Identities of candidates A, B and E are subject to current investigations.

Hit no.	Candidate biomarker type	Change kidneys Sdhb$^{fl/fl}$/Sdhb$^{wt/wt}$	Change plasma Sdhb$^{fl/fl}$/Sdhb$^{wt/wt}$	Change urine Sdhb$^{fl/fl}$/Sdhb$^{wt/wt}$	Change GIST SDH def./SDH wt	Molecular weight [g/mol]	RT [min]	Suggested identities
A	plasma	up	up	any	up	120.04249	6.763	Purine?, (S)-3,4-Dihydroxybutyric acid?
B	plasma	up	up	any	up	143.09459	7.292	DL-Stachydrine?
C	urine	up	any	up	up	100.01616	13.041	Succinic anhydride?
D	urine	up	any	up	up	118.02698	13.037	Succinate
E	urine	up	any	up	up	186.0641	5.273	AMPA?, Pyroglutamylglycine?

Table 16: Potential plasma- and urine biomarkers of SDH deficiency. Expected change patterns compared to SDH-proficient controls, molecular weight, retention times and potential metabolite identities that have been suggested by automated annotation algorithms are depicted. In addition to elevated abundancies in *KspCre*$^{+}$, *Sdhb*$^{fl/fl}$, *Hras*$^{wt/LSLG12V}$ kidneys as well as SDH-deficient GIST samples, increased levels of a corresponding compound in *KspCre*$^{+}$, *Sdhb*$^{fl/fl}$, *Hras*$^{wt/LSLG12V}$ plasma or urine samples compared to *Sdhb*$^{wt/wt}$ controls were expected for plasma/urine biomarker candidates.

After correlation of individual succinate abundancies with SDH subunit mutations in our GIST sample set as outlined above, future work will focus on comparisons of mouse model-derived metabolomics results against alterations selectively occurring in the group of five GIST samples that display highest succinate accumulation, *i.e.* a typical metabolic profile of SDH-deficiency in order to increase the number of biomarker candidates for future validation studies.

Appendices

Appendix 1: Publications

Mills EL, Kelly B, Logan A, Costa ASH, Varma M, Bryant CE, Tourlomousis P, **Däbritz JHM**, Gottlieb E, Latorre I, Corr SC, McManus G, Ryan D, Jacobs HT, Szibor M, Xavier RJ, Braun T, Frezza C, Murphy MP, O'Neill LA (2016). Succinate Dehydrogenase Supports Metabolic Repurposing of Mitochondria to Drive Inflammatory Macrophages. Cell 167(2):457-470.
https://doi.org/10.1016/j.cell.2016.08.064

Olivares O*, **Däbritz JHM***, King A, Gottlieb E, Halsey C (2015). Research into cancer metabolomics: Towards a clinical metamorphosis. Semin Cell Dev Biol. 43:52-64. (Review) *equal contribution
https://doi.org/10.1016/j.semcdb.2015.09.008

List of References

1. Boycott KM, Rath A, Chong JX, Hartley T, Alkuraya FS, Baynam G, et al. International Cooperation to Enable the Diagnosis of All Rare Genetic Diseases. *Am J Hum Genet*. 2017;100(5):695-705.
2. Vrueh R, Baekelandt E, and de Haan J. Background paper 6.19 rare diseases: update on 2004 background paper written by S. van Weely and H.G.M. Leufkens. http://who.int/medicines/areas/priority_medicines/BP6_19Rare.pdf. Updated 2013 Accessed 05/01/2019.
3. Knudson AG, Jr. Mutation and cancer: statistical study of retinoblastoma. *Proceedings of the National Academy of Sciences of the United States of America*. 1971;68(4):820-3.
4. Hall JM, Lee MK, Newman B, Morrow JE, Anderson LA, Huey B, et al. Linkage of early-onset familial breast cancer to chromosome 17q21. *Science*. 1990;250(4988):1684-9.
5. Warburg O, and Minami S. Versuche an überlebendem Carcinomgewebe. *Klinische Wochenschrift*. 1923;2(17):2.
6. Warburg O. On the origin of cancer cells. *Science*. 1956;123(3191):309-14.
7. Vander Heiden MG, and DeBerardinis RJ. Understanding the Intersections between Metabolism and Cancer Biology. *Cell*. 2017;168(4):657-69.
8. Olivares O, Dabritz JH, King A, Gottlieb E, and Halsey C. Research into cancer metabolomics: Towards a clinical metamorphosis. *Seminars in cell & developmental biology*. 2015.
9. DiNardo CD, Stein EM, de Botton S, Roboz GJ, Altman JK, Mims AS, et al. Durable Remissions with Ivosidenib in IDH1-Mutated Relapsed or Refractory AML. *N Engl J Med*. 2018;378(25):2386-98.
10. Stein EM, DiNardo CD, Pollyea DA, Fathi AT, Roboz GJ, Altman JK, et al. Enasidenib in mutant IDH2 relapsed or refractory acute myeloid leukemia. *Blood*. 2017;130(6):722-31.
11. Rasheed M, and Tarjan G. Succinate Dehydrogenase Complex: An Updated Review. *Arch Pathol Lab Med*. 2018;142(12):1564-70.
12. Bardella C, Pollard PJ, and Tomlinson I. SDH mutations in cancer. *Biochimica et biophysica acta*. 2011;1807(11):1432-43.
13. Krebs HA. The history of the tricarboxylic acid cycle. *Perspect Biol Med*. 1970;14(1):154-70.
14. Folbergrova J, Ljunggren B, Norberg K, and Siesjo BK. Influence of complete ischemia on glycolytic metabolites, citric acid cycle intermediates, and associated amino acids in the rat cerebral cortex. *Brain Res*. 1974;80(2):265-79.
15. Taegtmeyer H. Metabolic responses to cardiac hypoxia. Increased production of succinate by rabbit papillary muscles. *Circ Res*. 1978;43(5):808-15.
16. Wittenberger T, Schaller HC, and Hellebrand S. An expressed sequence tag (EST) data mining strategy succeeding in the discovery of new G-protein coupled receptors. *J Mol Biol*. 2001;307(3):799-813.
17. He W, Miao FJ, Lin DC, Schwandner RT, Wang Z, Gao J, et al. Citric acid cycle intermediates as ligands for orphan G-protein-coupled receptors. *Nature*. 2004;429(6988):188-93.
18. Rubic T, Lametschwandtner G, Jost S, Hinteregger S, Kund J, Carballido-Perrig N, et al. Triggering the succinate receptor GPR91 on dendritic cells enhances immunity. *Nat Immunol*. 2008;9(11):1261-9.

19. Hakak Y, Lehmann-Bruinsma K, Phillips S, Le T, Liaw C, Connolly DT, et al. The role of the GPR91 ligand succinate in hematopoiesis. *J Leukoc Biol*. 2009;85(5):837-43.
20. Tannahill GM, Curtis AM, Adamik J, Palsson-McDermott EM, McGettrick AF, Goel G, et al. Succinate is an inflammatory signal that induces IL-1beta through HIF-1alpha. *Nature*. 2013;496(7444):238-42.
21. Diehl J, Gries B, Pfeil U, Goldenberg A, Mermer P, Kummer W, et al. Expression and localization of GPR91 and GPR99 in murine organs. *Cell Tissue Res*. 2016;364(2):245-62.
22. Toma I, Kang JJ, Sipos A, Vargas S, Bansal E, Hanner F, et al. Succinate receptor GPR91 provides a direct link between high glucose levels and renin release in murine and rabbit kidney. *The Journal of clinical investigation*. 2008;118(7):2526-34.
23. Peti-Peterdi J. High glucose and renin release: the role of succinate and GPR91. *Kidney Int*. 2010;78(12):1214-7.
24. Vargas SL, Toma I, Kang JJ, Meer EJ, and Peti-Peterdi J. Activation of the succinate receptor GPR91 in macula densa cells causes renin release. *Journal of the American Society of Nephrology : JASN*. 2009;20(5):1002-11.
25. Sapieha P, Sirinyan M, Hamel D, Zaniolo K, Joyal JS, Cho JH, et al. The succinate receptor GPR91 in neurons has a major role in retinal angiogenesis. *Nat Med*. 2008;14(10):1067-76.
26. Ko SH, Choi GE, Oh JY, Lee HJ, Kim JS, Chae CW, et al. Succinate promotes stem cell migration through the GPR91-dependent regulation of DRP1-mediated mitochondrial fission. *Sci Rep*. 2017;7(1):12582.
27. Chouchani ET, Pell VR, Gaude E, Aksentijevic D, Sundier SY, Robb EL, et al. Ischaemic accumulation of succinate controls reperfusion injury through mitochondrial ROS. *Nature*. 2014;515(7527):431-5.
28. Kohlhauer M, Dawkins S, Costa ASH, Lee R, Young T, Pell VR, et al. Metabolomic Profiling in Acute ST-Segment-Elevation Myocardial Infarction Identifies Succinate as an Early Marker of Human Ischemia-Reperfusion Injury. *J Am Heart Assoc*. 2018;7(8).
29. Mills EL, Kelly B, Logan A, Costa ASH, Varma M, Bryant CE, et al. Succinate Dehydrogenase Supports Metabolic Repurposing of Mitochondria to Drive Inflammatory Macrophages. *Cell*. 2016;167(2):457-70 e13.
30. Regard JB, Sato IT, and Coughlin SR. Anatomical profiling of G protein-coupled receptor expression. *Cell*. 2008;135(3):561-71.
31. McCreath KJ, Espada S, Galvez BG, Benito M, de Molina A, Sepulveda P, et al. Targeted disruption of the SUCNR1 metabolic receptor leads to dichotomous effects on obesity. *Diabetes*. 2015;64(4):1154-67.
32. Mills EL, Pierce KA, Jedrychowski MP, Garrity R, Winther S, Vidoni S, et al. Accumulation of succinate controls activation of adipose tissue thermogenesis. *Nature*. 2018;560(7716):102-6.
33. National Library of Medicine (US). Genetics Home Reference [Internet]. Leigh syndrome. https://ghr.nlm.nih.gov/condition/leigh-syndrome Updated June 2016 Accessed 11/12/2018.
34. Bourgeron T, Rustin P, Chretien D, Birch-Machin M, Bourgeois M, Viegas-Pequignot E, et al. Mutation of a nuclear succinate dehydrogenase gene results in mitochondrial respiratory chain deficiency. *Nat Genet*. 1995;11(2):144-9.
35. Jones R, McDonald KE, Willson JA, Ghesquiere B, Sammut D, Daniel E, et al. Mutations in succinate dehydrogenase B (SDHB) enhance neutrophil survival independent of HIF-1alpha expression. *Blood*. 2016;127(21):2641-4.

36. Baysal BE, Ferrell RE, Willett-Brozick JE, Lawrence EC, Myssiorek D, Bosch A, et al. Mutations in SDHD, a mitochondrial complex II gene, in hereditary paraganglioma. *Science*. 2000;287(5454):848-51.
37. Niemann S, and Muller U. Mutations in SDHC cause autosomal dominant paraganglioma, type 3. *Nat Genet*. 2000;26(3):268-70.
38. Astuti D, Latif F, Dallol A, Dahia PL, Douglas F, George E, et al. Gene mutations in the succinate dehydrogenase subunit SDHB cause susceptibility to familial pheochromocytoma and to familial paraganglioma. *Am J Hum Genet*. 2001;69(1):49-54.
39. Gill AJ, Hes O, Papathomas T, Sedivcova M, Tan PH, Agaimy A, et al. Succinate dehydrogenase (SDH)-deficient renal carcinoma: a morphologically distinct entity: a clinicopathologic series of 36 tumors from 27 patients. *Am J Surg Pathol*. 2014;38(12):1588-602.
40. Janeway KA, Kim SY, Lodish M, Nose V, Rustin P, Gaal J, et al. Defects in succinate dehydrogenase in gastrointestinal stromal tumors lacking KIT and PDGFRA mutations. *Proceedings of the National Academy of Sciences of the United States of America*. 2011;108(1):314-8.
41. Niemeijer ND, Papathomas TG, Korpershoek E, de Krijger RR, Oudijk L, Morreau H, et al. Succinate Dehydrogenase (SDH)-Deficient Pancreatic Neuroendocrine Tumor Expands the SDH-Related Tumor Spectrum. *J Clin Endocrinol Metab*. 2015;100(10):E1386-93.
42. Burnichon N, Briere JJ, Libe R, Vescovo L, Riviere J, Tissier F, et al. SDHA is a tumor suppressor gene causing paraganglioma. *Human molecular genetics*. 2010;19(15):3011-20.
43. Bayley JP, Kunst HP, Cascon A, Sampietro ML, Gaal J, Korpershoek E, et al. SDHAF2 mutations in familial and sporadic paraganglioma and phaeochromocytoma. *Lancet Oncol*. 2010;11(4):366-72.
44. Killian JK, Miettinen M, Walker RL, Wang Y, Zhu YJ, Waterfall JJ, et al. Recurrent epimutation of SDHC in gastrointestinal stromal tumors. *Science translational medicine*. 2014;6(268):268ra177.
45. Weinhold N, Jacobsen A, Schultz N, Sander C, and Lee W. Genome-wide analysis of noncoding regulatory mutations in cancer. *Nat Genet*. 2014;46(11):1160-5.
46. Gaude E, and Frezza C. Tissue-specific and convergent metabolic transformation of cancer correlates with metastatic potential and patient survival. *Nat Commun*. 2016;7:13041.
47. Reznik E, Wang Q, La K, Schultz N, and Sander C. Mitochondrial respiratory gene expression is suppressed in many cancers. *Elife*. 2017;6.
48. Castro-Vega LJ, Letouze E, Burnichon N, Buffet A, Disderot PH, Khalifa E, et al. Multi-omics analysis defines core genomic alterations in pheochromocytomas and paragangliomas. *Nat Commun*. 2015;6:6044.
49. Crona J, Delgado Verdugo A, Maharjan R, Stalberg P, Granberg D, Hellman P, et al. Somatic mutations in H-RAS in sporadic pheochromocytoma and paraganglioma identified by exome sequencing. *J Clin Endocrinol Metab*. 2013;98(7):E1266-71.
50. Fishbein L, Leshchiner I, Walter V, Danilova L, Robertson AG, Johnson AR, et al. Comprehensive Molecular Characterization of Pheochromocytoma and Paraganglioma. *Cancer Cell*. 2017;31(2):181-93.
51. Cerami E, Gao J, Dogrusoz U, Gross BE, Sumer SO, Aksoy BA, et al. The cBio cancer genomics portal: an open platform for exploring multidimensional cancer genomics data. *Cancer Discov*. 2012;2(5):401-4.

52. Gao J, Aksoy BA, Dogrusoz U, Dresdner G, Gross B, Sumer SO, et al. Integrative analysis of complex cancer genomics and clinical profiles using the cBioPortal. *Sci Signal*. 2013;6(269):pl1.
53. Linehan WM, Srinivasan R, and Schmidt LS. The genetic basis of kidney cancer: a metabolic disease. *Nat Rev Urol*. 2010;7(5):277-85.
54. Moch H, Cubilla AL, Humphrey PA, Reuter VE, and Ulbright TM. The 2016 WHO Classification of Tumours of the Urinary System and Male Genital Organs-Part A: Renal, Penile, and Testicular Tumours. *Eur Urol*. 2016.
55. Young MD, Mitchell TJ, Vieira Braga FA, Tran MGB, Stewart BJ, Ferdinand JR, et al. Single-cell transcriptomes from human kidneys reveal the cellular identity of renal tumors. *Science*. 2018;361(6402):594-9.
56. Ngo TC, Wood CG, and Karam JA. Biomarkers of renal cell carcinoma. *Urol Oncol*. 2014;32(3):243-51.
57. Williamson SR, Eble JN, Amin MB, Gupta NS, Smith SC, Sholl LM, et al. Succinate dehydrogenase-deficient renal cell carcinoma: detailed characterization of 11 tumors defining a unique subtype of renal cell carcinoma. *Mod Pathol*. 2015;28(1):80-94.
58. Wang G, and Rao P. Succinate Dehydrogenase-Deficient Renal Cell Carcinoma: A Short Review. *Arch Pathol Lab Med*. 2018;142(10):1284-8.
59. Kumar R, Bonert M, Naqvi A, Zbuk K, and Kapoor A. SDH-deficient renal cell carcinoma - clinical, pathologic and genetic correlates: a case report. *BMC Urol*. 2018;18(1):109.
60. Agaimy A. [Succinate dehydrogenase (SDH)-deficient renal cell carcinoma]. *Pathologe*. 2016;37(2):144-52.
61. Selak MA, Armour SM, MacKenzie ED, Boulahbel H, Watson DG, Mansfield KD, et al. Succinate links TCA cycle dysfunction to oncogenesis by inhibiting HIF-alpha prolyl hydroxylase. *Cancer Cell*. 2005;7(1):77-85.
62. Letouze E, Martinelli C, Loriot C, Burnichon N, Abermil N, Ottolenghi C, et al. SDH mutations establish a hypermethylator phenotype in paraganglioma. *Cancer Cell*. 2013;23(6):739-52.
63. Nowicki S, and Gottlieb E. Oncometabolites: Tailoring our Genes. *FEBS J*. 2015.
64. Sulkowski PL, Sundaram RK, Oeck S, Corso CD, Liu Y, Noorbakhsh S, et al. Krebs-cycle-deficient hereditary cancer syndromes are defined by defects in homologous-recombination DNA repair. *Nat Genet*. 2018;50(8):1086-92.
65. Gilissen J, Jouret F, Pirotte B, and Hanson J. Insight into SUCNR1 (GPR91) structure and function. *Pharmacol Ther*. 2016;159:56-65.
66. Cardaci S, Zheng L, MacKay G, van den Broek NJ, MacKenzie ED, Nixon C, et al. Pyruvate carboxylation enables growth of SDH-deficient cells by supporting aspartate biosynthesis. *Nat Cell Biol*. 2015;17(10):1317-26.
67. Birsoy K, Wang T, Chen WW, Freinkman E, Abu-Remaileh M, and Sabatini DM. An Essential Role of the Mitochondrial Electron Transport Chain in Cell Proliferation Is to Enable Aspartate Synthesis. *Cell*. 2015;162(3):540-51.
68. Sullivan LB, Gui DY, Hosios AM, Bush LN, Freinkman E, and Vander Heiden MG. Supporting Aspartate Biosynthesis Is an Essential Function of Respiration in Proliferating Cells. *Cell*. 2015;162(3):552-63.
69. Garcia-Bermudez J, Baudrier L, La K, Zhu XG, Fidelin J, Sviderskiy VO, et al. Aspartate is a limiting metabolite for cancer cell proliferation under hypoxia and in tumours. *Nat Cell Biol*. 2018;20(7):775-81.
70. Bender RH, Haigis KM, and Gutmann DH. Activated k-ras, but not h-ras or N-ras, regulates brain neural stem cell proliferation in a raf/rb-dependent manner. *Stem Cells*. 2015;33(6):1998-2010.

71. Aoki Y, Niihori T, Kawame H, Kurosawa K, Ohashi H, Tanaka Y, et al. Germline mutations in HRAS proto-oncogene cause Costello syndrome. *Nature genetics*. 2005;37(10):1038-40.
72. Leoni C, Onesimo R, Giorgio V, Diamanti A, Giorgio D, Martini L, et al. Understanding Growth Failure in Costello Syndrome: Increased Resting Energy Expenditure. *J Pediatr*. 2016;170:322-4.
73. Dard L, Bellance N, Lacombe D, and Rossignol R. RAS signalling in energy metabolism and rare human diseases. *Biochim Biophys Acta Bioenerg*. 2018;1859(9):845-67.
74. Hobbs GA, Der CJ, and Rossman KL. RAS isoforms and mutations in cancer at a glance. *J Cell Sci*. 2016;129(7):1287-92.
75. Karnoub AE, and Weinberg RA. Ras oncogenes: split personalities. *Nat Rev Mol Cell Biol*. 2008;9(7):517-31.
76. Serrano M, Lin AW, McCurrach ME, Beach D, and Lowe SW. Oncogenic ras provokes premature cell senescence associated with accumulation of p53 and p16INK4a. *Cell*. 1997;88(5):593-602.
77. Braig M, Lee S, Loddenkemper C, Rudolph C, Peters AH, Schlegelberger B, et al. Oncogene-induced senescence as an initial barrier in lymphoma development. *Nature*. 2005;436(7051):660-5.
78. Chen X, Makarewicz JM, Knauf JA, Johnson LK, and Fagin JA. Transformation by Hras(G12V) is consistently associated with mutant allele copy gains and is reversed by farnesyl transferase inhibition. *Oncogene*. 2014;33(47):5442-9.
79. Burgess MR, Hwang E, Mroue R, Bielski CM, Wandler AM, Huang BJ, et al. KRAS Allelic Imbalance Enhances Fitness and Modulates MAP Kinase Dependence in Cancer. *Cell*. 2017;168(5):817-29 e15.
80. Kerr EM, Gaude E, Turrell FK, Frezza C, and Martins CP. Mutant Kras copy number defines metabolic reprogramming and therapeutic susceptibilities. *Nature*. 2016;531(7592):110-3.
81. Bremner R, and Balmain A. Genetic changes in skin tumor progression: correlation between presence of a mutant ras gene and loss of heterozygosity on mouse chromosome 7. *Cell*. 1990;61(3):407-17.
82. Piruat JI, and Millan-Ucles A. Genetically modeled mice with mutations in mitochondrial metabolic enzymes for the study of cancer. *Front Oncol*. 2014;4:200.
83. Ramirez-Solis R, Liu P, and Bradley A. Chromosome engineering in mice. *Nature*. 1995;378(6558):720-4.
84. Gu H, Marth JD, Orban PC, Mossmann H, and Rajewsky K. Deletion of a DNA polymerase beta gene segment in T cells using cell type-specific gene targeting. *Science*. 1994;265(5168):103-6.
85. Rajewsky K, Gu H, Kuhn R, Betz UA, Muller W, Roes J, et al. Conditional gene targeting. *The Journal of clinical investigation*. 1996;98(3):600-3.
86. Feil R. Conditional somatic mutagenesis in the mouse using site-specific recombinases. *Handb Exp Pharmacol*. 2007(178):3-28.
87. Brault V, Besson V, Magnol L, Duchon A, and Herault Y. Cre/loxP-mediated chromosome engineering of the mouse genome. *Handb Exp Pharmacol*. 2007(178):29-48.
88. Feil S, Valtcheva N, and Feil R. Inducible Cre mice. *Methods Mol Biol*. 2009;530:343-63.
89. Shao X, Somlo S, and Igarashi P. Epithelial-specific Cre/lox recombination in the developing kidney and genitourinary tract. *Journal of the American Society of Nephrology : JASN*. 2002;13(7):1837-46.

90. Hameyer D, Loonstra A, Eshkind L, Schmitt S, Antunes C, Groen A, et al. Toxicity of ligand-dependent Cre recombinases and generation of a conditional Cre deleter mouse allowing mosaic recombination in peripheral tissues. *Physiol Genomics*. 2007;31(1):32-41.
91. Luche H, Weber O, Nageswara Rao T, Blum C, and Fehling HJ. Faithful activation of an extra-bright red fluorescent protein in "knock-in" Cre-reporter mice ideally suited for lineage tracing studies. *Eur J Immunol*. 2007;37(1):43-53.
92. Irion S, Luche H, Gadue P, Fehling HJ, Kennedy M, and Keller G. Identification and targeting of the ROSA26 locus in human embryonic stem cells. *Nat Biotechnol*. 2007;25(12):1477-82.
93. Friedrich G, and Soriano P. Promoter traps in embryonic stem cells: a genetic screen to identify and mutate developmental genes in mice. *Genes Dev*. 1991;5(9):1513-23.
94. Vooijs M, Jonkers J, and Berns A. A highly efficient ligand-regulated Cre recombinase mouse line shows that LoxP recombination is position dependent. *EMBO Rep*. 2001;2(4):292-7.
95. Seibler J, Zevnik B, Kuter-Luks B, Andreas S, Kern H, Hennek T, et al. Rapid generation of inducible mouse mutants. *Nucleic acids research*. 2003;31(4):e12.
96. Esteban LM, Vicario-Abejon C, Fernandez-Salguero P, Fernandez-Medarde A, Swaminathan N, Yienger K, et al. Targeted genomic disruption of H-ras and N-ras, individually or in combination, reveals the dispensability of both loci for mouse growth and development. *Mol Cell Biol*. 2001;21(5):1444-52.
97. Fisher S, Barry A, Abreu J, Minie B, Nolan J, Delorey TM, et al. A scalable, fully automated process for construction of sequence-ready human exome targeted capture libraries. *Genome Biol*. 2011;12(1):R1.
98. Andrews S. FastQC A Quality Control tool for High Throughput Sequence Data. *http://wwwbioinformaticsbabrahamacuk/projects/fastqc/*.
99. Wingett SW, and Andrews S. FastQ Screen: A tool for multi-genome mapping and quality control. *F1000Res*. 2018;7:1338.
100. Zerbino DR, Achuthan P, Akanni W, Amode MR, Barrell D, Bhai J, et al. Ensembl 2018. *Nucleic acids research*. 2018;46(D1):D754-d61.
101. Kim D, Langmead B, and Salzberg SL. HISAT: a fast spliced aligner with low memory requirements. *Nature methods*. 2015;12(4):357-60.
102. Pertea M, Kim D, Pertea GM, Leek JT, and Salzberg SL. Transcript-level expression analysis of RNA-seq experiments with HISAT, StringTie and Ballgown. *Nat Protoc*. 2016;11(9):1650-67.
103. Anders S, Pyl PT, and Huber W. HTSeq--a Python framework to work with high-throughput sequencing data. *Bioinformatics (Oxford, England)*. 2015;31(2):166-9.
104. Huber W, Carey VJ, Gentleman R, Anders S, Carlson M, Carvalho BS, et al. Orchestrating high-throughput genomic analysis with Bioconductor. *Nature methods*. 2015;12(2):115-21.
105. Love MI, Huber W, and Anders S. Moderated estimation of fold change and dispersion for RNA-seq data with DESeq2. *Genome Biol*. 2014;15(12):550.
106. Benjamini Y, and Hochberg Y. Controlling the False Discovery Rate: A Practical and Powerful Approach to Multiple Testing. *Journal of the Royal Statistical Society Series B (Methodological)*. 1995;57(1):289-300.
107. Gerdes J, Schwab U, Lemke H, and Stein H. Production of a mouse monoclonal antibody reactive with a human nuclear antigen associated with cell proliferation. *Int J Cancer*. 1983;31(1):13-20.

108. Sulkowski PL, Corso CD, Robinson ND, Scanlon SE, Purshouse KR, Bai H, et al. 2-Hydroxyglutarate produced by neomorphic IDH mutations suppresses homologous recombination and induces PARP inhibitor sensitivity. *Science translational medicine*. 2017;9(375).
109. Burma S, Chen BP, Murphy M, Kurimasa A, and Chen DJ. ATM phosphorylates histone H2AX in response to DNA double-strand breaks. *J Biol Chem*. 2001;276(45):42462-7.
110. Drusian L, Nigro EA, Mannella V, Pagliarini R, Pema M, Costa ASH, et al. mTORC1 Upregulation Leads to Accumulation of the Oncometabolite Fumarate in a Mouse Model of Renal Cell Carcinoma. *Cell Rep*. 2018;24(5):1093-104 e6.
111. Adam J, Hatipoglu E, O'Flaherty L, Ternette N, Sahgal N, Lockstone H, et al. Renal cyst formation in Fh1-deficient mice is independent of the Hif/Phd pathway: roles for fumarate in KEAP1 succination and Nrf2 signaling. *Cancer Cell*. 2011;20(4):524-37.
112. Harlander S, Schonenberger D, Toussaint NC, Prummer M, Catalano A, Brandt L, et al. Combined mutation in Vhl, Trp53 and Rb1 causes clear cell renal cell carcinoma in mice. *Nat Med*. 2017;23(7):869-77.
113. Tanner LB, Goglia AG, Wei MH, Sehgal T, Parsons LR, Park JO, et al. Four Key Steps Control Glycolytic Flux in Mammalian Cells. *Cell Syst*. 2018;7(1):49-62 e8.
114. Pylayeva-Gupta Y, Grabocka E, and Bar-Sagi D. RAS oncogenes: weaving a tumorigenic web. *Nature reviews Cancer*. 2011;11(11):761-74.
115. Lee DC, Sohn HA, Park ZY, Oh S, Kang YK, Lee KM, et al. A lactate-induced response to hypoxia. *Cell*. 2015;161(3):595-609.
116. van Rijswijk M, Beirnaert C, Caron C, Cascante M, Dominguez V, Dunn WB, et al. The future of metabolomics in ELIXIR. *F1000Res*. 2017;6.
117. Mei L, Smith SC, Faber AC, Trent J, Grossman SR, Stratakis CA, et al. Gastrointestinal Stromal Tumors: The GIST of Precision Medicine. *Trends Cancer*. 2018;4(1):74-91.